EES Solar

REVIEW

View Article Online
View Journal | View Issue

Cite this: *EES Sol.*, 2025, **1**, 441

Recent progress in Pb-, Sn-, and Pb–Sn-based inorganic perovskite solar cells: toward enhanced stability and efficiency

Seok Yeong Hong, [a] David Sunghwan Lee, [a] Hyong Joon Lee, [a] Ki-Ha Hong *[b] and Sang Hyuk Im *[ac]

All-inorganic metal halide perovskites have attracted increasing attention as promising materials for inorganic perovskite solar cells, owing to their superior thermal and chemical stability and wider bandgap tunability compared to organic–inorganic hybrid perovskites. However, inorganic perovskite has the problem of phase instability, as these materials are prone to undesirable phase transitions induced by both intrinsic and extrinsic factors. Such instability significantly degrades the long-term stability and efficiency of inorganic perovskite solar cells. In this review, we provide a comprehensive overview of Pb-, Sn-, and Pb–Sn-based inorganic perovskite solar cells. We systematically address various intrinsic and extrinsic factors that induce phase transitions and degrade the stability of inorganic perovskite. In particular, we focus on polymorphic transitions and examine how α/β/γ to δ transformations determine the optoelectronic properties in $CsPbX_3$, $CsSnX_3$ and their Pb–Sn alloys. In addition, we introduce recent strategies to suppress or mitigate these factors in order to develop long-term stable and highly efficient inorganic perovskite solar cells and inorganic perovskite-based tandem solar cells.

Received 26th April 2025
Accepted 1st July 2025

DOI: 10.1039/d5el00065c

rsc.li/EESSolar

Broader context

This review explores recent advances and key challenges related to inorganic perovskite materials. Inorganic perovskite materials, which eliminate volatile organic cations such as methylammonium (MA) and formamidinium (FA), have attracted considerable interest in the field of perovskite photovoltaics due to their superior thermal stability compared to hybrid perovskites. However, despite these advantages, issues such as phase transitions and poor phase stability continue to limit the long-term durability and power conversion efficiency of inorganic perovskite solar cells. In this review, we comprehensively analyze the intrinsic and extrinsic factors that trigger phase transitions and instability in Pb-, Sn-, and Pb–Sn-based inorganic perovskites-including lattice distortion, tolerance factor mismatch, ion migration, moisture exposure, and light-induced degradation. We further examine recent advances in mitigating these challenges through strategies such as compositional engineering, additive incorporation, surface and interface passivation, and heterostructure engineering. By categorizing and discussing these approaches in the context of both long-term stability and efficiency enhancement, this review aims to provide valuable insight for the development of robust inorganic perovskite solar cells and all-inorganic tandem solar cells with improved operational performance.

1. Introduction

Metal halide perovskites (MHPs) have garnered tremendous interest in the field of solar cells, light emitting diodes (LEDs), and various photo-electronic devices since Miyasaka first reported halide perovskite-based sensitized solar cells in 2009.[1–7] Certified power conversion efficiency (PCE) of perovskite solar cells has reached 27%, which almost paralleled the best PCE of silicon-based solar cells (27.6%), and the PCE of perovskite/Si tandem cells has exceeded 30% already.[8] However, the highest efficiencies reported to date have all come from solar cells made from organic cation-based perovskite materials such as methylammonium (MA) and formamidinium (FA). Organic components such as methylammonium MA and FA undergo chemical decomposition when exposed to extreme conditions including high temperature, moisture, oxygen, and illumination, due to their hygroscopic and volatile nature. As a result, hybrid perovskite solar cells (PSCs) suffer from poor long-term stability, significantly limiting their fabrication, storage, and commercial viability.[9–13]

Replacing organic components with the inorganic cesium (Cs) cation to create all-inorganic $CsPbX_3$ perovskites (where X = Cl, Br, I, or mixed halogens) represents a viable and effective strategy to overcome decomposition problems.[14] All-inorganic $CsPbX_3$ perovskites demonstrate significantly improved heat resistance, with thermal decomposition occurring only above 400 °C,[15,16] unlike their hybrid counterparts. Given its suitable bandgap (~1.7 eV, which is the closest among $CsPbX_3$

[a]*Department of Chemical and Biological Engineering, Korea University, Seoul, 02841, Republic of Korea. E-mail: imromy@korea.ac.kr*

[b]*Department of Materials Science and Engineering, Hanbat National University, Daejeon 34158, Republic of Korea. E-mail: kiha.hong@hanbat.ac.kr*

[c]*Perolight, New Engineering Hall, 45 Anam-ro, Seongbuk-gu, Seoul 02841, Republic of Korea*

compositions to the Shockley–Queisser limit for single-junction solar cells) and low-cost solution processability, $CsPbI_3$ has been recognized as one of the most promising candidates to overcome the instability of hybrid perovskites and drive perovskite photovoltaics toward industrial viability (Fig. 1).[16,17]

Despite its potential, $CsPbI_3$ faces a critical challenge in that its perovskite black phases are thermodynamically metastable at room temperature. $CsPbI_3$ crystallizes in a cubic (α) phase at high temperature (~320 °C) but under ambient conditions (especially in the presence of moisture), freshly formed black-phase $CsPbI_3$ readily undergoes a phase transition to the yellow δ-phase, which is a non-perovskite structure with a larger bandgap and inferior charge-transport properties.[17,18]

Parallel to $CsPbI_3$, significant attention has also been directed toward its lead-free analog, $CsSnI_3$. $CsSnI_3$ addresses environmental and toxicity concerns associated with lead-based materials and offers a narrower bandgap closer to the ideal Shockley–Queisser (SQ) limit (~1.3 eV).[19] While $CsSnI_3$ also experiences the undesirable δ-phase transformation, its stability issues are further exacerbated by the easy oxidation of Sn^{2+} to Sn^{4+}, causing deep trap formation and rapid performance degradation in practical environments.[20–22]

Using $Cs(Pb,Sn)I_3$ solid solutions has emerged as a strategy to overcome these limitations by combining the enhanced stability imparted by lead-based frameworks with the favorable bandgap tuning provided by Sn substitution in the range of 1.35–1.76 eV.[23] Recent studies, particularly using compositions such as $CsPb_{0.7}Sn_{0.3}I_3$, have demonstrated significant advancements, achieving a record efficiency of up to 17.55%, the highest reported to date for inorganic Pb–Sn alloyed perovskite solar cells with bandgaps below 1.35 eV. This notable efficiency underscores their potential for excellent spectral matching in tandem solar

Seok Yeong Hong

Seok Yeong Hong received his B.S. degree in Chemical Engineering from Dankook University and is currently continuing his academic career as a graduate student in the Department of Chemical and Biological Engineering at Korea University. His research interests focus on perovskite solar cells and tandem devices.

David Sunghwan Lee

David Sunghwan Lee received his M.S. degree in Chemical Engineering from Korea University in 2021 and his B.S. degree in Chemical Engineering from the University of California, Berkeley, in 2015. He is currently working towards his doctorate degree in the Department of Chemical and Biological Engineering at Korea University under the guidance of Prof. Sang Hyuk Im. His research interests are high efficiency perovskite solar cells.

Hyong Joon Lee

Hyong Joon Lee received his BS degree from the Department of Chemical and Biological Engineering at Korea University in 2020 and continued his academic career as a graduate student at Korea University. His research interests include perovskite optoelectronics and material designs.

Ki-Ha Hong

Ki-Ha Hong has been a Professor in the Department of Materials Science and Engineering at Hanbat National University since 2011. Previously, he was a principal research scientist at the Samsung Advanced Institute of Technology, Samsung Electronics. He received his B.S., M.S., and Ph.D. degrees in Materials Science and Engineering from Seoul National University. His research interests include computational materials science, focusing on density functional theory, computational nanoelectronics, halide perovskites, ferroelectric materials, thermodynamics of alloys, and AI-driven materials development.

Sang Hyuk Im

Sang Hyuk Im received his Ph.D. degree in Chemical & Biomolecular Engineering from the Korean Advanced Institute of Science and Technology (KAIST) in 2003. He has worked at the University of Washington (~2005), LG Chemicals Research Park (~2009) and the Korea Research Institute of Chemical Technology (KRICT) until 2013 as a senior research scientist. He was an associate professor in the Department of Chemical Engineering at Kyung Hee University. He is a professor in the Department of Chemical and Biological Engineering at Korea University. His research interests are material design and application of metal halide perovskites in fields such as solar cells, LEDs, detectors, photobatteries, photocapacitors, quantum sensing and carbon neutrality.

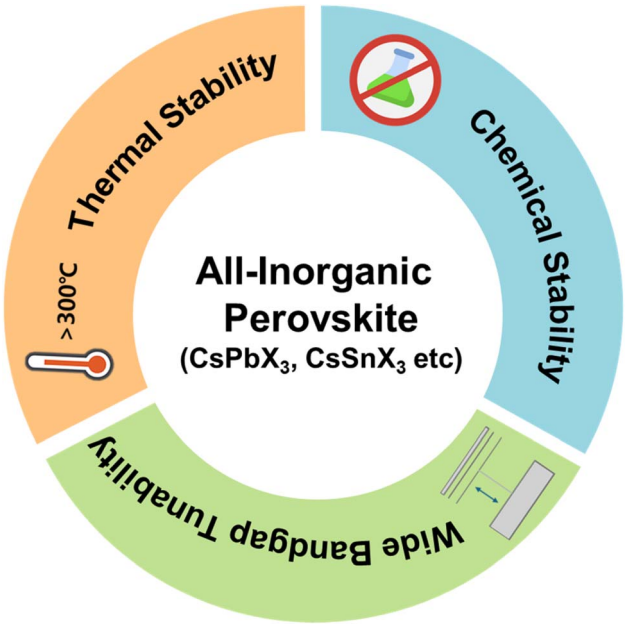

Fig. 1 Illustration of advantages of all-inorganic perovskites.

cell configurations, thus driving intense research interest.[24] Although Cs(Pb,Sn)I_3 demonstrates improved phase stability and oxidation resistance relative to pure $CsSnI_3$, significant challenges remain, particularly in managing Sn^{2+} oxidation and ensuring long-term operational stability.[25,26]

Most previous reviews have treated Pb-, Sn-, or Pb–Sn-based inorganic perovskite individually, with few providing a comprehensive discussion that encompasses all three compositions. In addition, the effects of various degradation factors on the performance of inorganic perovskite solar cells have generally been addressed briefly, with previous reviews primarily focusing on specific solution strategies.

In this review, we systematically discuss the issue of the phase transition, which is one of the primary causes of reduced stability and efficiency in inorganic perovskites, along with various intrinsic and extrinsic factors that affect stability. We provide the first cross-cutting roadmap that systematically maps the α/β/γ ↔ δ transformations of Pb-, Sn-, and Pb–Sn-alloys to strain, defect chemistry, and interface design. Furthermore, we classify and discuss recent strategic approaches for improving the performance of Pb-, Sn-, and Pb–Sn-based inorganic perovskite solar cells from the perspectives of long-term stability enhancement and efficiency enhancement. In addition, we summarize research on tandem solar cells employing inorganic perovskites to overcome the efficiency limit of single-junction solar cells. Finally, we present our outlook on the future development direction of inorganic perovskite solar cells.

2. Phase transition and stability

2.1 Overview of phase transitions in inorganic halide perovskites

Inorganic metal halide perovskites of compositions $CsPbI_3$, $CsSnI_3$, and their alloys Cs(Pb,Sn)I_3 exhibit multiple crystalline phases with distinct structures (cubic, tetragonal, and orthorhombic) that can interconvert depending on temperature and other conditions. At high temperatures, these materials adopt a cubic (α-phase) perovskite structure (space group $Pm\bar{3}m$), in which Cs^+ occupies the cuboctahedral A-site, Pb^{2+} or Sn^{2+} occupies the B-site center of corner-sharing $[BX_6]^{4-}$ octahedra, and I^- occupies the X-site connecting the octahedral corners. Upon cooling, the lattice undergoes symmetry-lowering distortions (octahedral tilting) to tetragonal (β-phase) or orthorhombic (γ-phase) perovskite structures as shown in Fig. 2a.[27,28] Under ambient conditions, the thermodynamically stable phase is the non-perovskite δ-phase (often yellow in color) in which the corner-sharing network of octahedra is broken. These structural phase transitions are driven by thermodynamics: the high-temperature cubic phase is stabilized primarily by entropy due to increased vibrational and configurational freedom at elevated temperatures, whereas lower temperature phases minimize enthalpy by adopting more stable and energetically favorable lattice configurations through lattice distortions.

In $CsPbI_3$, the cubic α-phase (black polymorph) is only stable above ~330 °C. As temperature decreases, $CsPbI_3$ transitions from α (cubic) to β (tetragonal) at ~281 °C and then to γ (orthorhombic perovskite) at ~184 °C. All three α, β, and γ phases are photoactive black phases with band gaps ~1.7–1.75 eV, suitable for optoelectronics.[32] However, at room temperature the perovskite γ-phase is metastable and will slowly convert to the δ-phase (yellow), which is a lower-symmetry non-perovskite structure with a larger band gap and poor electronic properties (Fig. 2b).[29,33]

Similarly, $CsSnI_3$ was experimentally reported to exhibit polymorphism with three distinct metastable black-phase structures. Specifically, $CsSnI_3$ undergoes two-step phase transitions during cooling: from cubic (α-$CsSnI_3$, space group $Fm\bar{3}m$, stable above 440 K) to tetragonal (β-$CsSnI_3$, space group $P4/mbm$, stable between 362 and 440 K) and then to orthorhombic (γ-$CsSnI_3$, space group $Pnma$, stable below 362 K).[34] Below room temperature, the material eventually transforms into a yellow non-perovskite δ-phase upon prolonged exposure to ambient conditions or moisture. In essence, both $CsPbI_3$ and $CsSnI_3$ share the trait that their perovskite-structured phases are metastable at room temperature, in contrast to analogous inorganic perovskites with smaller anions (*e.g.* $CsPbBr_3$ and $CsPbCl_3$) which remain perovskites under ambient conditions (albeit with distorted orthorhombic symmetry).[35–37]

From a thermodynamic perspective, phase stability is determined by the free energy $G(T,P)$ of each polymorph. The cubic α-phase, while entropically favored at high T, has a higher enthalpy at room temperature than the δ-phase, making α metastable (local minimum) and δ the global minimum under ambient conditions. Using RT solution calorimetry and differential scanning calorimetry, Wang *et al.* reported the formation enthalpies (ΔH) of the α and δ phases of $CsPbI_3$ ($\Delta H_\alpha = -2.83 \pm 0.90$ kJ mol^{-1}, $\Delta H_\delta = -16.93 \pm 0.87$ kJ mol^{-1}), as depicted in Fig. 2c.[30] The conversion of the δ phase to the α phase is associated with an enthalpy change of 14.10 ± 0.24 kJ mol^{-1} and an entropy change of 23.78 J (mol K)$^{-1}$. The phase transition from α (or β/γ) to δ is typically first-order, involving a discontinuous

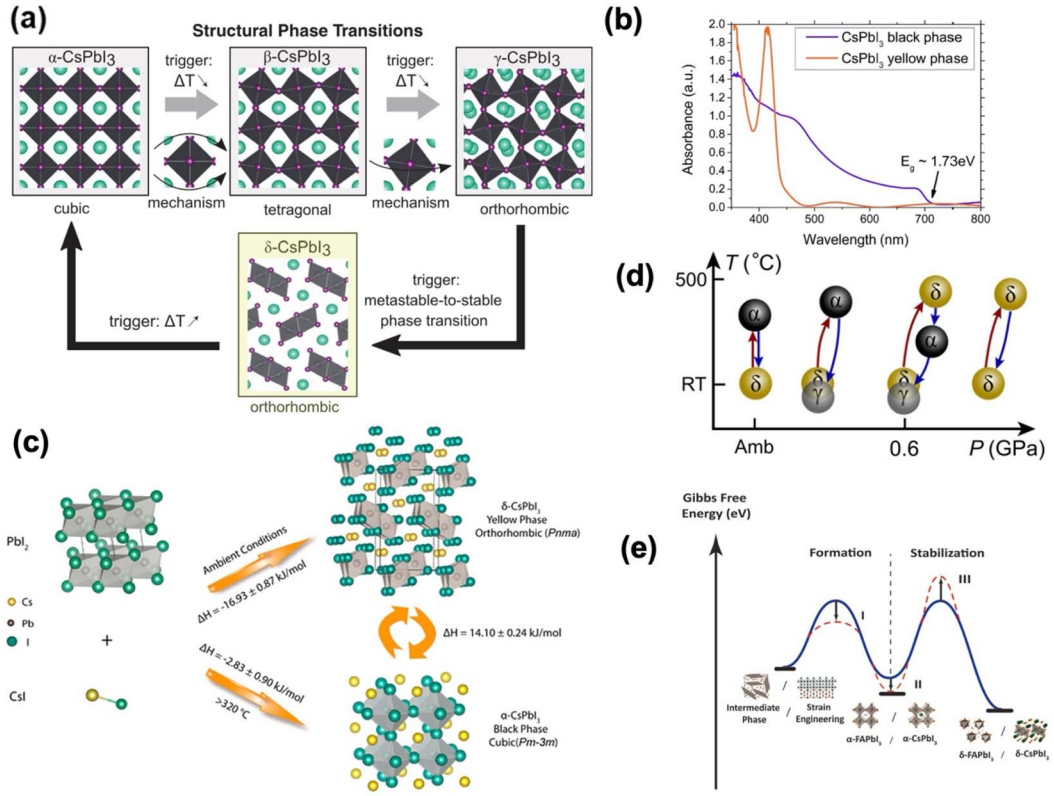

Fig. 2 Phase transitions in inorganic halide perovskites. (a) Structural phase transition of $CsPbI_3$ (ref. 27) (reproduced with permission from *Science*, 2019, **365**, 679–684. Copyright 2019 AAAS), (b) Absorbance spectra of black and yellow phases of $CsPbI_3$ thin films[29] (reproduced with permission from the *Journal of Materials Chemistry A*, 2015, **3**, 19688–19695. Copyright 2015 Royal Society of Chemistry), (c) diagram of the formation enthalpy of α- and δ-$CsPbI_3$ and the enthalpy change of the δ to α phase transition (reproduced with permission from the *Journal of the American Chemical Society*, 2019, **37**, 14501–14504. Copyright 2019 American Chemical Society), and (d) phase transition of $CsPbI_3$ at varying *P*–*T*[28] (reproduced with permission from *Nature Communications*, 2021, **12**, 461. Copyright 2021 Springer Nature).[30] (e) Thermodynamic changes of phase transitions for the formation and stabilization processes of $FAPbI_3$ and $CsPbI_3$ metastable perovskite phases[31] (reproduced with permission from *Cell Reports Physical Science*, 2024, **5**, 101825. Copyright 2024 Cell Press).

change in the structure and volume and often a latent heat. Kinetics play a key role: fast cooling (thermal quenching) can kinetically trap the material in a metastable black phase at room temperature by preventing the rearrangement required for the δ-phase.[17,32] Indeed, quenching $CsPbI_3$ from high temperature can retain β/γ-$CsPbI_3$ at room temperature, as the rapid change induces internal strain that raises the energy barrier for the transition.[27] However, given sufficient time or slight stimuli, the trapped β/γ phase will still relax to δ-$CsPbI_3$ as this allows strain release. Pressure can also influence these thermodynamics: applying external pressure generally favors denser phases and can alter the transition temperature. Orthorhombic γ-$CsPbI_3$ has been successfully stabilized through the combined application of moderate pressure (0.1–0.6 GPa) and heat treatment, with the phase remaining intact upon decompression under ambient conditions. The interrelation of phase transitions as a function of pressure and temperature parameters is illustrated in Fig. 2d.[28] Thus, by controlling temperature, pressure, and composition, researchers can tune both the energy barriers and relative phase energies, enabling access to different phases and stabilizing high-temperature phases that are metastable under room conditions. Composition (such as mixing Pb/Sn or halide content) similarly shifts phase stabilities, as discussed next, by altering the lattice dimensions and energetics (Fig. 2e).[31,38,39]

2.2 Intrinsic factors influencing stability

2.2.1 Goldschmidt's tolerance factor and geometrical effects. The Goldschmidt tolerance factor (TF, *t*) and octahedral factor (OF, *m*) are common indicators for stable three-dimensional perovskites. The *t* and *m* are defined as $(r_A + r_X)/(\sqrt{2}(r_B + r_X))$ and r_B/r_X, respectively, where $r_{A/B/X}$ means the ionic radius of A (Cs^+), B (Pb^{2+} or Sn^{2+}) and X (I^-), schematics of which can be found in Fig. 3a.[40] For ideal perovskites a tolerance factor in the range 0.9–1.0 yields a stable cubic structure, whereas significantly lower or higher values favor distorted or non-perovskite structures. There have been various efforts to use *t* to predict the stability of 3-dimensionally (3-D) connected perovskite structures such as α, β, and γ phases.[41–44] Travis *et al.*[44] suggested revised stable regimes of the tolerance factor ($0.875 < t < 1.06$) and octahedral factor ($0.41 < m$) with a revised ionic radius ($r_{Sn} = 0.97$ Å and $r_{Pb} = 1.03$ Å) for iodide compounds. The predicted stable area for Sn-based

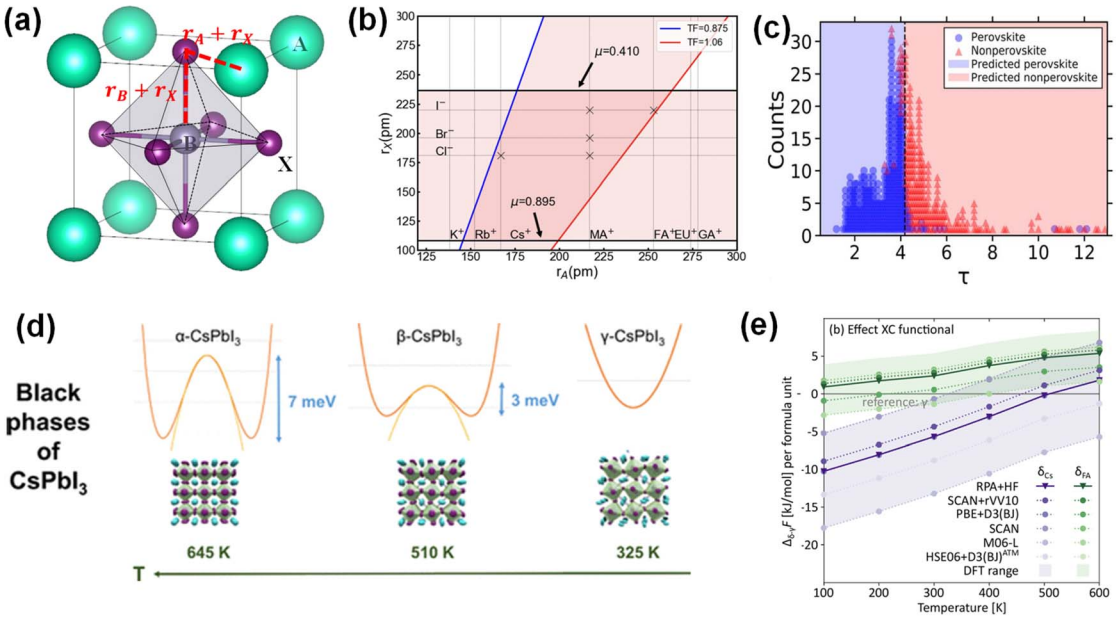

Fig. 3 Goldschmidt's tolerance factor, geometrical effects and phonon effects on stability. (a) The structural description of an ideal ABX_3-type perovskite structure[40] (reproduced with permission from *Solar RRL*, 2020, **4**, 2000513. Copyright 2020 Wiley-VCH GmbH). (b) The stable area prediction for Sn-based halide perovskites with regard to the tolerance factor (TF, $0.875 \leq TF \leq 1.06$) and octahedral factor (m, $0.41 \leq \mu \leq 0.895$)[40] (reproduced with permission from *Solar RRL*, 2020, **4**, 2000513. Copyright 2020 Wiley-VCH GmbH). (c) Classification using the machine learned new tolerance factor[43] (reproduced with permission from *Science Advances*, 2019, **5**, eaav0693. Copyright 2019 AAAS). (d) Phonon-driven polymorphic phase transitions among black phases (α, β, and γ) of $CsPbI_3$, highlighting small energy differences that govern structural stability[45] (reproduced with permission from *ACS nano*, 2018, **12**, 3477–3486. Copyright 2018 American Chemical Society). (e) Comparison of the impact of different exchange correlations to calculate phase transition temperatures[46] (reproduced with permission from *Chemistry of Materials*, 2022, **34**, 8561–8576. Copyright 2022 American Chemical Society).

halide perovskites is presented in Fig. 3b.[40] The tolerance factor of $CsPbI_3$ is lower than that of $CsSnI_3$ due to the larger Pb^{2+} ionic radius. This low tolerance factor is a primary intrinsic reason that the corner-sharing $(Pb/Sn)I_6$ network cannot be maintained without distortion – the Cs^+ cation is simply too small relative to the $(Pb/Sn)I_3$ framework, so the structure collapses to the δ-phase (with isolated $(Pb/Sn)I_6$ octahedra) at room temperature. Recent research by Bartel *et al.* introduced a significantly improved tolerance factor, achieving about 92% accuracy in predicting perovskite stability across diverse oxide and halide compositions. This revised factor incorporates ionic radii, oxidation states (n_A), and their ratios, enabling a more accurate and generalized stability prediction. Their work utilized a data-driven SISSO method to develop an improved tolerance factor defined using:

$$\tau = \frac{r_B}{r_X} - n_A\left(n_A - \frac{r_A/r_B}{\ln(r_A/r_B)}\right)$$

with a threshold value ($\tau < 4.18$) for stable perovskites (Fig. 3c).[43]

Despite these advancements, approaches based on tolerance factors continue to demonstrate fundamental limitations. Inconsistencies arise from different research groups employing varied ionic radius values and stability criteria, creating confusion in predicting perovskite structural stability. Indeed, several studies have erroneously predicted $CsPbI_3$ stability based on tolerance factor calculations alone.[47] Most notably, the approach relies purely on geometric and ionic considerations, disregarding important electronic and chemical effects such as orbital hybridization, covalency, defect chemistry, and anharmonic lattice dynamics. These chemical and electronic factors critically influence stability in real systems, especially for compounds with significant covalent bonding character or polarizable ions, thus limiting the universal applicability of tolerance factors alone.

2.2.2 Phonon effects on stability of inorganic perovskites. The stability of inorganic metal halide perovskites, particularly $CsPbI_3$ and $CsSnI_3$, is profoundly influenced by phonon effects, including harmonic and anharmonic lattice vibrations. These phonon dynamics fundamentally govern structural stability and phase transitions, key factors in determining their applicability in optoelectronic devices.

Within the harmonic approximation, lattice vibrations are assumed to be small oscillations around equilibrium positions with linear restoring forces. In this idealized scenario, phonon dispersion calculations using density functional theory (DFT) reveal soft-mode instabilities characterized by imaginary frequencies, especially prominent at the Brillouin zone boundaries.[45,48] Such instabilities indicate that the cubic high-symmetry phases (α-phase for $CsPbI_3$ and $CsSnI_3$) are inherently unstable at low temperatures, predicting spontaneous distortions to lower-symmetry orthorhombic or tetragonal structures.

However, the purely harmonic description does not fully capture temperature-dependent stability. This discrepancy is resolved by considering anharmonic phonon effects—nonlinearities in lattice vibrations arising from significant atomic displacements at finite temperatures. Anharmonicity manifests notably in phonon–phonon interactions, double-well potentials, and temperature-dependent frequency shifts, critically influencing the thermodynamic stability of phases as shown in Fig. 3d.[45,49,50] This dynamic stabilization explains the persistence of metastable black phases under conditions far from equilibrium, such as rapid quenching or lattice strain. Understanding phonon-driven stability mechanisms offers practical strategies for enhancing phase stability. For instance, compositional tuning through doping or alloying can modify phonon spectra, reducing anharmonic instabilities and suppressing undesirable phase transitions. Additionally, controlled lattice strain and microstructural engineering can selectively stabilize desired perovskite phases by altering vibrational modes and entropy contributions.[51] Accurate modeling of phonon properties is essential; recent research combining random-phase approximation (RPA) calculations with machine learning potentials (MLPs) has demonstrated significant sensitivity in predicted phase transition temperatures. For example, employing different exchange–correlation (XC) functionals or inadequate structural optimizations can cause deviations in predicted transition temperatures exceeding 100 K. Specifically, precise calculations using RPA combined with MLP corrections yielded transition temperatures within 50 to 100 K of experimental values, highlighting the necessity of carefully chosen computational methods for accurate stability predictions (Fig. 3e).[46]

2.2.3 Role of point defects. Intrinsic point defects (such as halide vacancies, interstitials, or cation antisites) can also influence phase stability. In particular, iodine vacancies (V_I)

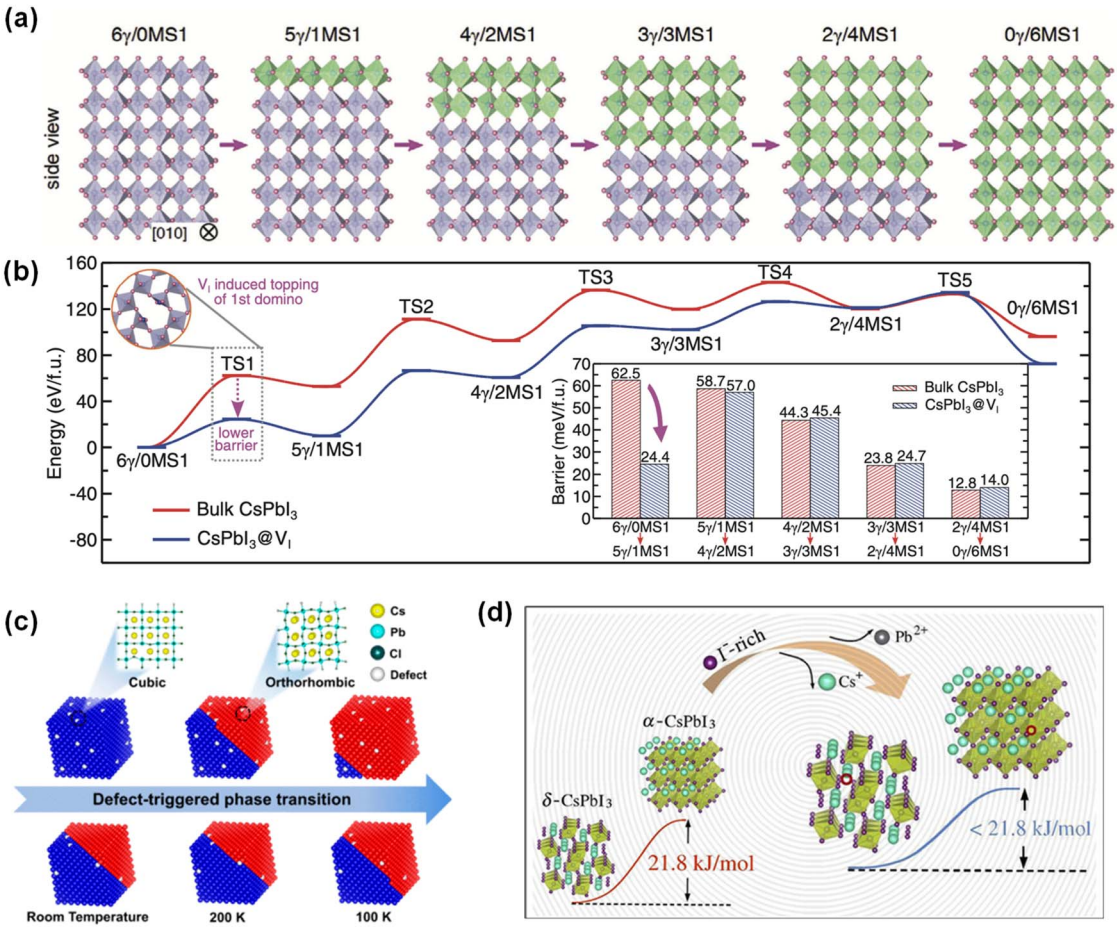

Fig. 4 Role of point defects. (a) Layer by layer phase transition processes between the γ-phase and MS1-phase (intermediate states having higher energy barriers)[52] (reproduced with permission from *Advanced Functional Materials*, 2024, **34**, 2308246. Copyright 2024 Wiley-VCH GmbH). (b) Transition barrier lowering by the formation of an iodine vacancy[52] (reproduced with permission from *Advanced Functional Materials*, 2024, **34**, 2308246. Copyright 2024 Wiley-VCH GmbH). (c) The conversion of subdomains from cubic to orthorhombic phases in defect-rich or fewer NCs when cooling down[54] (reproduced with permission from *Chemistry of Materials*, *ACS Materials Letters*, 2019, **1**, 185–191. Copyright 2019 American Chemical Society). (d) Schematic illustration of reducing the energy change from the d to the a phase by controlling Cs^+ and Pb^{2+} vacancies[55] (reproduced with permission from *Chemistry of Materials*, *The Journal of Physical Chemistry C*, 2019, **123**, 9735–9744. Copyright 2019 American Chemical Society).

have emerged as critical intrinsic defects that can tip the balance toward structural collapse of the perovskite framework. Theoretically, Guo *et al.* demonstrated that an iodine vacancy significantly lowers the kinetic barrier for the γ → δ transition and essentially acts as "the seed of the whole phase transition process," initiating the collapse of the corner-sharing Pb–I network.[52] Wylie *et al.* further revealed a multi-step transition pathway in which surface V_I defects create alternative short-lived intermediate states and reduce the activation energy for the first step of the γ → δ transformation.[53] In essence, an iodine vacancy breaks the bridging linkage between neighboring PbI_6 octahedra, which induces local tilting and a change from corner-to edge-sharing connectivity – the structural hallmark of the δ-phase. Once a critical nucleus of δ-$CsPbI_3$ forms at a defect site, the remaining phase transformation can propagate rapidly as a "domino effect," given that only small re-coordination and ion diffusion are needed to convert surrounding regions as shown in Fig. 4a and b.[52] This means that controlling the initial defect-mediated nucleation is key to stabilizing the desired phase. Ma *et al.* also demonstrated that structural defects, particularly halide vacancies, trigger stepwise and reversible phase transitions in cesium lead halide perovskite nanocrystals (NCs).[54] Upon cooling, the cubic subdomains in highly defective NCs gradually transform into orthorhombic phases from the quasi-cubic state at room temperature, whereas high-quality NCs, characterized by coexisting cubic and orthorhombic subdomains at room temperature, exhibit substantial resistance to this transition (Fig. 4c).

Experimental observations strongly support the above picture. Iodine vacancies tend to form readily under iodine-poor or destabilizing conditions (owing to their relatively low formation energy), and their presence correlates with accelerated phase degradation. For example, moisture is known to catalyze the black-to-yellow transition in $CsPbI_3$ by leaching iodide from the surface (*via* HI or I_2 formation), thereby amplifying the surface V_I concentration.[53] In contrast, vacancies on the cation sublattices (A-site Cs or B-site Pb vacancies) may have quite different effects. Cs vacancies, in particular, tend to stabilize the perovskite framework rather than destabilize it (Fig. 4d). Thermodynamic calculations by Kye *et al.* showed that the introduction of cation vacancies weakens the coupling between Cs^+ ions and the PbI_6 octahedral network, thereby lowering the energy difference between the cubic/orthorhombic perovskite phase and the δ-phase.[55] However, Kye's theoretical study extrapolates macroscopic phase stability from single-defect formation energies, neglecting defect–defect interactions; moreover, the very high vacancy concentrations required for full stabilization have yet to be experimentally verified.

2.3 Extrinsic factors and environmental effects

2.3.1 Moisture. Ambient humidity is a well-known trigger for black-to-yellow phase transitions in $CsPbI_3$. Thin films of cubic or orthorhombic black-phase $CsPbI_3$ rapidly convert to the non-perovskite yellow δ-phase upon exposure to moisture. For example, *in situ* tests showed that α-$CsPbI_3$ completely transitions to δ-$CsPbI_3$ in under 75 minutes at 33% relative humidity and room temperature.[56] Similarly, the β/γ $CsPbI_3$ phases are highly vulnerable to moisture attack and they quickly destabilize and turn yellow when exposed.[57]

Lin *et al.* quantified the kinetics of this moisture-induced phase change: higher relative humidity dramatically increases the nucleation rate of the yellow phase, accelerating the black → yellow conversion (Fig. 5a and b).[58] Crucially, water itself is not consumed into new compounds (no permanent hydrates are formed); instead, it acts as a catalyst. Dastidar *et al.* measured a black → yellow phase-change enthalpy of ∼14.2 kJ mol^{-1} and found that under dry inert conditions the trapped black phase remains stable up to ∼100 °C.[56] The presence of water vapor did not alter the phase equilibrium enthalpy, but sped up the transformation, confirming that moisture primarily catalyzes the phase transition rather than shifting the thermodynamics.[56] Interestingly, δ-$CsPbI_3$ can be easily converted into a perovskite phase by annealing, which is the distinguished feature of inorganic perovskites with hybrid perovskites. This reversible characteristic of $CsPbI_3$ enables its application in thermochromic solar cells (Fig. 5c and d).[59]

Surface iodide vacancies serve as nucleation sites for δ-$CsPbI_3$ growth, with moisture amplifying these vacancies by strongly solvating halide ions at the interface (Fig. 5e).[53] Wylie *et al.* showed that surface treatment strategies are effective in improving moisture resistance, with CsI and CdI_2 treatments reducing the phase transition rate by approximately 5-fold by filling surface iodide vacancies.[53]

Theoretical investigation revealed that H_2O and OH^- largely affect the kinetics by lowering the activation energy, whereas H^+ has a negligible effect on the kinetics by calculating the phase transition barrier with DFT (Fig. 5f).[60] For $CsSnI_3$, moisture effects have not been thoroughly investigated as much as in the case of $CsPbI_3$, yet. Yang *et al.*'s DFT calculations presented that water adsorbed on the surface of γ-phase $CsSnI_3$ could induce charge transfers between the H atom in the water and adjacent I atoms and between the O atom and Cs^+, leading to distortion of SnI_6 octahedra and structural deformation, which can be the plausible origin of phase instability.[61]

The recognition of water as a catalyst (rather than a reactant) was key to devising mitigation strategies: theory indicated that simply keeping films dry or introducing water-resistant interfaces could preserve the metastable black phase. Indeed, encapsulation and surface passivation (to prevent H_2O adsorption) emerged as effective measures to maintain black-phase stability in humid environments, aligning with the computational predictions.

2.3.2 Oxygen. In contrast to moisture, molecular oxygen affects $CsPbI_3$ and $CsSnI_3$ differently due to their chemistry. All-inorganic $CsPbI_3$ is comparatively robust against oxygen alone, which is a distinguished feature of the hybrid perovskite undergoing superoxide-driven auto-decomposition.[61] Because superoxide is experimentally shown to deprotonate the organic A-site cations in $MAPbI_3$ and $FAPbI_3$—triggering their conversion to PbI_2, I_2, water and volatile amines—whereas Cs^+ offers no such labile proton, this oxygen-induced degradation route is effectively absent in all-inorganic $CsPbI_3$.[16,62]

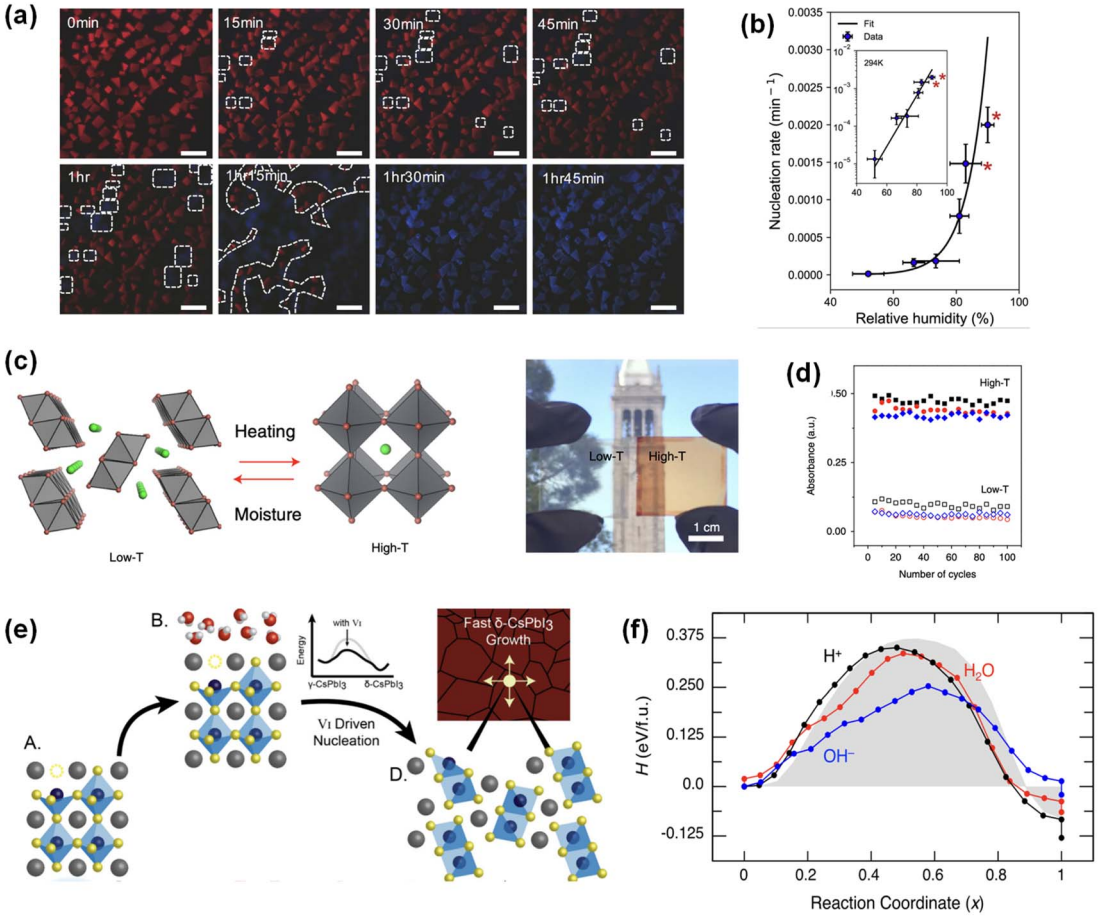

Fig. 5 Effect of moisture on inorganic perovskites. (a) PL micrographs of $CsPbI_3$ at 90% RH over time under 375 nm laser excitation. Dotted lines: a guide to the eye highlighting the emergence of low-*T* phase crystals. Scale bars, 20 μm (ref. 58) (reproduced with permission from *Matter*, 2021, **4**, 2392–2402. Copyright 2021 Cell Press). (b) Dependence of the nucleation rate (J_N) on RH. Inset: the nucleation rate shown in the log plot[58] (reproduced with permission from *Matter*, 2021, **4**, 2392–2402. Copyright 2021 Cell Press). (c) Photograph of the low-*T* phase and high-*T* phase (orange-red-colored) thin films[59] (reproduced with permission from *Nature Materials*, 2018, **17**, 261–267. Copyright 2018 Springer Nature). (d) The stable and reversible switching of the absorption (550 nm) of the three $CsPbIBr_2$ thin films over 100 phase transition cycles. (e) Schematic of V_I and H_2O driven fast δ-$CsPbI_3$ growth[59] (reproduced with permission from *Nature Materials*, 2018, **17**, 261–267. Copyright 2018 Springer Nature). (f) Variation of *H* (enthalpy) during the γ-to-δ phase transition in the presence of H_2O, H^+, and OH^- within $CsPbI_3$. The shaded curve represents the pristine case[60] (reproduced with permission from *Chemistry of Materials*, 2023, **35**, 2321–2329. Copyright 2023 American Chemical Society).

By comparison, tin-based perovskites are extremely oxygen-sensitive. Oxygen exposure induces a chemical oxidation: Sn^{2+} (in the black perovskite) oxidizes to Sn^{4+}, which destabilizes the perovskite lattice and generates a yellow or amorphous phase. This manifests as rapid degradation of the optoelectronic properties of $CsSnI_3$ in air. The pronounced oxygen sensitivity of $CsSnI_3$ stems from the synergy between redox chemistry and defect formation in its Sn-based lattice. Frost diagrams indicates that Pb^{2+} is in a deep asymmetric thermodynamic sink while Sn^{2+} is in a shallow sink (Fig. 6a), which can lead to oxidation pathways for Sn^{2+}.[63] Therefore, adsorbed O_2 or O_2/H_2O rapidly extracts electrons and converts Sn^{2+} to Sn^{4+}, which can result in V_{Sn} and lower the defect formation energy barrier. Tin vacancies raise the native p-doping level and accommodate the oxidized Sn^{4+} ions.

Oxygen can trigger cyclic degradation of tin-based perovskites. Haque *et al.* revealed that oxidized Sn^{4+} complexes with I^-, releasing SnI_4; SnI_4 hydrolyses to HI + SnO_2, and HI + O_2 ⇒ I_2 + H_2O. I_2 is itself a strong oxidant toward remaining Sn^{2+}, creating a cyclic degradation loop (Fig. 6b).[64] Depletion of Sn destabilizes the already metastable black perovskite and drives it toward yellow δ-$CsSnI_3$ and then vacancy-ordered Cs_2SnI_6 or direct conversion into yellow Cs_2SnI_6 (Fig. 6c).[65] The high-lying Sn 5s and I 5p valence bands also facilitate hole transfer to O_2, so easy Sn oxidation, self p-doping, iodine autocatalysis, lattice metastability and favorable band energetics together make $CsSnI_3$ far more air-labile than its Pb counterpart (energy levels can be found in Fig. 6d).[66]

2.3.3 Light irradiation. $CsPbI_3$ is generally more photostable than hybrid perovskites, but intense illumination can still induce structural changes under certain conditions.[17]

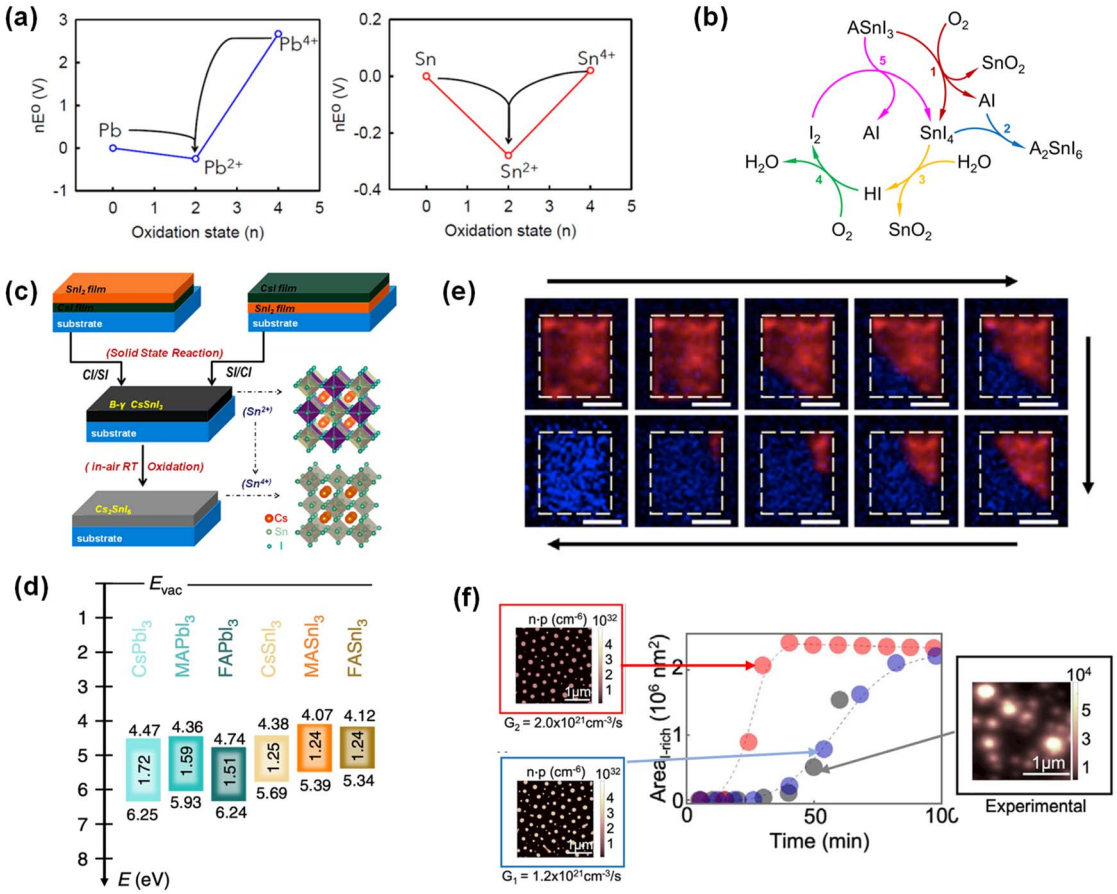

Fig. 6 Effect of oxygen and light irradiation on inorganic perovskites. (a) Frost diagrams for Pb and Sn under standard conditions[63] (reproduced with permission from *ACS Materials Letters*, 2021, **3**, 299–307. Copyright 2021 American Chemical Society). (b) Cyclic degradation mechanism of a tin iodide perovskite under ambient air exposure[64] (reproduced with permission from *Nature Communications*, 2021, **12**, 2853. Copyright 2021 Springer Nature). (c) Growth of Cs_2SnI_6 from $CsSnI_3$ (ref. 65) (reproduced with permission from *Energy & Environmental Science*, 2019, **12**, 1495–1511. Copyright 2019 Royal Society of Chemistry). (d) Energy levels of Pb- and Sn–iodide perovskites. Adapted with minor modifications[66] (reproduced with permission from *Nature Communications*, 2019, **10**, 2560. Copyright 2019 Springer Nature). (e) Confocal false-color images with the red and blue colors corresponding to emission channels >600 and <600 nm (ref. 67) (reproduced with permission from *Matter*, *Matter*, 2022, **5**, 1455–1465. Copyright 2022 Cell Press). (f) The total area of the I-rich regions plotted as a function of time at carrier generate rates of G_1 (blue line) and G_2 (red line), respectively, in comparison with the experimental data (black dots)[68] (reproduced with permission from *Matter*, *Matter*, 2023, **6**, 2052–2065. Copyright 2023 Cell Press).

Notably, light often acts in synergy with other factors. Lin *et al.* discovered that at ambient humidity, illuminating $CsPbI_3$ with above-bandgap laser light accelerates the black → yellow transition dramatically.[67] Fig. 6e shows the time evolution of the laser-accelerated high-T to low-T phase transformation on a single $CsPbI_3$ micro-plate. However, under completely dry conditions, the same above-bandgap illumination did not trigger any phase change. This implies that light by itself does not destabilize the $CsPbI_3$ structure, but photogenerated carriers can amplify other degradation pathways (such as water-induced vacancy formation).

Another phenomenon observed under continuous illumination is halide redistribution in mixed-halide perovskites. In $CsPb(I_{1-x}Br_x)_3$, strong light causes iodine-rich and bromine-rich regions to segregate, leading to local bandgap changes.[69,70] Peng *et al.* conclusively showed that light-induced Br/I segregation in single-crystalline $CsPbBr_{2.1}I_{0.9}$ proceeds by spinodal decomposition, quantifying both the carrier-dependent kinetics and the nanometre-scale coarsening length using *in situ* cryo-STEM cathodoluminescence and phase-field modelling (Fig. 6f).[68]

Although this halide segregation is not directly connected with phase transformation, the ensuing I-rich micro-domains promote iodide-vacancy accumulation and local strain, which under severe operating conditions can nucleate the yellow δ-phase, so halide segregation—though structurally discrete—may indirectly accelerate phase degradation.

As mentioned above, phase transitions and instability in inorganic perovskites are induced by a variety of intrinsic and extrinsic factors, which in turn contribute to the degradation of both long-term operational stability and device efficiency. Accordingly, mitigating these instability-inducing factors, such as lattice distortions, defect formation, and environmental

stressors, is essential for enhancing the long-term stability and photovoltaic performance of inorganic perovskite solar cells.

3. Strategy for long-term stability

3.1 Compositional engineering

Compositional engineering has been widely adopted to promote stability of inorganic perovskite solar cells by incorporating foreign A site, B site, and X site ions. Various compositional engineering strategies have been reported that partially substitute constituent ions to alleviate lattice strains or to enhance inherent thermodynamic stability or construct low-dimensional phases to protect them from the external environment and to prevent interface-derived degradation processes (Table 1).[71–79]

3.1.1 A-site engineering. Li *et al.* introduced trimethylammonium lead tribromide ($TrMAPbBr_3$) within the precursor solution to formulate composites of inorganic $CsPbI_{3-x}Br_x$ and linearly rotatable $TrMAPbBr_3$.[71] The incorporated bulky TrMA cation forms a hexagonal low-dimensional perovskite phase with high lattice tolerance at the grain boundaries of the inorganic 3D perovskite moieties. $TrMAPbBr_3$ exhibits a flexible inorganic framework at high temperatures, damping the risk of Cs^+ ion migration from strong vibration at the atomic scale. The activation energy for the ion migration pathway is significantly hurdled as shown in Fig. 7a, stabilizing the $CsPbI_{3-x}Br_x$ composite. The resulting inorganic perovskite solar cell demonstrates 20.59% PCE with exceptional stability, with the unencapsulated device maintaining 91% of its original performance in an ambient environment after 3000 hours of storage.

3.1.2 B-site engineering. Nan *et al.* incorporated a small portion of Ge^{2+} in $CsPbI_3$ perovskite to afford improved inherent stability through B site composition engineering.[72] The smaller sized Ge^{2+} cation readily incorporates into the perovskite $CsPbI_3$ perovskite lattice, which was confirmed by a slight shift in bandgaps to 1.679 eV with 5% Ge^{2+} incorporation from 1.665 eV with pure $CsPbI_3$. The Ge^{2+} incorporated perovskite stabilizes the desired perovskite structure owing to the favorable Goldschmidt tolerance factor and octahedral factor and therefore exhibits lower formation energy, as shown in Fig. 8a. Moreover, the partial amount of Ge^{2+} forms GeO_2 native oxide at the perovskite surface, further strengthening the film stability.

Table 1 Stability enhancement *via* compositional engineering

No.	Strategy	Structure	Type	PCE	Stability	Ref.
1	A-site engineering	FTO/TiO_2/$CsPbI_{3-x}Br_x$:TrMA/P3HT/Ag	NIP	20.59	84% for 192 h@*T*: 85 °C/ambient air/ non-encapsulated 91% for 3055 h@ambient air/ non-encapsulated 97% for 2071 h@N_2	71
2	B-site engineering	FTO/TiO_2/PCBA/$CsPb_{0.95}Ge_{0.05}I_3$/ spiro-OMeTAD/Au	NIP	19.52	85.5% for 3000 h@MPP/ 1 sun illumination/N_2 92% for 1400 h@ambient air/ non-encapsulated	72
3		FTO/PCBM/$CsSn_{0.5}Ge_{0.5}I_3$/ spiro-OMeTAD/Au	NIP	7.11	90% for 500 h@MPP/ 1 sun light illumination/N_2	73
4		FTO/c-TiO_2/mp-TiO_2/ $CsSn_{1-x}Zn_xI_3$/Al_2O_3/NiO_x/carbon	PIN	8.27	86% for 216 h@ambient air/ non-encapsulated 90% for 30 d@N_2	74
5		ITO/SnO_2/$CsPb_{0.7}Sn_{0.3}IBr_2$:ZnC_2O_4/ spiro-OMeTAD/Au	PIN	14.1	450 h@*T*: 80 °C/N_2 75% for 240 h@ambient air/ non-encapsulated 1350 h@N_2	75
6	X-site engineering	FTO/TiO_2/$Cs_2PbI_2Cl_2$/$CsPbI_3$/ spiro-OMeTAD/Au	NIP	20.6	80% for 1000 h@MPP/ 1 sun illumination/N_2	76
7		ITO/SnO_2/$CsPbI_3$:$NH_4PbCl_{2.8}Br_{0.2}$/ spiro-OMeTAD/MoO_3/Ag	NIP	20.2	95% for 1000 h@MPP/ 1 sun illumination/ 80% for 250 h@*T*: 85 °C RH: 85%	77
8		FTO/NiO_x/$CsPb_{0.6}Sn_{0.4}I_3$:SnF_2*3FACl/ 4AMPI$_2$/PCBM/BCP/Ag	PIN	13.37	70% for 1045 h@MPP/ 1 sun illumination/*T*: 45 °C/N_2 77% for 100 h@*T*: 85 °C/N_2 100% for 2800 h@N_2	78
9		ITO/PEDOT:PSS/ $CsPb_{0.55}Sn_{0.45}I_2Br$:CsCl/$PbSO_4$/ PCBM/BCP/Ag	PIN	10.39	93% for 300 h@MPP/ 1 sun illumination/N_2 80% for 300 h@MPP/1 sun illumination/ *T*: 25 °C RH: 40–50%/ non-encapsulated 95% for 300 h@*T*: 85 °C/N_2 92.5% for 2000 h@N_2	79

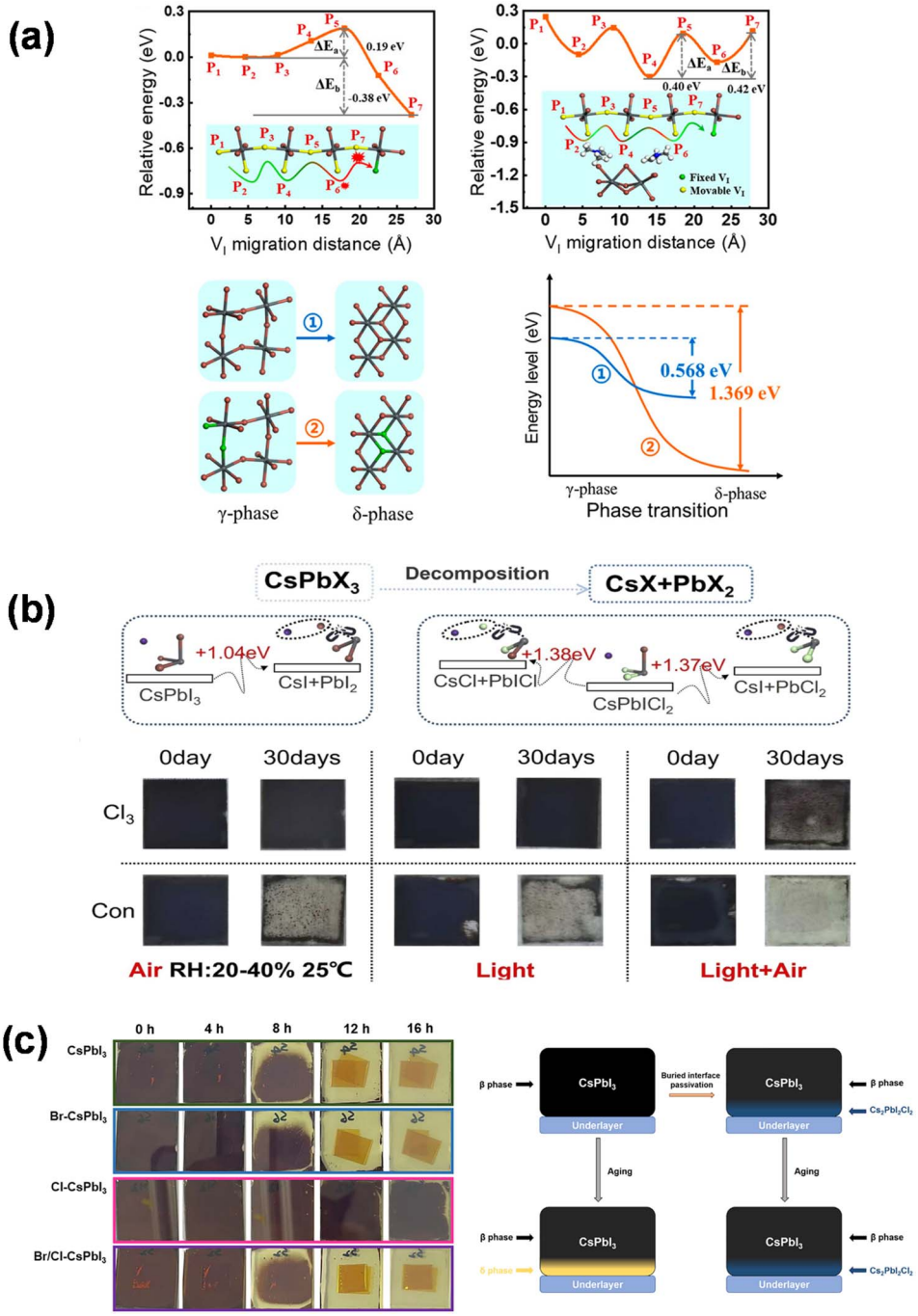

Fig. 7 The review of stability enhancement *via* composition engineering with (a) trimethylammonium in $CsPbI_{3-x}Br_x$ (reproduced with permission from *ACS Energy Lett.*, **8**(5), 2284–2291. Copyright 2023 American Chemical Society),[71] (b) NH_4PbX_3 in $CsPbI_3$ perovskite (reproduced with permission from *Nano Energy*, **132**, 110396. Copyright 2024 Elsevier)[77] and (c) CsCl in $CsPbI_3$ perovskite (reproduced with permission from *Cell Rep. Phys. Sci.*, **5**(5), 101935. Copyright 2024 Elsevier).[76]

As a result, the $CsPbI_3$ perovskite solar cell with a 5% GeI_2 additive demonstrated 19.52% PCE, along with substantial operational stability exceeding 3000 hours under 100 mW cm^{-2} light illumination and at 0.85 V applied bias voltage in a N_2 environment.

Wang *et al.* proposed a facile and effective galvanic displacement reaction approach for stable $CsSnI_3$ perovskite solar cells.[74] Metallic Zn powder was introduced into the perovskite precursor film, which behaves as a favorable redox couple with Zn/Zn^{2+} and Sn^{2+}/Sn^{4+} ions. The introduction of zinc powder thus successfully reduces the undesired Sn^{4+} species within the precursor solution and in turn results in reduced trap states in the final perovskite film. Moreover, the galvanic displacement reaction simultaneously incorporates

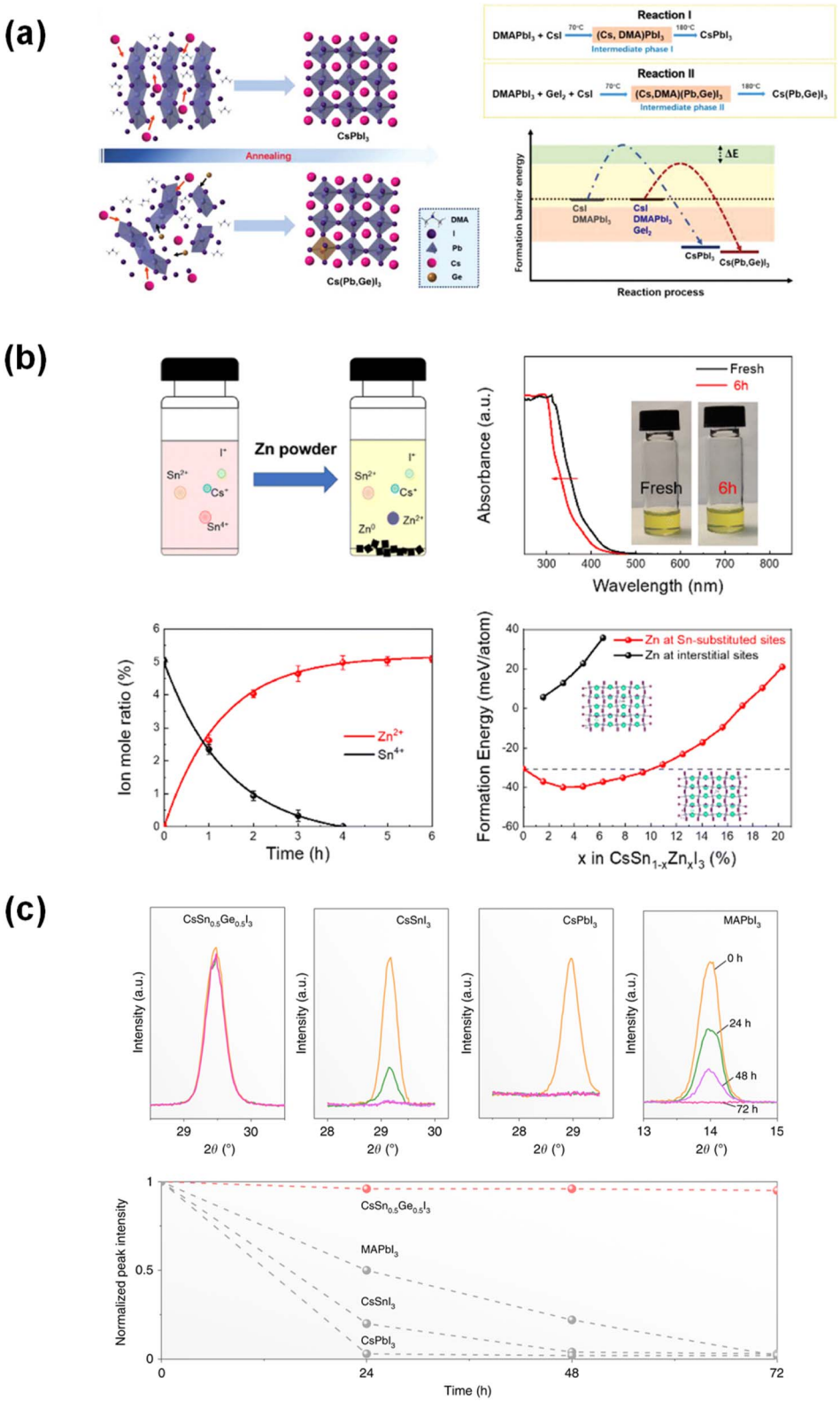

Fig. 8 The review of stability enhancement *via* composition engineering with (a) GeI_2 in $CsPbI_3$ (reproduced with permission from *Adv. Energy Mater.*, **12**(10), 2103690),[72] (b) Zn in $CsSnI_3$ (reproduced with permission from *J. Mater. Chem. A*, **10**, 23204–23211. Copyright 2022 Royal Society of Chemistry),[74] and (c) GeI_2 in $CsPbI_3$ (reproduced with permission from *Adv. Energy Mater.*, **12**(10), 2103690. Copyright 2022 Wiley-VCH GmbH).[73]

Table 2 Stability enhancement *via* additive engineering

No.	Strategy	Structure	Type	PCE	Stability	Ref.
1	Antioxidant	FTO/TiO_2/$CsPbI_3$:FBTH/spiro-OMeTAD/Au	NIP	21.41	85.63% for 200 h@MPP/1 sun illumination/encapsulated 93.1% for 280 h@*T*: 85 °C/N_2 92.6% for 900 h@ambient air/non-encapsulated	80
2		ITO/NiO_x/$CsSnI_3$:CBZ/ZnO/PCBM/Ag	PIN	11.21	90% for 650 h@MPP/1 sun illumination/*T*: 65 °C/N_2 100% for 60d@N_2	81
3		FTO/NiO_x/$CsPb_{0.6}Sn_{0.4}I_3$:4AMPI$_2$: acetylhydrazine/PCBM/BCP/Ag	PIN	15.04	90% for 1000 h@MPP/1 sun illumination/N_2 100% for 850 h@pure O_2 T : RT 3500 h@N_2	82
4		FTO/TiO_2/$CsPbI_{3-x}Br_x$/OMe-SP/spiro-OMeTAD/Au	NIP	22.2	90.70% for 1000 h@MPP/1 sun illumination/N_2 94.45% for 170 h@UV/ambient air/non-encapsulated 95.03% for 840 h@ambient air/non-encapsulated	83
5		FTO/PEDOT:PSS/$CsPb_{0.55}Sn_{0.45}I_{2.4}B_{r0.6}$: acrylamide/PCBM/BCP/Ag	PIN	14.17	90% for 200 h@MPP/1 sun illumination/*T*: 65 °C/N_2 70% for 500 h@*T*: 65 °C/N_2	84
6	Crystallization regulation	ITO/PEDOT:PSS/Me-4PACz/$CsPbI_3$:EAL/PCBM/C_{60}/BCP/Ag	PIN	21.08	98% for 600 h@MPP/1 sun illumination/N_2 90% for 140 h@*T*: 60 °C/N_2 95% for 1680 h@N_2	85
7		FTO/TiO_2/$CsPbI_3$:[PPN][TFSI]/spiro-OMeTAD/Au	NIP	20.64	88% for 1000 h@MPP/1 sun illumination/N_2 72% for 1000 h@*T*: 85 °C/N_2 82% for 1000 h@ambient air/*T*: 25 °C RH:20–30%/ non-encapuslated	86
8		FTO/TiO_2/$CsPbI_3$:GDY//spiro-OMeTAD/Au	NIP	20.49	96.7% for 500 h@MPP/1 sun illumination/N_2 97.5% for 500 h@*T*: 65 °C/N_2	87
9		FTO/TiO_2/$CsPbI_{2.85}Br_{0.15}$:PHSF/spiro-OMeTAD/Au	NIP	20.16	82.9% for 600 h@MPP/1 sun illumination/N_2 81.7% for 65 h@*T*: 70 °C/ambient air/non-encapsulated 87.7% for 60d/ambient air/non-encapsulated	88
10		ITO/$NiiO_x$/CbzNaph/$CsPb(I_xBr_{(1-x)})_3$:(AQS:FPEA)/C_{60}/BCP/Ag	PIN	18.59	94% for 1000 h@MPP/1 sun illumination/*T*: 45 °C/N_2	89
11		ITO/PEDOT:PSS/$CsPb_{0.5}Sn_{0.5}I_2Br$:PbS/PCBM/Ag	PIN	8.03	90% for 400 h@Ar	90
12		ITO/PEDOT:PSS/$CsPb_{0.7}Sn_{0.3}I_3$:1-4FP/PCBM/PEI/Ag	PIN	17.19	91% for 48 h@RH: 50–60%/*T*: ambient RT/non-encapsulated Around 100% for 4000 h@N_2/non-encapsulated	91
13		FTO/c-TiO_2/mp-TiO_2/$CsSnI_3$:EMIMAc/Al_2O_3/NiO_x/carbon	PIN	8.54	64% for 78 h@*T*: RT RH: 60%/non-encapsulated 94% for 2160 h@N_2	92
14	Defect passivation	FTO/TiO_2/$CsPbI_3$:DED/spiro-OMeTAD/Au	NIP	21.15	92.8% for 250 h@1 sun illumination/N_2 94.9% for 1000 h@ambient air/non-encapsulated	93
15		ITO/SnO_2/$CsPbI_{2.85}Br_{0.15}$:PC/ODADI/spiro-OMeTAD/Au	NIP	22.07	90.89% for 450 h@MPP/1 sun illumination/ *T*: 25 °C RH: 25%/non-encapsulated 92.79% for 600 h@RH 15–25%/*T*: 25 °C 90.10% for 100 h@*T*: 65 °C/N_2 96.34% for 1000 h@N_2	94
16		FTO/TiO_2/$CsPbI_3$:RBITC/spiro-OMeTAD/Au	NIP	20.95	93.6% for 100 h@MPP/1 sun illumination/encapsulated 86.02% for 500 h@*T*: 60 °C/N_2	95
17		ITO/NiO_x/$CsPbI_{2.85}Br_{0.15}$:5-MVA/PCBM/BCP/Ag	PIN	20.82	90% for 500 h@*T*: 85 °C/N_2 90% for 2000 h@ambient air/*T*: 25 °C RH: 25%/non-encapsulated	96

Table 2 (*Contd.*)

No.	Strategy	Structure	Type	PCE	Stability	Ref.
18		FTO/TiO_2/$CsPbI_3$:EMIMHSO$_4$/spiro-OMeTAD/Au	NIP	20.01	95% for 1000 h@ambient air/non-encapsulated	97
19		FTO/SnO_2/$CsPbI_3$:$Zn(C_6F_5)_2$/spiro-OMeTAD/Au	NIP	19	98% for 700 h@ambient air/non-encapsulated	98
20		ITO/NiO_x/$CsPb_{0.6}Sn_{0.4}I_2Br$:DCD/ZnO/PCBM/Ag	PIN	14.17	92% for 600 h@MPP/1 sun illumination/N_2 60% for 1200 h@MPP/1 sun illumination/*T*: 65 °C 80% for 45 d@*T*: 85 °C/N_2 95% for 60d@N_2	99
21		ITO/NiO_x/$CsPb_{0.7}Sn_{0.3}I_3$:(1-4FP)/PCBM/ZrAcac/Ag	PIN	17.551	90% for 700 h@1 sun illumination 100% for 400 h@N_2	24
22		ITO/PEDOT:PSS/$CsSnI_3$:PTM/ICBA/BCP/Ag	PIN	10.1	81.3% for 2000 min@MPP/1 sun illumination/*T*: 70 °C, RH: 30%/encapsulated 83.4% for 45 d@*T*: RT, RH: 30%/non-encapsulated 94.3% for 60 d@N_2	100
23		FTO/c-TiO_2/mp-TiO_2/$CsSnI_3$:MBAA/P3HT/Au	NIP	7.5	58.4% for 120 h@1 sun illumination/*T*: 45 °C, RH: 10%/non-encapsulated 25.2% for 600 h@*T*: RT, RH: 10%/non-encapsulated 76.5% for 1440 h@N_2	101
24		FTO/c-TiO_2/mp-TiO_2/$CsSnI_3$:CPT/Al_2O_3//NiO_x/carbon	NIP	8.03	86% for 120 h@*T*: RT, RH: 60%/encapsulated 90% for 3000 h@N_2	102
25	Moisture barrier	FTO/TiO_2/$CsPbI_3$:CSE/spiro-OMeTAD/Au	NIP	21.8	97% for 440 h@MPP/1 sun illumination/encapsulated 90% for 1500 h@ambient air/non-encapsulated	103

small fractions of Zn^{2+} ions, saturating at 5% in the final perovskite lattice, affording enhanced inherent stability, as shown in Fig. 8b. The zinc incorporated $CsSnI_3$ perovskite film achieved 8.27% PCE with a carbon electrode and retained 86.3% PCE after 216 hours of storage in air without encapsulation.

Padture *et al.* demonstrated a stable lead-free perovskite light absorber through Sn and Ge alloys. A solid solution perovskite of $CsSn_xGe_{1-x}I_3$ was prepared to stabilize the Goldschmidt tolerance factor and octahedral factor.[73] The optimal inherent structural and chemical stability was achieved in $CsSn_{0.5}Ge_{0.5}I_3$, which retained the perovskite crystal structure even after exposure to humid air for 72 hours as shown in Fig. 8c. The $CsSn_{0.5}Ge_{0.5}I_3$ film was prepared through vacuum thermal evaporation of the alloy powder, and the successful Ge incorporation in the resulting film was confirmed with the optical bandgap reaching 1.50 eV. Notably, the Ge incorporated film spontaneously forms native GeO_2 oxide at the surface when exposed to air, providing a passivation layer against detrimental oxygen and moisture. Accordingly, the $CsSn_{0.5}Ge_{0.5}I_3$ alloy perovskite solar cell exhibited promising storage stability in air without encapsulation, maintaining 91% of its initial PCE after 100 hours, and demonstrated excellent operational stability, maintaining 92% of its initial PCE after 500 hours of continuous operation in an inert environment.

3.1.3 X-site engineering. Similarly, Zhang *et al.* utilized halide compositional engineering by introducing perovskite-like product NH_4PbX_3 into the inorganic precursor solution for reinforcing the device stability.[77] During the annealing process, the volatile ammonium halide salt evaporates from the film, leaving the residual $CsPbICl_{2-x}Br_x$ composite at the inorganic $CsPbI_3$ perovskite surface observed from photoluminescence spectra along the incident angle. $CsPbICl_2$ exhibits robust ionic bond strength, requiring a higher bond dissociation energy of 1.37 eV into CsX and PbX_2, compared to the 1.04 eV of $CsPbI_3$. The composite film with the mixed halide demonstrated excellent film stability under ambient conditions and light exposure stress as shown in Fig. 7b. Accordingly, the $CsPbI_3$ perovskite solar cell with $CsPbICl_{2-x}Br_x$ exhibits 20.2% PCE, while maintaining 95% of its original performance at the maximum power point for 1000 hours.

Min *et al.* also adopted halide compositional engineering by introducing CsCl within the precursor solution for stability enhancement of $CsPbI_3$ perovskite solar cells.[76] According to the time-of-flight secondary ion mass spectrometry spectra and X-ray diffraction pattern, the chloride ions remain at the bottom buried layer during the film formation stage, establishing a spontaneous $Cs_2PbI_2Cl_2/CsPbI_3$ interface. The as-grown $CsPbI_3$ film exhibits suppressed trap density and superior film crystallinity, contributing to the film stability. Moreover, the superior thermodynamic stability of the $Cs_2PbI_2Cl_2$ interlayer inhibits the δ-$CsPbI_3$ phase transition predominant at the buried interface during exposure to humid environments as shown in Fig. 7c. Thus, the $CsPbI_3$ perovskite solar cell with CsCl incorporation exhibits 20.6% PCE, maintaining approximately 80% of its initial performance after 1000 hours of light exposure in a N_2 environment.

3.2 Additive engineering

Another promising strategy to improve stability of inorganic perovskites is to incorporate additives into the perovskite precursor solution that engage in regulating the preparation, formation and preservation of the resulting perovskite films. To regulate prominent defect states, modulate the crystallization process, and protect against external stress, a wide range of molecules such as ionic salts, ionic liquids, Lewis bases, and semiconducting molecules with various functionalities have been explored (Table 2).[24,80–103]

3.2.1 Antioxidant. Yan *et al.* introduced a bifunctional reductive Lewis base carbazide molecule in the $CsSnI_3$ perovskite to simultaneously ameliorate the crystallization process and suppress trap states within the resulting perovskite film.[81] The carbazide molecule exhibited effective reduction capability of the detrimental Sn^{4+} ions in the precursor and the resulting film, as shown in Fig. 9a. The remnant carbazide molecule is

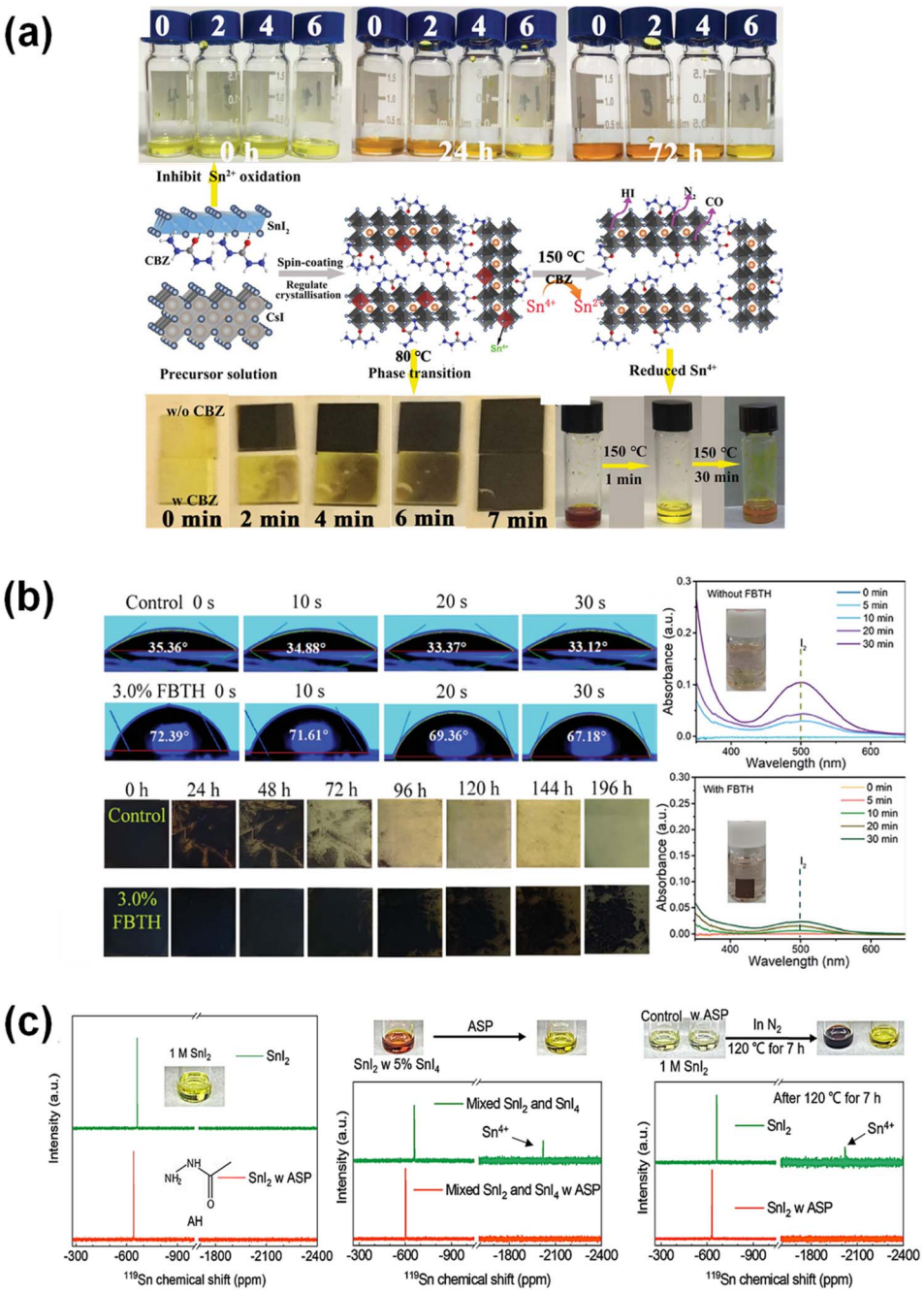

Fig. 9 The review of stability enhancement *via* additive engineering with (a) carbazide molecule in $CsSnI_3$ (reproduced with permission from *Adv. Mater.*, **35**(26), 2300503. Copyright 2023 Wiley-VCH GmbH),[81] (b) 4-fluorobenzothiohydrazide in $CsPbI_3$ (*Adv. Funct. Mater.*, **34**(10), 2312638. Copyright 2023 Wiley-VCH GmbH),[80] and (c) acetylhydrazine in $CsPb_{0.6}Sn_{0.4}I_3$ (reproduced with permission from *J. Energy Chem.*, **72**, 487–494. Copyright 2022 Elsevier).[82]

continuously consumed in the film state to prevent oxidation, resulting in suppressed deep trap states in the final $CsSnI_3$ perovskite film. Moreover, the lone pair electron of the carbon and nitrogen atom coordinates with the Lewis acidic Sn atoms, regulating the rapid crystallization process. Thus, the $CsSnI_3$ perovskite film prepared with the carbazide molecule exhibited smooth and dense morphology with large crystalline grains, imparting decreased crystallographic and chemical defects. The $CsSnI_3$ perovskite solar cell with carbazide retained 90% and 80% of its initial performance during 650 hours of maximum power point (MPP) tracking at 65 °C and during 100 hours of storage in ambient air, respectively.

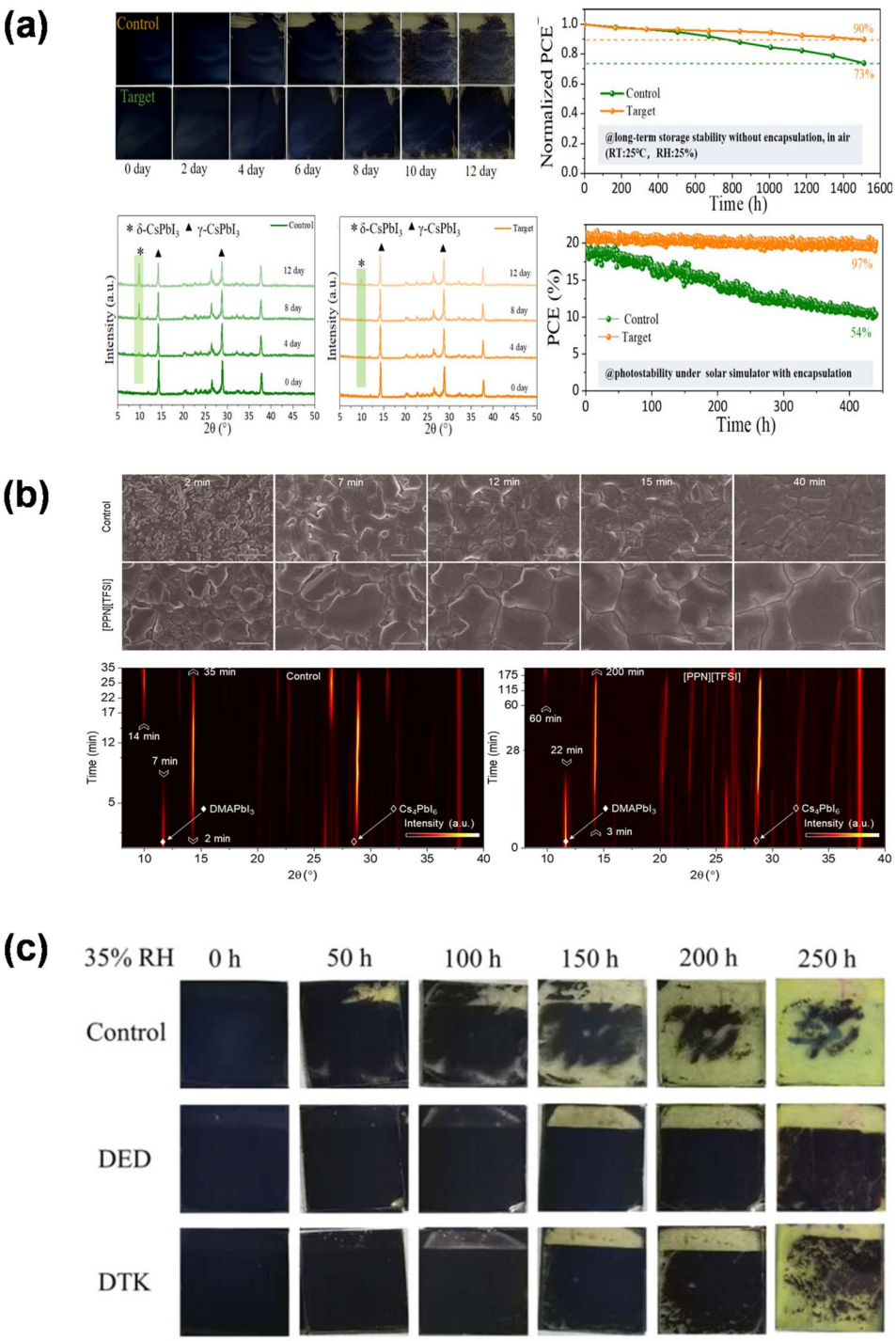

Fig. 10 The review of stability enhancement *via* additive engineering with (a) CSE in $CsPbI_3$ perovskite (reproduced with permission from *ACS Energy Lett.*, **9**(10), 4817–4826. Copyright 2024 American Chemical Society),[103] (b) [PPN][TFSI] in $CsPbI_3$,[86] and (c) DED in $CsPbI_3$ (reproduced with permission from *Adv. Mater.*, **35**(12), 2210223. Copyright 2023 Wiley-VCH GmbH).[93]

Similarly, Liu *et al.* incorporated a 4-fluorobenzothiohydrazide (FBTH) molecule in $CsPbI_3$ perovskite solar cells to stabilize the redox reaction during aging and to passivate defects in the final perovskite film.[80] Owing to the Lewis acidic F, S, and N atoms, the FBTH additive stabilizes the precursor solution, maintaining uniform colloidal size distribution during storage and regulating the crystallization process, enhancing film morphology with larger grain size. Moreover, the FBTH molecule acts as an effective redox agent to suppress I_2 and Pb^0 formation during aging of the $CsPbI_3$ perovskite film. In addition, the enhanced hydrophobicity of FBTH further contributes to the phase stability of the resulting film as shown in Fig. 9b. As a result, the $CsPbI_3$ perovskite solar cell prepared with TBFH demonstrated 92.6% and 85.63% PCE retention during 900 hours of storage and during 200 hours of operation at the MPP, respectively.

Yang *et al.* reported an acetylhydrazine additive in the $CsPb_{0.6}Sn_{0.4}I_3$ perovskite precursor solution to demonstrate an antioxidative solution processing method.[82] The Sn^{2+} ions in the precursor solution are susceptible to spontaneous oxidation to the Sn^{4+} oxidation state, resulting in abundant deep trap states in the control film. The acetylhydrazine addition successfully reduces the Sn^{4+} oxidation states to desirable Sn^{2+} states and further prevents oxidation under thermal stress, as shown in Fig. 9c. The acetylhydrazine incorporation successfully suppresses trap states in the resulting film and further protects the resulting $CsPb_{0.6}Sn_{0.4}I_3$ film from oxidation in ambient air owing to the favorable adsorption energy on the perovskite surface compared to oxygen molecules. Accordingly, the $CsPb_{0.6}Sn_{0.4}I_3$ perovskite solar cell with acetylhydrazine demonstrates excellent storage stability in an N_2 environment for 3500 hours and in an ambient environment for 85 hours and further exhibits remarkable operational stability, maintaining 90% of its initial PCE for 1000 hours of operation.

3.2.2 Crystallization regulation. Nazeeruddin *et al.* incorporated ionic liquid additive, bis(triphenylphosphine)iminium bis(trifluoromethylsulfonyl)imide ([PPN][TFSI]), in the $CsPbI_3$ perovskite precursor solution to enhance both performance and stability of inorganic perovskite solar cells.[86] [PPN][TFSI] is composed of a bulky $[PPN]^+$ cation and a weakly coordinating hydrophobic $[TFSI]^-$ anion and substantially retards the solid-state ion exchange reaction between Cs_4PbI_6 and the $DMAPbI_3$ intermediate. The addition of [PPN][TFSI] delays the formation of γ-$CsPbI_3$ by forming a $[PPN]PbI_3$ intermediate phase, prolonging the conversion process up to 200 minutes as shown in Fig. 10b. Furthermore, the [PPN][TFSI] molecules act simultaneously as passivation agents and as a moisture barrier through Pb–O interactions at the surface, stabilizing the desirable photoactive γ-$CsPbI_3$ phase. As a result, the $CsPbI_3$ perovskite solar cell exhibited excellent ambient and thermal storage stability and operational stability, maintaining 88% of its initial PCE after 1000 hours.

3.2.3 Defect passivation. Liu *et al.* introduced an acyloin ligand, 1,2-di(thiophen-2-yl)ethane-1,2-dione (DED), in a $CsPbI_3$ perovskite solar cell as a simultaneous phase stabilizer and a defect passivator.[93] The lone pair electrons in C=O and the S functional group coordinate with the undercoordinated Pb^{2+} atoms, exhibiting strong bidentate features, binding with 2 Pb atoms per DED molecule. The DED molecule effectively suppresses trap states by inhibiting Pb^{2+} vacancies with higher formation energy reaching 2.715 eV compared to the 0.951 eV formation energy of the V_{Pb}. Owing to its passivating role, the ion conductivity of the modified $CsPbI_3$ film with DED is substantially inhibited. The $CsPbI_3$ perovskite film with the DED additive exhibited a higher activation energy of ion migration of −0.51 eV compared to −0.34 eV of pristine $CsPbI_3$, increasing ion migration barrier energy to suppress the phase transition. Accordingly, the $CsPbI_3$ perovskite film and device presented excellent moisture stability as shown in Fig. 10c and maintained 92.8% of its initial performance for 250 hours of continuous light exposure.

3.2.4 Moisture barrier. Liu *et al.* introduced a 1,2-bis(-chlorodimethylsilyl)ethane (CSE) multifunctional additive in a $CsPbI_3$ perovskite solar cell to reinforce stability.[103] The CSE molecule manipulates the film formation process by contributing to the perovskite precursor colloidal migration through liquid state transport and further retards the crystallization process with low vapor pressure, providing larger grain size and fewer pinholes. The CSE molecules also exhibit an effective passivation role of the under-coordinated Pb cation filling up the V_I-related defects through Pb and Cl atom interaction, resulting in suppressed deep-level trap states. Moreover, CSE undergoes hydrolytic polymerization, forming Si–O bonds under exposure to ambient air, providing a spontaneous barrier against ambient oxygen and moisture. Accordingly, as shown in Fig. 10a, the $CsPbI_3$ perovskite solar cell with the CSE additive demonstrated excellent storage stability, maintaining 90% of its original PCE in ambient air for 1500 hours without encapsulation and 97% of its initial performance during 400 hours of operation with encapsulation.

3.3 Surface post-treatment

The rapid crystallization and crystal disorder of inorganic perovskites lead to the formation of numerous defects at grain boundaries and surfaces. The defects act as sites that induce decomposition and ion migration, as well as pathways for the infiltration of oxygen and moisture, resulting in reduced stability. These issues can be mitigated through various post-treatment processes on the surface of inorganic perovskite films.

In general, post-treatment with inorganic salts[104,105] and molecules[106–112] or organic ionic salt[113–115] containing functional groups such as NH_3, $S–COO^-$, $S=O^-$, *etc.* enhances the stability by passivating defects of the perovskite surface. Additionally, surface reconstruction and the formation of an environmental protection layer through post-treatment can further improve the stability of inorganic perovskites (Table 3).

3.3.1 Surface defect passivation. As shown in Fig. 11a, Wang *et al.* passivated defects through post-treatment using $Yb(TFSI)_3$.[104] The Yb^{3+} ions interacted with iodide ions on the perovskite surface through strong electrostatic attraction, leading to the passivation of surface defects and the suppression of ion migration. It also alleviated the surface strain

Table 3 Stability enhancement *via* surface post-treatment

No.	Strategy	Structure	Type	PCE	Stability	Ref
1	Surface defect passivation	FTO/NiO_2/MeO-2PACs/$CsPbI_{3-x}Br_x$/$Yb(TFSI)_3$/PCBM/BCP/Ag	PIN	21.4%	90% for 1260 h@MPP/1 sun illumination/ambient air 86% for 350 h@*T*: 65 °C/N_2	104
2		FTO/TiO_2/$CsPbI_{3-x}Br_x$/BMBC/spiro-OMeTAD/Au	NIP	21.75%	89.3% for 120 h@*T*: 85 °C/N_2/non-encapsulated 91.8% for 720 h@RH: 20–35%/*T*: 65 °C	107
3		FTO/TiO_2/$CsPbI_{3-x}Br_x$/TFA/spiro-OMeTAD/Au	NIP	21.35%	% For 120 h@*T*: 65 °C/N_2 % For 960 h@RH: 20–35%/*T*: ambient RT	108
4		FTO/NiO_x/2PACz/$CsPbI_{2.85}Br_{0.15}$/LiF/PD/PCBM/BCP/Ag	PIN	20.24%	89.66% for 500 h@*T*: 65 °C/N_2/non-encapsulated 97.84% for 500 h@ambient air/non-encapsulated 96.48% for 1000 h@N_2/non-encapsulated	110
5		ITO/NiO_x/P3CT-N/$CsPbI_{2.85}Br_{0.15}$/BPFz/PCBM/BCP/Ag	PIN	20.22%	83.85% for 100 h@1 sun illumination/ambient air/ non-encapsulated 86.45% for 500 h@*T*: 65 °C/N_2/non-encapsulated 89.66% for 600 h@ambient air/non-encapsulated 96.15% for 1000 h@N_2/non-encapsulated	111
6		FTO/NiO_x/$CsPbI_{3-x}Br_x$/MMI/PCBM/BCP/Ag	PIN	20.6%	91% for 100 h@MPP/1 sun illumination/RH: 15–25%/ *T*: ambient/encapsulated 90% for 265 h@*T*: 65 °C/N_2/non-encapsulated 90% for 1000 h@RH: 15–25%/*T*: ambient/non-encapsulated	113
7		FTO/TiO_2/$CsPbI_3$/F_3EAI/spiro-OMeTAD/Au	NIP	20.5%	90% for 1000 h@RH: ~20%/*T*: ambient/non-encapsulated	114
8		ITO/PEDOT:PSS/$CsPb_{0.5}Sn_{0.5}I_2Br$/F-TBA/PCBM/BCP/Ag	PIN	14.01%	90% for 900 h@MPP/1 sun illumination/*T*: 55 °C/Ar/non-encapsulated 72% for 100 h@RH: 60%/*T*: ambient RT/non-encapsulated 94% for 1000 h@Ar/non-encapsulated	112
9	Surface reconstruction	ITO/SnO_2/$CsPbI_{3-x}Br_x$/CsF/spiro-OMeTAD/Au	NIP	21.02%	86% for 400 h@MPP/1 sun illumination/*T*: 40 °C/N_2/non-encapsulated	116
10		FTO/TiO_2/$CsPbI_3$/BTABr/spiro-OMeTAD/Au	NIP	21.31%	90% for 1000 h@RH: 10–15%/*T*: 25 °C/non-encapsulated Around 100% for 400 h@0.85 V/LED(6500 K) illumination/N_2/ non-encapsulated	117
11		ITO/PEDOT:PSS/$CsPb_{0.7}Sn_{0.3}I_3$/1-4FP/PCBM/PEI/Ag	PIN	17.19%	91% for 48 h@RH: 50–60%/*T*: ambient RT/non-encapsulated Around 100% for 4000 h@N_2/non-encapsulated	91
12	Environmental protection layer	FTO/TiO_2/$CsPbI_3$/APTES/spiro-OMeTAD/Au	NIP	21.42%	81% for 500 h@RH: 30%/non-encapsulated 95% for 500 h@RH: 85%/encapsulated	118
13		FTO/NiO_x/MeO-2PACz/$CsPbI_{3-x}Br_x$/MPTS/PCBM/BCP/Ag	PIN	21.00%	86% for 800 h@MPP/1 sun illumination/encapsulated 86% for 300 h@*T*: 65 °C/N_2/non-encapsulated 91% for 1000 h@RH: 40–50%/*T*: 25–30 °C/non-encapsulated	119
14		ITO/PTAA/$CsPbI_3$/Omxene/CPTA/BCP/Ag	PIN	19.69%	93.01% for 1000 h@*T*: 85 °C/N_2/non-encapsulated 72.19% for 1000 h@RH: 85%/*T*: 25 °C/non-encapsulated 90.38% for 1000 h@RH: 85%/*T*: 85 °C/encapsulated	120

tension of the inorganic perovskite. The operational stability of the Yb^{3+}-treated device maintained 90% of its initial efficiency for 1260 h under MPP tracking and continuous 1 sun illumination. Furthermore, it retained 86% of its performance for 350 h under continuous heating at 65 °C in a nitrogen environment.

As shown in Fig. 11b, Zhang *et al.* proposed a method for passivating surface defects by applying post-treatment with Boc-*S*-4-methoxy-benzyl-L-cysteine (BMBC), a molecule containing multiple functional groups.[107] The multiple Lewis bases of –NH, –S, and –C=O in BMBC formed strong interaction with undercoordinated Pb^{2+} through Lewis base–acid reactions and suppressed the formation of halide vacancies. Additionally, the *tert*-butyl group, which exhibits hydrophobic properties, was uniformly distributed on the surface, effectively preventing moisture penetration. The BMBC-treated unencapsulated

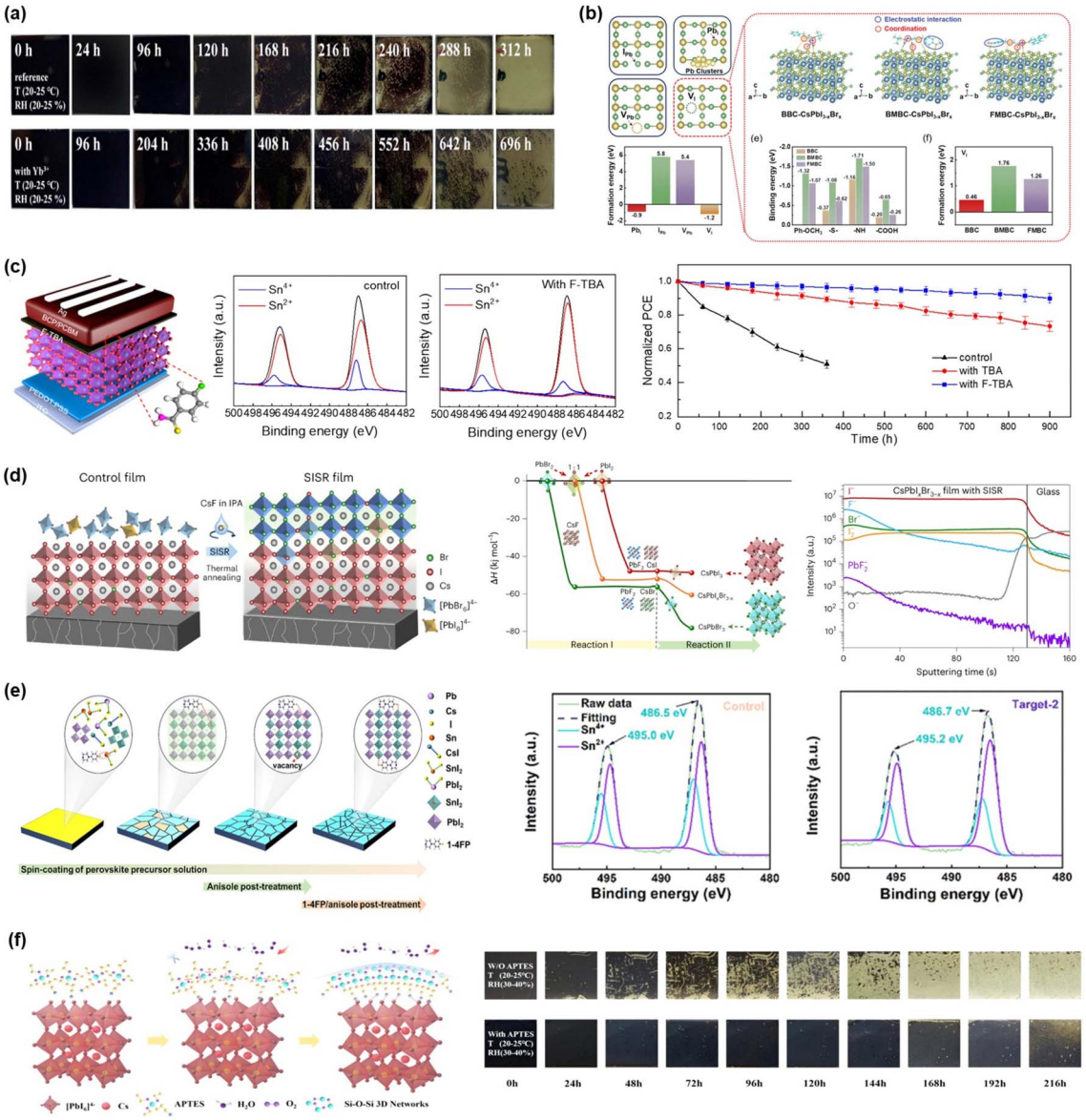

Fig. 11 The review of stability enhancement *via* surface post-treatment. (a) Post-treatment with $Yb(TFSi)_3$ on an inorganic perovskite surface (reproduced with permission from *Energy Environ. Sci.*, 2024, **17**, 7271–7280. Copyright 2024 The Royal Society of Chemistry),[104] (b) passivating surface defects by applying post-treatment with Boc-*S*-4-methoxy-benzyl-L-cysteine (BMBC) (reproduced with permission from *Adv. Mater.*, 2023, **35**, 2301140. Copyright 2023 Wiley-VCH GmbH),[107] (c) suppressing Sn^{2+} oxidation and passivating defects in inorganic Pb–Sn-based perovskite through post-treatment with 4-fluorophenylcarbothioamide (F-TBA) (reproduced with permission from *ACS Appl. Mater. Interfaces*, 2023, **15**(30), 36594–36601. Copyright 2023 American Chemical Society),[112] (d) surface defect passivation through CsF post-treatment induced surface reconstruction (reproduced with permission from *Nature Energy*, 2023, **8**, 372–380. Copyright 2023 Springer Nature),[116] (e) suppression of Sn^{2+} oxidation and defect passivation in Pb–Sn-based inorganic perovskites through surface reconstruction induced by 1-(4-fluorophenyl) piperazine (1-4FP) additive incorporation and post-treatment (reproduced with permission from *Chemical Engineering Journal*, 2024, **479**, 147554. Copyright 2023 Elsevier B.V.),[91] and (f) formation of a moisture protection layer *via* surface treatment with 3-aminopropyltriethoxysilane (APTES) (reproduced with permission from *Chemical Engineering Journal*, 2024, **497**, 154706. Copyright 2024 Elsevier B.V.).[118]

device exhibited high thermal stability, maintaining 89.3% of its initial efficiency for 120 h at 85 °C in a nitrogen-filled glovebox. Additionally, it demonstrated excellent storage stability, retaining 91.8% of its initial efficiency for 720 h at a relative humidity of 20–35% at ambient temperature.

As shown in Fig. 11c, Zhang *et al.* suggested a strategy to suppress Sn^{2+} oxidation and passivate defects in inorganic Pb–Sn perovskite through post-treatment with 4-fluorophenylcarbothioamide (F-TBA).[112] The C=S and NH_2 groups of F-TBA formed strong coordinated interactions with Sn^{2+}, suppressing its oxidation and consequently reducing defects formed by Sn^{4+}. In addition, the hydrophobic nature of fluorine enhanced moisture resistance. The F-TBA-modified cell retained 90% of its original efficiency after continuous operation at the MPP at 55 °C for 900 h and maintained over 72% of its initial performance for 100 h at 60% relative humidity at ambient temperature.

3.3.2 Surface reconstruction. As shown in Fig. 11d, Chu *et al.* reported that surface defects were passivated through surface reconstruction induced by CsF post-treatment.[116] After CsF post-treatment on the $CsPbI_xBr_{3-x}$ film, annealing induced a reaction with $CsPbX_3$, leading to halide exchange from PX_2 to PbF_2. The CsF-treated $CsPbI_x$ surface underwent a conversion to $CsPbBr_3$, which has a lower formation energy, resulting in the formation of a Br-rich perovskite surface with a more relaxed lattice on the existing inorganic perovskite. Additionally, fluoride remained on the surface by forming strong interactions with uncoordinated Pb^{2+}, effectively passivating the surface defects. The unencapsulated CsF-treated devices exhibited enhanced operational stability, retaining over 86% of their initial efficiency for 400 h under continuous bias and 1 sun illumination at around 40 °C under nitrogen atmosphere conditions.

Tan *et al.* proposed a method for passivating surface defects by applying post-treatment with benzyl trimethylammonium bromide (BTABr).[117] After post-treating the $CsPbI_3$ perovskite surface with BTABr and applying low-temperature annealing, Br^- ions diffuse into the $CsPbI_3$ film, passivating undercoordinated Pb^{2+} and inhibiting Pb cluster formation in both the bulk and on the surface of $CsPbI_3$. Moreover, through I/Br ion exchange, a gradient BTA^+–$CsPbI_{3-x}Br_x$ heterostructure was formed on the surface, improving energy level alignment. The BTABr-treated device exhibited good storage stability, maintaining over 90% of its initial efficiency for 1000 h under ambient conditions with 10–15% RH and 25 °C. Furthermore, it retained nearly 100% of its performance for 400 h under continuous white LED (6500 K) illumination and at a bias voltage of 0.85 V in a nitrogen-filled glove box.

As shown in Fig. 11e, Zhang *et al.* suggested a method to suppress Sn^{2+} oxidation and passivate defects by simultaneously applying 1-(4-fluorophenyl) piperazine (1-4FP) additive incorporation and post-treatment to Pb–Sn based inorganic perovskites.[91] The surface post-treatment with 1-4FP reconstructed the film, transforming the pinhole-rich and poorly covered Pb–Sn inorganic perovskite film into a more uniform and smoother film. Additionally, 1-4FP passivated the Sn vacancy defect by inhibiting the oxidation of Sn^{2+} through strong interaction with Sn^{2+}. The 1-4FP-treated perovskite film exhibited improved humidity and thermal stability, while the device demonstrated enhanced long-term storage stability.

3.3.3 Environmental protection layer. Inorganic perovskites exhibit high thermal stability but are vulnerable to environmental factors such as moisture and oxygen. Exposure to moisture accelerates the phase transition of $CsPbI_3$ from the black α-phase to the non-photovoltaic yellow δ-phase, which subsequently induces the degradation of the perovskite device and reduces its stability. Therefore, to enhance device stability, a protective layer is required to shield the perovskite layer from environmental factors without compromising the device's electrical properties.[118–121]

As shown in Fig. 11f, Li *et al.* demonstrated an *in situ* surface reconstruction using siloxane surfactants to form a protective layer that inhibits moisture infiltration.[118] When 3-aminopropyltriethoxysilane (APTES) was surface-treated on the perovskite surface, siloxanes reacted with moisture in the air to form a hydrophobic Si–O–Si cross-linked network layer, which impeded the infiltration of moisture and oxygen. The water contact angle of the APTES-treated $CsPbI_3$ film significantly increased from 52.25° to 76.5°, demonstrating enhanced hydrophobicity. Furthermore, the $-NH_2$ groups in APTES were converted to $-NH_3^+$, interacting with I^- and anchoring to non-coordinated Pb^{2+}, which demonstrated defect passivation and the suppression of ion migration. The APTES-treated inorganic perovskite film maintained the black phase for 216 h when exposed to air at 20–25 °C and 30–40% relative humidity. Additionally, the unencapsulated device retained over 80% of its initial efficiency for 500 h at around 30% relative humidity, while the encapsulated device maintained 95% of its initial efficiency for 500 h at 85% relative humidity, demonstrating improved stability.

Hea *et al.* synthesized OMXene plates by oxidizing $Ti_3C_2T_x$ MXene and applied them as a surface post-treatment on $CsPbI_3$ to form a physical protective layer that prevents moisture ingress.[120] By adjusting the oxidation time of MXene, OMXene with a TiO_2 electron-transporting shell on its surface was synthesized. As a result, the electron selectivity was enhanced and the formation of a strong electric field at the OMXene interface improved charge extraction. The OMXene-treated $CsPbI_3$ mini-module encapsulation demonstrated robust stability maintaining 90% of its initial efficiency at 85 °C and 85% relative humidity environments during 1 sun light soaking for 1000 h.

3.4 Interface optimization

Perovskite solar cells are fabricated with a structure in which the perovskite layer is sandwiched between charge transport layers (CTLs), such as the hole transport layer (HTL) and the electron transport layer (ETL), and are classified as n–i–p or p–i–n depending on the stacking order of the CTL and perovskite layer.

At the CTL/perovskite interface, various factors contribute to the degradation of the perovskite film and device performance. These include defects such as oxygen vacancies in the CTL and

Table 4 Stability enhancement *via* interface optimization

No.	Strategy	Structure	Type	PCE	Stability	Ref
1	ETL interface	FTO/TiO_2/DCB(SA)/$CsPbI_3$/spiro-OMeTAD/Ag	NIP	21.86%	91.1% for 300 h@1 sun illumination/non-encapsulated 87.1% for 720 h@RH: 35 ± 5%/non-encapsulated	122
2		FTO/TiO_2/ATFC/$CsPbI_3$/spiro-OMeTAD/Au	NIP	21.11%	99.37% for 350 h@MPP/1 sun illumination/RH: ∼30%/N_2/encapsulated 95.48% for 120 h@*T*: 65 °C/N_2/non-encapsulated 92.47% for 800 h@RH: 30–35%/*T*: 25 °C/non-encapsulated	123
3		FTO/TiO_2/MOCs/$CsPbI_3$/spiro-OMeTAD/Au	NIP	20.67%	94% for 800 h@RH: 20–30%/non-encapsulated	124
4		FTO/TiO_2/18C6/$CsPbI_3$/spiro-OMeTAD/Au	NIP	22.14%	95% for 1500 h@MPP/1 sun illumination/*T*: 50–55 °C/N_2/non-encapsulated 95% for 1500 h@RH: <10%/*T*: 25 °C/non-encapsulated	125
5		FTO/TiO_2/SPA/$CsPbI_3$/OAI/spiro-OMeTAD/Au	NIP	20.98%	80% for 400 h@1 sun illumination/N_2/non-encapsulated >90% for 200 h@*T*: 80 °C/N_2/non-encapsulated 91% for 1500 h@RH: 20–30%/*T*: 20–30 °C/non-encapsulated	126
6		FTO/NiO_x/$CsPb_{0.6}Sn_{0.4}I_3$:4AMPI$_2$/SnOx/PCBM/BCP/Ag	PIN	16.79%	>90% for 958 h@MPP/1 sun illumination/N_2/non-encapsulated	127
7	HTL interface	FTO/NiO_x/Br-2PACz/$CsPbI_3$/PCBM/BCP/Ag	PIN	19.34%	89% for 284 h@MPP/1 sun illumination/N_2/non-encapsulated 73% for 48 h@*T*: 60 °C/non-encapsulated 80% for 960 h@RH: 30–35%/non-encapsulated	128
8		ITO/NiO_x/2PACz/TPAI/$CsPbI_3$/PCBM/BCP/Ag	PIN	21.60%	96.71% for 1400 h@MPP/1 sun illumination/RH: ∼30%/encapsulated 95.88% for 2000 h@RH: 30–35%/non-encapsulated	129
9		ITO/NiO_x/MeO-2PACz/$NbCl_5$/$CsPbI_3$/PCBM/BCP/Ag	NIP	21.24%	92.27% for 1000 h@MPP/1 sun illumination/RH: 30–35%/encapsulated 97.61% for 1000 h@RH: 35%/*T*: 25 °C/non-encapsulated	130
10		FTO/TiO_2/$CsPbI_{3-x}Br_x$/spiro-OMeTAD:TA/Au	NIP	21.80%	83% for 250 h@*T*: 65 °C/N_2/non-encapsulated 90% for 800 h@RH: 25–35%/non-encapsulated	131
11		FTO/TIO_2/$CsPbI_3$/spiro-OMeTAD:BPFPDS/Au	NIP	21.95%	98% for 1200 h@MPP/1 sun illumination/RH: 30%/*T*: 85 °C/encapsulated 89% for 300 h@*T*: 65 °C/non-encapsulated 96% for 3000 h@RH: 15–20%/non-encapsulated	132
12	Low-dimension heterostructure	FTO/TiO_2/Al_2O_3/$CsPbI_3$/$Cs_2PbI_2Cl_2$/CuSCN/Cr/Au	NIP	17.4%	80% for 2100 h@MPP/120 mW cm^{-2}/RH: 65 ± 26%/*T*: 110 °C/encapsulated	133
13		ITO/PTAA/$CsPbI_3$/Cs_4PbBr_6/CPTA/BCP/Ag	PIN	21.03	92.48% for 1000 h@MPP/1 sun illumination/RH: 85%/*T*: 85 °C/encapsulated 76.33% for 1000 h@MPP/1 sun illumination/non-encapsulated 66.03% for 1000 h@MPP/1 sun illumination/RH: 85%/non-encapsulated	134
14		FTO/c-TiO_2/$CsPbI_{2.75}Br_{0.25}$/NPA 2D-RP/P3HT/Ag	NIP	19.77	93.2% for 1200 h@MPP/1 sun illumination/RH: 25%/*T*: 25 °C/encapsulated 87.8% for 1200 h@MPP/1 sun illumination/N_2/*T*: 20 °C/encapsulated 88.9% for 1200 h@MPP/1 sun illumination/*T*: 80 °C/N_2/encapsulated	135
15	Overcoming the hygroscopic additive (HTM free/carbon electrode)	FTO/TiO_2/m-Al_2O_3/$CsPbI_3$/CF_3-PAI/carbon	NIP	18.33	87.7% for 200 h@MPP/1 sun illumination/N_2/non-encapsulated 90% for 1000 h@RH: <20%, *T*: 10–30 °C/non-encapsulated	136
16		FTO/TiO_2/$CsPbI_3$/TChI/carbon	NIP	19.08	91.5% for 300 h@MPP/1 sun illumination/N_2/non-encapsulated 93.2% for 100 h@MPP/1 sun illumination/RH: 65 ± 5%/encapsulated 91.5% for 300 h@*T*: 65 °C/N_2/non-encapsulated	137

uncoordinated Pb^{2+} in the perovskite interface, chemical reactions with the CTL and perovskite, nonuniform perovskite film growth caused by CTL surface roughness and aggregation, lattice mismatch, inadequate adhesion between the CTL and perovskite layer, and energy-level mismatch leading to charge accumulation. To address these issues occurring at the CTL/perovskite interfaece, it is necessary to optimize the interface through various strategies (Table 4).

3.4.1 ETL interface optimization. In n–i–p structure inorganic perovskite solar cells, metal oxide ETLs such as SnO_2 and TiO_2 are commonly used. However, oxygen vacancies are present on the surface of metal oxide ETLs, and upon UV exposure, they act as photocatalysts, accelerating the degradation of the perovskite layer. Perovskite defects at the ETL/perovskite interface increase recombination and impede charge transport, leading to charge accumulation, which ultimately contributes to the degradation of device performance and stability.[122–126,138,139]

As shown in Fig. 12a, Qiu *et al.* adapted dipolar chemical bridge (DCB) materials at the ETL/inorganic perovskite interface.[122] The DCB material, 3-amino-1-propane-sulfonic acid (SA), generated a strong electric field at the interface, optimizing the interfacial energy-level alignment and facilitating charge extraction. SA passivated defects through strong interactions

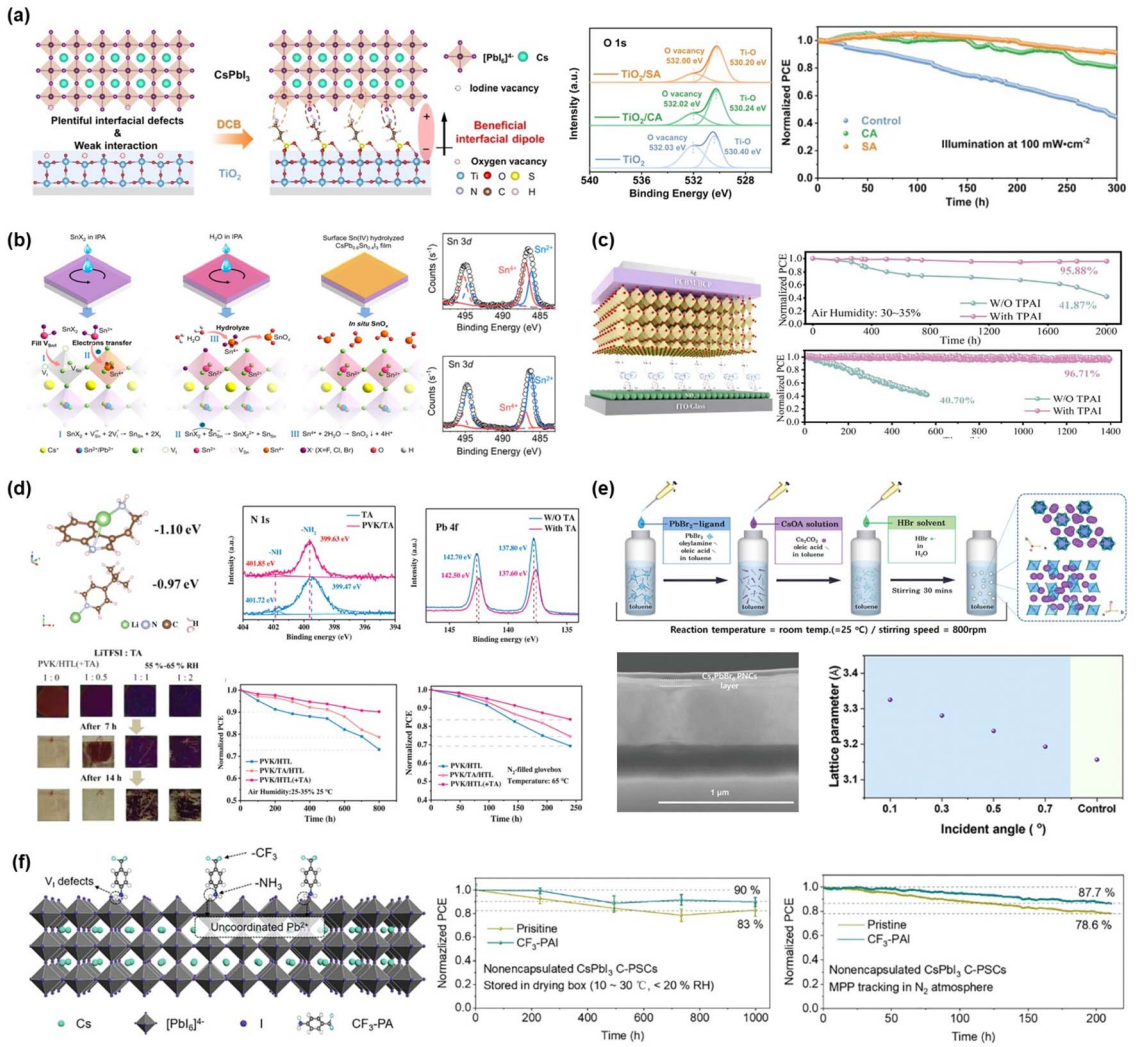

Fig. 12 The review of stability enhancement *via* interface optimization. (a) ETL/inorganic perovskite interface optimization *via* TiO_2 surface treatment with 3-amino-1-propane-sulfonic acid (SA) (reproduced with permission from *Angew. Chem. Int. Ed.* 2024, **63**, e202401751. Copyright 2024 Wiley-VCH GmbH),[112] (b) suppression of Sn^{2+} oxidation and *in situ* formation of a SnO_2 ETL *via* the surface Sn(IV) hydrolysis (SSH) technique in Pb–Sn-based inorganic perovskite solar cells (reproduced with permission from *ACS Energy Lett.*, 2023, **8**(2), 1035–1041. Copyright 2023 American Chemical Society),[127] (c) modification of the SAM surface with 4-(aminomethyl)-*N*,*N*-diphenylaniline iodide (TPAI) to suppress SAM aggregation and improve molecular ordering (reproduced with permission from *Angew. Chem.*, 2025, e202502221. Copyright 2025 Wiley-VCH GmbH),[129] (d) suppression of Li^+ ion migration and passivation of perovskite interface defects by incorporating the biocompatible molecule tryptamine (TA) into the HTL (reproduced with permission from *Adv. Mater.*, 2024, **36**, 2306982. Copyright 2023 Wiley-VCH GmbH),[131] (e) surface defect passivation, lattice strain buffering, and environmental barrier effect achieved by forming a 3D/0D heterostructure through deposition of 0D Cs_4PbBr_6 nanocrystals on $CsPbI_3$ (reproduced with permission from *Adv. Mater.*, 2024, **36**, 2408387. Copyright 2024 Wiley-VCH GmbH),[134] and (f) optimization of the $CsPbI_3$/carbon interface in HTM-free devices *via* CF_3-PAI interface treatment (reproduced with permission from *Small*, 2024, **20**, 2402061. Copyright 2024 Wiley-VCH GmbH).[136]

with uncoordinated Ti^{4+} on the TiO_2 surface, I^- ions and uncoordinated Pb^{2+} in the buried perovskite interface. Furthermore, by enhancing the contact with the perovskite, it effectively reduced non-radiative recombination. Furthermore, the interface treatment with SA improved the crystallinity and relieved tensile strain of the inorganic perovskite, thereby enhancing the durability of the inorganic perovskite film. The SA-treated unencapsulated device maintained 87.1% of its initial efficiency after 720 h of storage at 35 ± 5% RH. Additionally, it retained 91.1% of its initial efficiency after 300 h of operation under continuous 100 mW cm^{-2} illumination.

As shown in Fig. 12b, Hu *et al.* applied the surface Sn(IV) hydrolysis (SSH) technique in Pb–Sn based inorganic perovskite solar cells to suppress Sn^{2+} oxidation and form an *in situ* SnO_2 ETL, thereby enhancing charge transport and extraction.[127] As a first step, SnF_2 was coated onto the perovskite surface to reduce Sn^{4+} to Sn^{2+}, while also inducing Sn^{2+} to fill defects on the surface. Subsequently, a second surface treatment was performed using an IPA solution containing a trace amount of H_2O, forming an ultrathin SnO_2 film. The *in situ* SnO_2 film formed through secondary treatment suppressed the oxidation of Sn^{2+} in Pb–Sn based inorganic perovskites and improved energy-level alignment, resulting in enhanced device stability and charge extraction capability. The unencapsulated device employing the SSH technique demonstrated long-term stability, maintaining over 90% of its initial efficiency for 958 h under 1 sun continuous illumination in a nitrogen-filled glovebox.

3.4.2 HTL interface optimization. HTL materials in conventional p–i–n structures are primarily PTAA or NiO_x. Problems such as energy-level mismatch between inorganic perovskite and the HTL, formation of poor-quality perovskite films due to the hydrophobic nature of PTAA, and chemical reactions between NiO_x and perovskite reduce the efficiency and durability of the device.

Recently, to address these issues, strategies have been reported that either replace conventional HTL materials with self-assembly materials (SAMs)[140] or enhance stability by suppressing chemical reactions through SAM surface treatment.[128] However, despite these advantages, the uneven distribution of the SAM layer due to agglomeration causes defects to form at the HTL/perovskite interface, ultimately degrading stability.[129,130]

As shown in Fig. 12c, Liu *et al.* demonstrated that the modification of 4-(aminomethyl)-*N*,*N*-diphenylaniline iodide (TPAI) to the SAM surface enhances stability.[129] TPAI bonded to the SAM through π–π interactions, suppressing SAM aggregation and improving SAM order. In addition, TPAI passivated defects at the $CsPbI_3$ surface by interacting with Pb^{2+} through its $-NH_3$ group and optimized the energy-level alignment at the HTL/perovskite interface, enhancing charge extraction and suppressing charge recombination. The TPAI-treated perovskite solar cell maintained 96.71% of its initial efficiency after 1400 h of maximum power point (MPP) tracking and retained 95.88% of its initial efficiency even after 2000 h of storage in air, demonstrating improved stability.

Another approach is to modify the HTM itself. In the case of n–i–p structured devices, the commonly used HTL, spiro-OMeTAD, contains additives such as LiTFSi to enhance its conductivity. The LiTFSi doped spiro-OMeTAD is highly sensitive to humidity and temperature variations, leading to Li^+ ion migration. Additionally, due to the high moisture affinity of Li^+ ions, it can absorb humidity and react with the perovskite layer, causing its degradation.[131,132]

As shown in Fig. 12d, Liu *et al.* proposed a method to suppress Li^+ ion migration and passivate perovskite interface defects by incorporating the biocompatible molecule tryptamine(TA) into the HTL.[131] The $-NH_2$ group of TA formed strong bonds with undercoordinated Pb^{2+} on the perovskite surface, reducing the interface defect density. Furthermore, TA formed TA:Li^+ complexes, reducing moisture absorption and suppressing Li^+ ion migration, thereby enhancing the stability of the perovskite layer. The device incorporating the TA-doped HTM maintained 90% of its initial efficiency after 800 h of storage at 25–35% RH. Additionally, in the thermal stability test, it retained 83% of its initial efficiency after 250 h at 65 °C.

3.4.3 Low-dimension heterostructure interface. Low-dimensional perovskites effectively passivate surface defects. Moreover, by capping the 3D inorganic perovskite layer, they stabilize the lattice strain, thereby suppressing ion migration and significantly enhancing phase stability.[133–135,141,142]

Zhao *et al.* formed a 2D $Cs_2PbI_2Cl_2$ capping layer on the $CsPbI_3$ surface by applying CsCI post-treatment.[133] Through CsCl surface treatment, Cl^- ions passivated I vacancy defects, while the 2D $Cs_2PbI_2Cl_2$ capping layer increased the activation energy to 0.536 eV, thereby suppressing iodide ion migration from the perovskite to the HTL under thermal and light stress, ultimately enhancing stability. The encapsulated 3D $CsPbI_3$/2D $Cs_2PbI_2Cl_2$ device demonstrated a remarkable T_{80} lifetime of 2100 h using the ISOS-L-3 protocol measured at the MPP under simultaneous light exposure (120 mW cm^{-2}) and in a heating environment at 110 °C.

As shown in Fig. 12e, Heo *et al.* synthesized 0D Cs_4PbBr_6 nanocrystals on the $CsPbI_3$ surface and subsequently applied them *via* the spray coating process, forming a 3D/0D heterostructure.[134] 0D Cs_4PbBr_6 consists of isolated $PbBr_6^{4-}$ octahedra surrounded by Cs^+ ions, effectively passivating Pb^{2+} defects on the perovskite surface. Also, the Cs_4PbBr_6 lattice spacing, similar to that of 3D perovskites, acts as a lattice strain holder, improving both phase and thermal stability. Furthermore, it has been shown to function as a barrier against environmental stress. The encapsulated device with 0D Cs_4PbBr_6 treatment retained 92.48% of its initial efficiency under simultaneous 1 sun illumination and damp heat (85 °C/85% relative humidity) for 1000 h.

3.4.4 Overcoming hygroscopic additives. The HTL contains hygroscopic components, which can absorb moisture and impact device stability. Additionally, its inherently permeable nature allows halide ions and metal ions to pass through easily, leading to the halogenation of the metal electrode.

In contrast, the chemical inertness of carbon electrodes fundamentally prevents electrode corrosion while the HTL-free structure enhances moisture resistance, thereby improving stability. However, despite these advantages, the abundant surface defects of inorganic perovskites and the low hole

selectivity of carbon electrodes lead to decreased durability and performance degradation.[136,137,143,144]

As shown in Fig. 12f, Zhang *et al.* demonstrated a method utilizing a dipole electric field at the $CsPbI_3$/carbon interface to enhance device performance and stability.[136] The $-NH_3$ group of CF_3-PAI bonded to the perovskite surface, while the $-CF_3$ group interacted with the carbon electrode. This alignment generated a well-ordered dipole electric field within the perovskite/carbon electrode interface, enhancing hole selectivity and interfacial charge separation. In addition, CF_3-PAI passivated defects by interacting with uncoordinated Pb^{2+}, which suppressed non-radiative recombination and contributed to the improvement of phase stability. The unencapsulated CF_3-PAI-treated HTM-free device maintained 90% of its initial efficiency over 1000 h under storage conditions with relative humidity below 20%. Moreover, under continuous illumination at 100 mW cm^{-2} for 200 h, it retained 87.7% of its performance, demonstrating enhanced operational stability.

Zhang *et al.*[144] and Lin *et al.*[137] treated the inorganic perovskite surface with choline iodide (ChI) and thiocholine iodide (TChI), respectively, forming a low-dimensional perovskite layer, which passivated the inorganic perovskite surface and enhanced charge extraction capability by improving energy-level alignment. In particular, Zhang *et al.*[144] enhanced stability by applying ChI in two steps, first at the wet film intermediate phase and then as a second treatment on the dried film, effectively passivating both bulk and surface defects in the inorganic perovskite.

Another strategy for overcoming the low stability induced by hygroscopic additives to the HTL is to use self-standing inorganic HTLs such as CuSCN and phthalocyanine (CuPc) that do not require hygroscopic additives.[145] Moreover, inorganic HTLs are generally more robust both mechanically and chemically, compared to soft organic HTLs such as spiro-OMeTAD, thus providing a significant advantage in long-term thermal and environmental stability.[146] Similarly, inorganic ETLs such as SnO_2 can also provide robust stability when processed on top of the perovskite layer for inverted perovskite solar cells.[147] However, the number of reports on using inorganic CTLs for all-inorganic PSCs with high stability is extremely limited, largely due to the difficulty in processing inorganic CTLs on top of the inorganic perovskite surface, and many reports on "all-inorganic PSCs" unfortunately still rely on organic top-CTLs such as spiro-OMeTAD and PCBM. It is expected that there remains a significant amount of research to be explored in the development of "true" all-inorganic PSCs with inorganic CTLs for enhanced thermal and moisture stability.

4. Strategy for efficiency enhancement

4.1 Current status and theoretical limits of efficiency

The S–Q limit[148] graph, as shown in Fig. 13, defines the theoretical maximum PCE of single-junction solar cells as a function of bandgap. Inorganic perovskites, with bandgaps tunable between 1.25 and 2.3 eV, theoretically allow efficiencies exceeding 30%. However, the current record efficiencies of inorganic perovskite solar cells remain significantly lower than the SQ-limit and are also lower than those of hybrid perovskite solar cells. The highest reported efficiency of inorganic perovskite solar cells is 22.20% (ref. 83) at a bandgap of 1.72 eV, which corresponds to approximately 80% of the SQ-limit at that bandgap, with most devices performing below this threshold. The gap between practical performance and theoretical potential demonstrates the remaining possibility for efficiency improvement in inorganic perovskite solar cells. To narrow this gap, further research is needed on enhancing efficiency through strategies such as optimization of material composition and film quality, interface engineering, defect passivation, and phase stabilization.

In particular, Sn- and Pb–Sn-based perovskites possess narrow bandgaps in the range of approximately 1.3 to 1.5 eV, which are close to the ideal bandgap of 1.34 eV for single-junction solar cells under AM1.5G illumination, and are well-suited as bottom cells in tandem architectures. Therefore, research on Sn- and Pb–Sn-based inorganic perovskites is essential not only for achieving optimal efficiency in single-junction solar cells but also for developing all-perovskite tandem solar cells that can overcome the efficiency limitations of single-junction devices while ensuring high thermal and operational stability.

4.2 Material composition and phase engineering

The strategies to boost efficiency of inorganic perovskite solar cells include compositional engineering by modifying the B site and X site ions. The introduction of external ions either partially incorporates into the perovskite lattice or constructs alternative phases to promote optoelectronic properties of the desired photoactive perovskite phases (Table 5).[37,149–170]

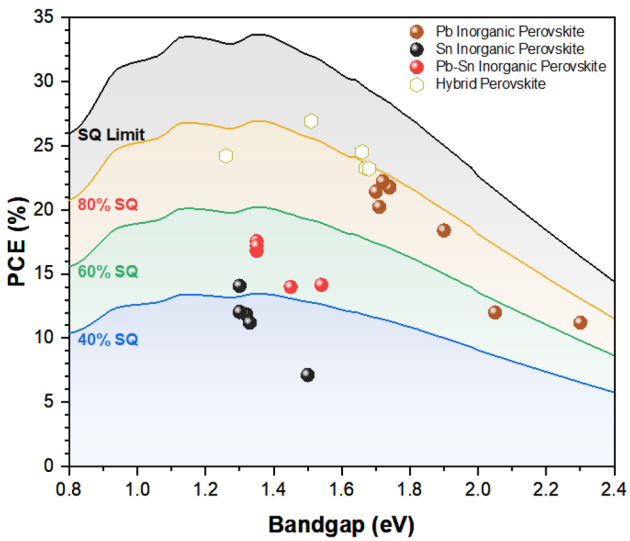

Fig. 13 The Shockley–Queisser (SQ) limit graph showing the record efficiencies of Pb-, Sn-, and Pb–Sn-based inorganic perovskites and hybrid perovskites according to bandgap energy.

Table 5 Efficiency enhancement *via* material composition and phase engineering

No.	Strategy	Structure	Type	J_{sc}	V_{oc}	FF	PCE	Ref.
1	B-site engineering	ITO/NiO_x/$CsPb_{(0.6-x)}Sn_{(0.4-x)}Mn_xI_{(3-y)}Br_y$:BHA/PCBM/ZrAcac/Ag	PIN	26.9	0.83	76.7	17.12	149
2		FTO/c-TiO_2/$CsPbI_{3-x}Br_x$:CdI_2/spiro-OMeTAD/Au	NIP	20.64	1.21	83.2	20.8	150
3		FTO/c-TiO_2/mp-TiO_2/$CsPb_{0.9}Sn_{0.1}IBr_2$/carbon	NIP	14.3	1.26	63	11.33	151
4		FTO/SnO_2/C_{60}/$CsPb_{0.75}Sn_{0.25}IBr_2$/spiro-OMeTAD/Au	NIP	12.57	1.21	75.8	11.53	152
5		FTO/c-TiO_2/mp-TiO_2/Al_2O_3/$CsPb_{0.5}Sn_{0.5}I_2$Br:TP/NiO_x/carbon	NIP	20.1	0.62	65	8.1	153
6		ITO/PEDOT:PSS/$CsPb_{0.7}Sn_{0.3}I_3$/PCBM/BCP/Ag	PIN	20.96	0.64	70.12	9.41	154
7		ITO/PEDOT:PSS/$CsPb_{0.4}Sn_{0.6}I_2Br$/PCBM/CeO_x/Ag	PIN	19.02	0.86	75.1	12.34	155
8		ITO/NiO_x/$CsSnI_{2.6}Br_{0.4}$:DMKO/PCBM/ZrAcac/Ag	PIN	20.7	0.75	72.1	11.2	156
9		ITO/PEDOT:PSS/$CsSn_{1-x}Zn_xBr_3$/C_{60}/BCP/Ag	PIN	13.99	0.35	54	2.59	157
10		ITO/PEDOT:PSS/$CsPb_{0.75}Sn_{0.25}I_3$/PCBM/bis-C_{60}/Ag	PIN	15.4	0.67	56	5.78	158
11	Phase engineering	FTO/TiO_2/SnO_2/β-$CsPbI_3$:$Zn(C_6F_5)_2$/γ-$CsPbI_3$:GAI/P3HT + SMeTAPyr/Au	NIP	21.72	1.22	81.5	21.59	159
12	X-site engineering	FTO/c-TiO_2/$CsPbI_3$:HBr/spiro-OMeTAD/MoO_3/IZO/Ag	NIP	20.34	1.22	80.36	19.89	160
13		ITO/PTAA/$CsSnI_2Br$/ICBA/BCP/Ag	PIN	22.2	0.75	71.29	11.87	37
14		ITO/PEDOT:PSS/$CsSnI_3$:CsFa/ICBA/BCP/Ag	PIN	24.94	0.75	74	13.68	161
15		FTO/TiO_2/$CsPbI_3$:CsFo/spiro-OMeTAD/Au	NIP	20.57	1.25	82.5	21.23	162
16		FTO/TiO_2/$CsPbI_3$:DMAAc/spiro-OMeTAD/Au	NIP	20.8	1.25	81.6	21.14	163
17		FTO/TiO_2/$CsPbI_3$:DMAAc/spiro-OMeTAD/Au	NIP	20.81	1.23	82.2	21.04	164
18		ITO/SnO_2/$CsPbI_{2.75}Br_{0.25}$:DMACl/CsI/spiro-OMeTAD/Au	NIP	18.86	1.356	81.15	20.75	165
19		FTO/TiO_2/$CsPbI_3$:DMAFa/spiro-OMeTAD/Au	NIP	20.49	1.21	82.02	20.4	166
20		ITO/P3CT-N/$CsPbI_3$:$PbAc_2$/PCBM/C_{60}/BCP/Ag	PIN	20.52	1.215	80.89	20.17	167
21		FTO/TiO_2/$CsPbI_2Br$/$CsPbI_{3-x}Br_x$/PTAA/Au	NIP	18.08	1.15	80.85	16.81	168
22		FTO/PEDOT:PSS/PTAA/$CsPb_{0.4}Sn_{0.6}I_{2.4}Br_{0.6}$/$C_{60}$/BCP/Ag	PIN	22.96	0.793	78.77	13.98	169
23		ITO/PEDOT:PSS/$CsPb_{0.5}Sn_{0.5}I_{2.7}Br_{0.3}$/PCBM/BCP/Ag	PIN	22.11	0.86	72.7	13.82	170

Cai *et al.* introduced a small amount of HBr acid into the $CsPbI_3$ perovskite precursor solution as a source of Br^- anions and phase regulator for preparing efficient semitransparent inorganic perovskite solar cells.[160] The Br^- additive induced a slight blue shift in the absorption edge of the perovskite film, confirming successful Br^- halide incorporation. The HBr additive induced partial formation of α-$CsPbI_3$ upon annealing at 100 °C, in contrast to γ-$CsPbI_3$ phase formation at 40 °C in the control film, thus imparting mixed α and γ phases, as shown in Fig. 14a. The co-existing mixed $CsPbI_3$ phases mitigate spontaneous strain and substrate-constrained strain from mismatching thermal expansion coefficients, thus securing photoactive $CsPbI_3$ perovskite films. Moreover, the HBr treated $CsPbI_3$ film is a uniform and dense film and demonstrated lower defect density, suppressing the detrimental non-radiative recombination. Accordingly, the $CsPbI_3$ perovskite solar cell with a transparent IZO electrode demonstrated a remarkable 19.89% PCE compared to the 17.80% PCE of the control sample.

Hong *et al.* modulated the I to Br halide ratio in $CsSnI_{3-x}Br_x$ to optimize the performance and the inherent stability trade-off relation from composition engineering to fabricate efficient inorganic lead-free perovskite solar cells.[37] The authors systematically investigated the optoelectronic characteristics of the $CsSnI_{3-x}Br_x$ film with varying I and Br halide composition through computational and experimental methods. While the I-rich composition benefitted the wider range of light absorption from lower bandgaps, the Br-rich composition favored enhanced γ-phase stability, as shown in Fig. 14b. The optimized $CsSnI_2Br$ perovskite exhibited robust lattice stability and demonstrated excellent performance, reaching 11.97% PCE through the precursor purification process and compositional engineering.

Wang *et al.* reported an anion alloying strategy in $CsSnI_3$ perovskite solar cells with pseudohalides by incorporating a cesium formate (CsFa) additive in the precursor solution.[161] The introduced Fa^- effectively suppressed the inorganic $CsSnI_3$ perovskite film through regulating the crystallization process. The Fa^--alloyed perovskite film exhibited slower crystallization by forming a low-dimensional intermediate phase and, therefore, resulted in a larger grain size and a narrower surface potential difference compared to the control $CsSnI_3$ film, as shown in Fig. 14c. Moreover, the Fa^- anions effectively passivate defects by coordinating with undercoordinated Sn^{2+} that fills the X-site vacancies and by suppressing Sn^{4+} defective oxidation states. As a result, the $CsSnI_3$ film demonstrated a remarkable certified 13.68% PCE through the pseudohalide anion alloying strategy.

Wang *et al.* investigated the ternary B-site co-doping strategy to enhance the performance of a $CsPb_{1-x-y}Sn_xB_yI_{3-z}Br_z$ perovskite composition system.[149] The B-site co-doping strategy was performed by introducing Sr^{2+}, Ge^{2+}, Zn^{2+}, and Mn^{2+} to enhance phase stability and promote light response from adjusting the optical bandgap. Among the various candidates, 4% Mn^{2+} incorporation into the B-site alloy system benefitted from the small ionic radius, increasing the Goldschmidt tolerance factor up to 0.82, favoring the photoactive black perovskite phase. Moreover, the Pb–Sn–Mn co-doped perovskite system exhibited a reduced bandgap to 1.36 eV closer to the ideal bandgap, contributing to enhanced performance reaching 14.34% PCE and phase stability, as shown in Fig. 15b. Upon further introduction of benzhydroxamic acid as an antioxidant and a passivation agent, the inorganic Pb–Sn–Mn based perovskite solar cell demonstrated excellent 17.12% PCE.

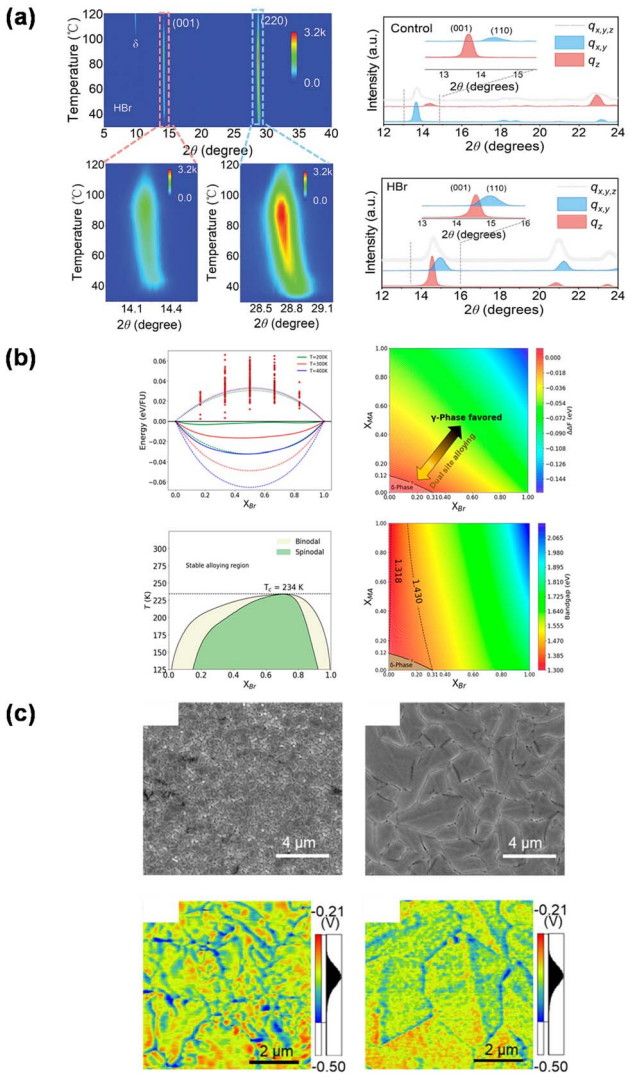

Fig. 14 The review of efficiency enhancement *via* material composition and phase engineering with (a) HBr in $CsPbI_3$ (reproduced with permission from *Small*, **21**(14), 2500710. Copyright 2025 Wiley-VCH GmbH),[160] (b) Br^- ion in $CsSnI_3$ (reproduced with permission from *ACS Energy Lett.*, **8**(12), 5061–5069. Copyright 2023 American Chemical Society),[37] and (c) formate pseudohalide anion in $CsSnI_3$ (reproduced with permission from *ACS Energy Lett.*, **9**(12), 5870–5878. Copyright 2024 American Chemical Society).[161]

Liu *et al.* introduced CdI_2 in a $CsPbI_{3-x}Br_x$ perovskite solar cell for B-site compositional engineering and for surface defect passivation.[150] The Cd^{2+} ions possess a smaller ionic radius than Pb^{2+} and, therefore, are partially substituted within the $CsPbI_{3-x}Br_x$ lattice up to 2 mol%, which reduces detrimental lattice distortion of the inorganic $[PbX_6]^{4-}$ framework. Interestingly, the excess CdI_2 additive mainly remained at the surface grain boundary in the form of $Cs_2PbI_{4-x}Br_x$, as shown in Fig. 15c, and contributed to the enhanced performance by reducing non-radiative recombination. Furthermore, the CdI_2 additive slows down the nucleation rate from increased precursor colloidal distribution and leads to the formation of larger crystal grain size with surface defect states. Accordingly, the $CsPbI_{3-x}Br_x$ perovskite solar cell with 8 mol% CdI_2 demonstrated 20.8% PCE from lattice engineering and defect control.

Hong *et al.* proposed a phase heterojunction (PHJ) with β-$CsPbI_3$ and γ-$CsPbI_3$ to prepare highly efficient $CsPbI_3$ perovskite solar cells by exploiting the $CsPbI_3$ polymorphs induced by compositional engineering.[159] The PHJ $CsPbI_3$ film was prepared by stacking the front dimethylammonium iodide-assisted β-$CsPbI_3$ perovskite along with a bis(pentafluorophenyl)zinc ($Zn(C_6F_5)_2$) additive from the solution process and the rear guanidinium iodide-assisted γ-$CsPbI_3$ perovskite from the vapor phase process. The $CsPbI_3$ polymorph stack provides a stable coherent phase-heterojunction without gap states, exhibiting favorable interfacial adhesion energy reaching -0.213 eV $Å^{-2}$ and facilitating charge extraction with favorable band alignment as shown in Fig. 15a. Accordingly, the PHJ perovskite solar cell demonstrated a remarkable maximum 21.59% PCE and 18.43% PCE from a 19.17 cm^2 active area module.

4.3 Reducing trap-induced recombination losses

All-inorganic perovskite solar cells are notoriously prone to various defects that can trap charge carriers and induce non-radiative recombination, subsequently leading to significant losses in open-circuit voltage and other drops in device performance. Accordingly, researchers have sought methods to reduce losses by defect passivation or by inhibiting defect formation. Since most defects within inorganic perovskite solar cells can form either at the perovskite interfaces or within the perovskite bulk film, defect passivation strategies have focused on identifying the types of the respective defects and using targeted molecules that can interact with and passivate the defects. Other strategies have focused on tackling the fundamental mechanism of defect formation during film fabrication, aiming towards the formation of a highly crystalline perovskite film with low defect density. Meanwhile, a layer of complexity is added when dealing with Sn-based inorganic perovskite solar cells since the problem of Sn oxidation must then be primarily addressed (Table 6).

4.3.1 Defect passivation. Trap-induced recombination loss is an unavoidable problem that must be addressed due to how easily defects can be formed within all-inorganic perovskite solar cells. During inorganic perovskite solar cell fabrication, defects are formed at either the perovskite surface, the bottom perovskite interface or the bulk perovskite film, and it is important to identify what kind of defect is present in order to design appropriate passivation strategies.

Post-treatment of the perovskite film surface is one of the most widely used methods of defect passivation, especially since the perovskite surface is most vulnerable to defect formation during thin film fabrication.[106–108,117,171,175,176] Gu *et al.* identified iodine vacancies as one of the most common types of surface defects for all-inorganic perovskite thin films and demonstrated the use of histamine (HA) to passivate the under-coordinated Pb^{2+} defects on the perovskite surface.[171] HA possesses an amine group and an imidazole ring, which could

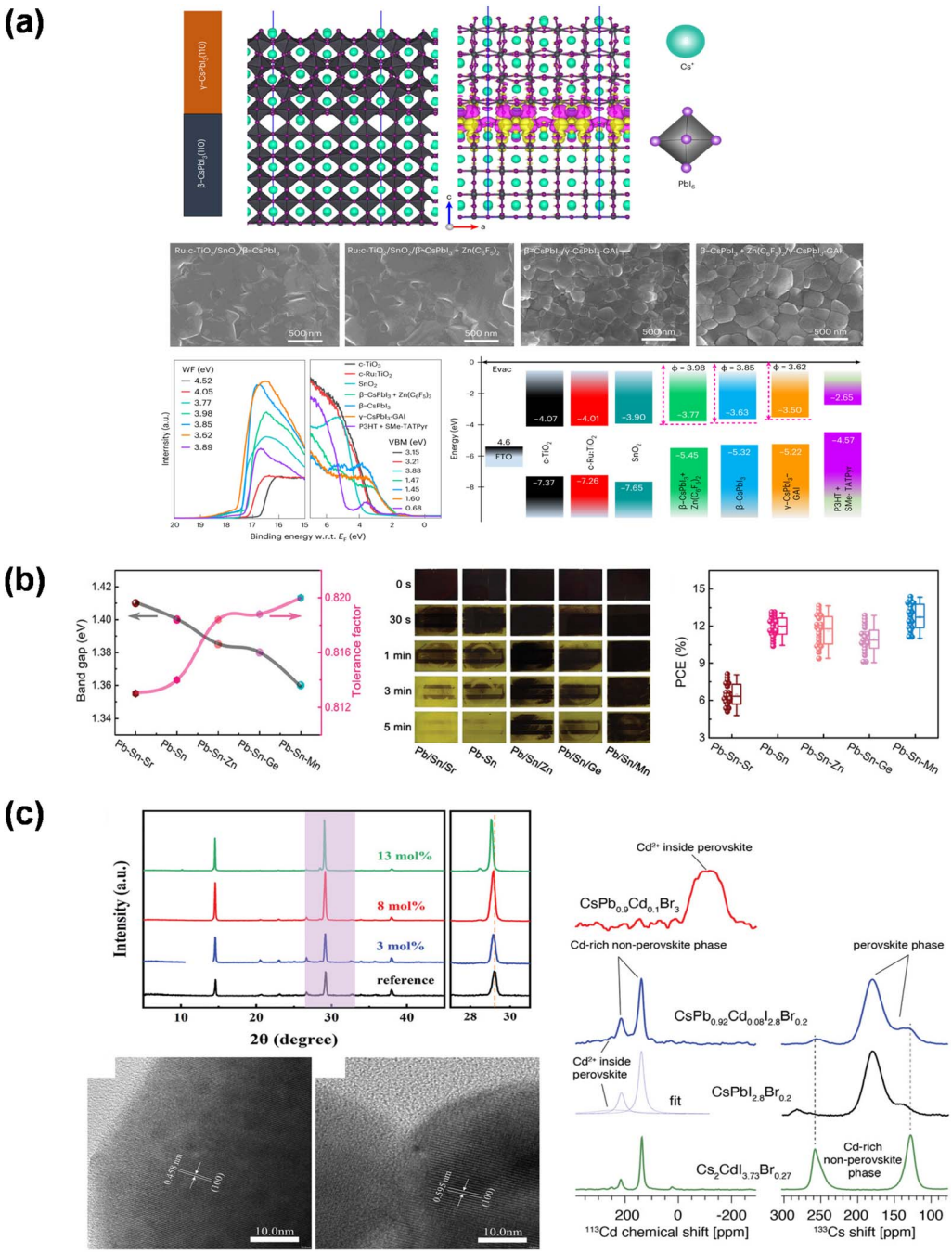

Fig. 15 The review of efficiency enhancement *via* material composition and phase engineering with (a) $Zn(C_6F_5)_2$ in $CsPbI_3$ perovskite (reproduced with permission from *Nat. Energy*, **8**, 989–1001. Copyright 2023 Springer Nature),[159] (b) Mn^{2+} in $CsPb_{1-x-y}Sn_xB_yI_{3-z}Br_z$ perovskite (reproduced with permission from *Adv. Mater.*, **36**(14), 2309193. Copyright 2023 Wiley-VCH GmbH),[149] and (c) CdI_2 in $CsPbI_{3-x}Br_x$ (reproduced with permission from *Adv. Sci.*, **9**(36), 2204486. Copyright 2022 Wiley-VCH GmbH).[150]

coordinate with the Pb^{2+} defects while simultaneously forming a H-bond with neighboring halides, effectively resulting in increased V_{OC} and FF from 1.195 V and 80.9% to 1.233 V and 81.9% and a PCE increase from 19.5% to 20.8%. Similarly, many surface passivation studies thereafter have focused on using molecules that can effectively interact with under-coordinated Pb^{2+} defects, while adding extra functionalities to the passivator for added effects. Zhang *et al.* used a trifluoroacetamide (TFA) passivator that has two amine groups for stronger chelation with the Pb^{2+} defects.[108] Moreover, the trifluoro group not only applies a strong dipole to the TFA passivator, but also gives hydrophobic passivation capabilities, greatly increasing the PCE to 21.35%. In 2023, Wang *et al.* additionally identified iodine interstitial defects as another source of solar cell performance inhibition and used 2,6-diaminopyridine (2,6-DAPy) to strongly passivate the surface defects as shown in

Table 6 Efficiency enhancement *via* reducing trap-induced recombination losses

No.	Strategy	Structure	Type	J_{SC} [mA cm^{-2}]	V_{OC} [V]	FF [%]	PCE [%]	Ref.
1	Surface defect passivation	FTO/TiO_2/$CsPbI_{3-x}Br_x$/HA/spiro-OMeTAD/Au	NIP	20.55	1.233	81.9	20.8	171
2		FTO/TiO_2/$CsPbI_{3-x}Br_x$/TFA/spiro-OMeTAD/Au	NIP	20.74	1.239	83.07	21.35	108
3		FTO/TiO_2/$CsPbI_{3-x}Br_x$/2,6-DAPy/spiro-OMeTAD/Au	NIP	20.78	1.252	83.71	21.8	106
4		FTO/TiO_2/$CsPbI_{3-x}Br_x$/BMBC/spiro-OMeTAD/Au	NIP	20.83	1.249	83.57	21.75	107
5		FTO/TiO_2/$CsPbI_3$/BTABr/spiro-OMeTAD/Au	NIP	20.81	1.2	85.4	21.31	117
6	Buried interface passivation	FTO/TiO_2/SPA/$CsPbI_3$/OAI/spiro-OMeTAD/Au	NIP	20.51	1.229	83.8	20.98	126
7		FTO/TiO_2/ATFC/$CsPbI_3$/spiro-OMeTAD/Au	NIP	20.6	1.24	82.82	21.11	123
8		ITO/NiO_x/4-ABSA/$CsPb_{0.6}Sn_{0.4}I_{3-x}Br_x$/PCBM/ZrAcac/Ag	PIN	26.5	0.83	79.1	17.4	172
9	Bulk passivation	FTO/TiO_2/$CsPbI_3$:CsFo/spiro-OMeTAD/Au	NIP	20.57	1.25	82.5	21.23	162
10		FTO/TiO_2/$CsPbI_3$:EMIMHSO$_4$/spiro-OMeTAD/Au	NIP	20.6	1.17	83	20.01	97
11		FTO/TiO_2/$CsPbI_3$:DED/spiro-OMeTAD/Au	NIP	20.6	1.244	82.52	21.15	93
12		ITO/SnO_2/$CsPbI_{2.85}Br_{0.15}$:PC/ODADI/spiro-OMeTAD/Au	NIP	20.4	1.342	80.59	22.07	94
13	Crystal growth control	FTO/TiO_2/$CsPbI_3$:RBITC/spiro-OMeTAD/Au	NIP	20.65	1.24	82.44	20.95	95
14		FTO/TiO_2/$CsPbI_3$:DMAAc/spiro-OMeTAD/Au	NIP	20.8	1.25	81.6	21.14	163
15		ITO/P3CT-N/$CsPbI_3$:$PbAc_2$/PCBM/C_{60}/BCP/Ag	PIN	20.52	1.215	80.89	20.17	167
16	Lattice stress release	FTO/TiO_2/$CsPbI_3$:GDY/spiro-OMeTAD/Au	NIP	20.49	1.191	83.96	20.49	87
17		ITO/NiO_x/$CsPbI_{2.85}Br_{0.15}$:5-MVA/PCBM/BCP/Ag	PIN	20.08	1.23	84.31	20.82	96
18		ITO/NiO_x/MeO-2PACz/$NbCl_5$/$CsPbI_3$/PCBM/BCP/Ag	PIN	20.5	1.25	83.1	21.24	130
19	Crystal growth control + bulk passivation	FTO/TiO_2/$CsPbI_3$:DMAFa/spiro-OMeTAD/Au	NIP	20.49	1.21	82.02	20.4	166
20	Buried interface passivation + lattice stress release	FTO/TiO_2/DCB/$CsPbI_3$/spiro-OMeTAD/Ag	NIP	20.71	1.26	83.8	21.86	122
21	Sn-defect regulation (crystal growth control)	ITO/PEDOT:PSS/$CsPb_{0.55}Sn_{0.45}I_2Br$:CsCl/$PbSO_4$/PCBM/BCP/Ag	PIN	20.57	0.7	71.82	10.39	173
22		FTO/PEDOT:PSS/PTAA/$CsPb_{0.4}Sn_{0.6}I_{2.4}Br_{0.6}$:MAI/$C_{60}$/BCP/Ag	PIN	22.96	0.793	78.77	13.98	169
23		ITO/PEDOT:PSS/$CsSnI_3$:CsFa/ICBA/BCP/Ag	PIN	24.94	0.75	74	13.68	161
24	Sn-defect regulation (antioxidants)	ITO/SnO_2/$CsPb_{0.7}Sn_{0.3}IBr_2$:ZnC_2O_4/spiro-OMeTAD/Au	NIP	15.5	1.18	76.7	14.1	75
25		ITO/NiO_x/$CsPb_{0.6}Sn_{0.4}I_2Br$:DCD/ZnO/PCBM/Ag	PIN	22.67	0.87	71.73	14.17	99
26		ITO/NiO_x/$CsSnI_3$:CBZ/ZnO/PCBM/Ag	PIN	21.38	0.73	71.99	11.21	81
27		ITO/NiO_x/$CsSnI_{2.6}Br_{0.4}$:DMKO/PCBM/ZrAcac/Ag	PIN	20.7	0.75	72.1	11.2	156
28		ITO/PEDOT:PSS/$CsSnI_3$:PTM/ICBA/BCP/Ag	PIN	21.81	0.64	72.1	10.1	100
29		FTO/c-TiO_2/mp-TiO_2/$CsSnI_3$:EMIMAc/Al_2O_3/NiO_x/carbon	NIP	22.1	0.56	69	8.54	92
30		ITO/PEDOT:PSS/$CsSnI_3$:TSC/C_{60}/BCP/Cu	PIN	19.7	0.63	66.1	8.2	174
31		FTO/c-TiO_2/mp-TiO_2/$CsSnI_3$:CPT/Al_2O_3/NiO_x/carbon	NIP	23.4	0.52	66	8.03	102

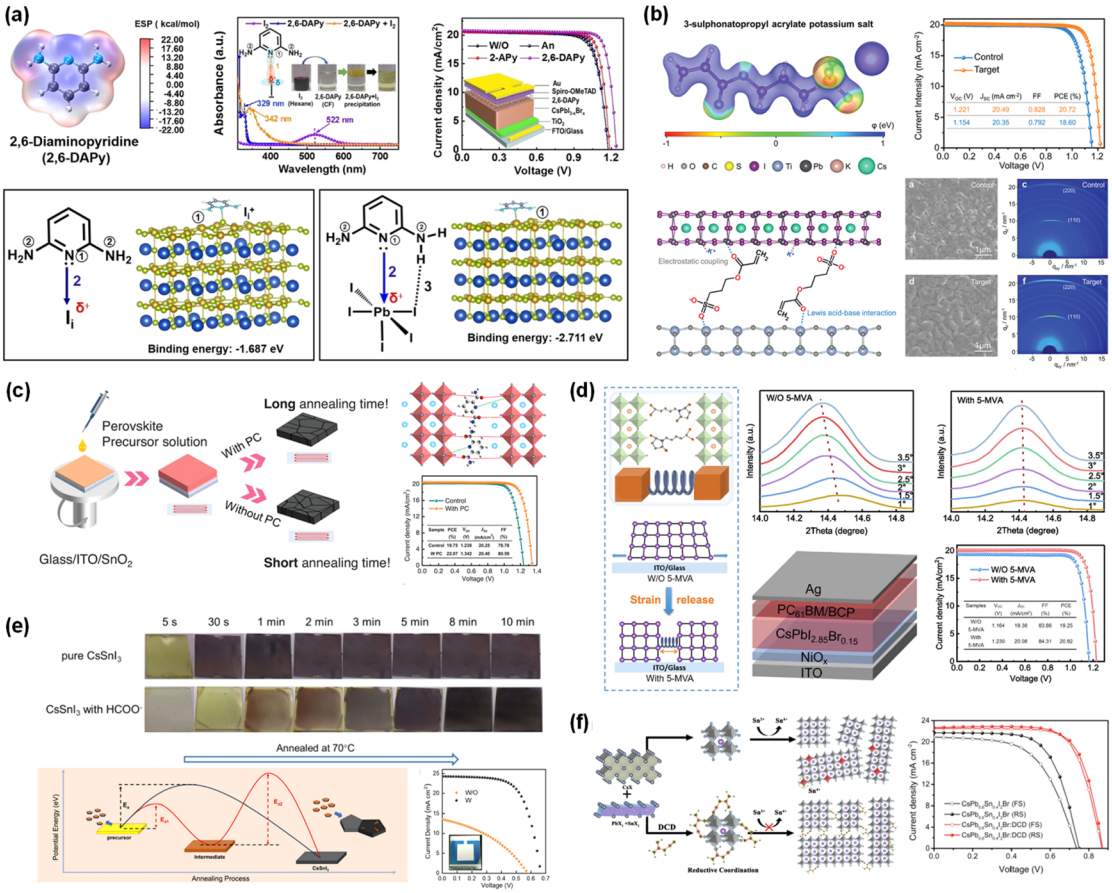

Fig. 16 The review of efficiency enhancement *via* reducing trap-induced recombination losses. (a) Perovskite surface defect passivation with 2,6-diaminopyridine (2,6-DAPy) (reproduced with permission from *Angewandte Chemie*, 2023, **62**, e202305815. Copyright 2023 Wiley-VCH GmbH).[106] (b) Buried interface defect passivation with 3-sulphonatopropyl acrylate potassium (SPA) (reproduced with permission from *Advanced Materials*, 2023, **35**, 2207172. Copyright 2022 Wiley-VCH GmbH).[126] (c) Bulk defect passivation *via* additive engineering with 2,6-pyridinedicarboxamide (PC) (reproduced with permission from *Advanced Energy Materials*, 2024, **14**, 2400151. Copyright 2024 Wiley-VCH GmbH).[94] (d) Inhibiting defect formation by releasing lattice stress with a 5-maleimidovaleric acid (5-MVA) additive (reproduced with permission from the *Journal of Energy Chemistry*, 2025, **100**, 87–93. Copyright 2024 Science Press and Dalian Institute of Chemical Physics, Chinese Academy of Sciences).[96] (e) Regulating crystal growth kinetics and transformation of the phase transition pathway with a cesium formate (CsFa) additive (reproduced with permission from *ACS Energy Letters*, 2024, **9**, 5870–5878. Copyright 2024 American Chemical Society).[161] (f) Preventing Sn^{2+} oxidation with a dicyandiamide (DCD) antioxidant additive (reproduced with permission from the *Chemical Engineering Journal*, 2023, **452**, 139697. Copyright 2022 Elsevier B.V.).[82]

Fig. 16a.[106] The authors showed that the strong nucleophilicity of the pyridine ring is more effective in passivating the positively charged defects, effectively resulting in a large increase in V_{OC} and FF from 1.189 V and 80.03% to 1.252 V and 83.71% and a significant PCE increase from 19.6% to 21.8%. Amine groups are not the only functional groups that can passivate perovskite surface defects, as shown by Zhang *et al.* in 2023.[107] Here, the authors used a cysteine derivative, namely BMBC, that possesses multiple functional groups such as –NH, –S and –C=O that can each interact with halide vacancy defects. Through the multiple passivation effect, the authors were able to confirm the effectiveness of this strategy through the enhanced V_{OC} of 1.249 V and high FF of 83.57%, yielding a high PCE of 21.75%. On the other hand, Tan *et al.* demonstrated the passivation of the perovskite surface with extra halide anions, supplied from an organic halide salt, BTABr.[117] The authors showed that the bromide ions could not only passivate the surface defects but also diffuse into the perovskite bulk film and passivate deeper defects, while most of the BTA^+ ions remain at the surface. The effectiveness of this strategy can be seen by the high efficiency of 21.31%.

The bottom interface (or the buried interface) of perovskite thin films is also a well-known hotspot for detrimental defects, and their passivation must consider interactions of the passivating agent with both the perovskite defects and the CTL defects. Typically, a proper passivating agent would consist of functional groups such as amine groups or ammonium halides, for the passivation of the perovskite layer, and acids such as carboxylates and sulfonates for the passivation of the bottom layer, which is usually a metal oxide.[122,126,170] In 2022, Xu *et al.* treated a TiO_2 ETL with 3-sulphonatopropyl acrylate potassium (SPA) prior to coating the $CsPbI_3$ inorganic perovskite layer.[126] As shown in Fig. 16b, both the sulfonate and carboxylate groups can interact with either the oxygen vacancies of the TiO_2 layer or

the halide vacancies of the perovskite layer, while the potassium cation would bind with the halides of the perovskite layer in order to inhibit formation of additional halide vacancies. Moreover, the increased hydrophilicity of the TiO_2 layer due to SPA treatment increased the perovskite crystallinity, leading to overall fewer defects, and hence an increased V_{OC} of 1.221 V, increased FF of 82.8%, and increased PCE of 20.72%. Meanwhile, Xu *et al.* treated the $TiO_2/CsPbI_3$ interface with a 4-amino-2,3,5,6-tetrafluorobenzoate cesium (ATFC) passivator, where the TiO_2 defects were passivated by the amine group of ATFC and the perovskite defects were passivated by the carboxylate group of ATFC.[123] In addition, the adjacent fluorine atoms on the benzene ring could provide additional interaction with both the TiO_2 defects and the perovskite defects, ensuring a stronger degree of passivation and a high PCE of 21.11% for the final device. Similarly, Qiu *et al.* used a dipolar passivator, named SA, for simultaneous passivation of TiO_2 and perovskite layers.[122] Compared to the commonly used carboxylate groups, the sulfonate group could form a tridentate chelation with the TiO_2 defects for stronger passivation, while the hydrogen bonds between the amine group of SA and halides of perovskite passivated the $CsPbI_3$ layer. Overall, a high PCE of 21.86% was obtained. Similar strategies can also be applied to inverted inorganic perovskite solar cell devices as well. Zhang *et al.* applied 4-aminobenzenesulfonic acid (4-ABSA) to passivate the bottom NiO_x HTL surface and the buried perovskite layer interface simultaneously, achieving a PCE of 17.4% for a $CsPb_{0.6}Sn_{0.4}I_{3-x}Br_x$ solar cell device.[170]

While the majority of defects are usually congregated at interfaces, the impact of perovskite bulk defects such as point defects and grain boundaries must also be addressed. However, despite their similarity in nature to interfacial defects, since the physical location of such defects makes it difficult to passivate them through pre- or post-treatment methods, researchers have turned to applying additives to the perovskite precursor solution itself so that harmful defects are passivated within the bulk film during and after the thin-film annealing process.[93–95,97,103,162,166,177] For example, a common approach is to use a formate additive such as a dimethylamine formate (DMAFa) or CsFa additive, since formate anions can passivate the Pb^{2+} defects that occur due to halide vacancies within the perovskite bulk film.[162,166] Similarly, in 2021, Du *et al.* introduced a low concentration of 1-ethyl-3-methylimidazolium hydrogen sulfate ($EMIMHSAO_4$) ionic liquid additive to the perovskite precursor solution.[97] The imidazolium ($EMIM^+$) cations and HSO_4^- anions were shown to passivate electrophilic defects and under-coordinated Pb^{2+} defects, respectively, within the perovskite bulk film, resulting in a high performing device with 20.01% PCE. Meanwhile, Wang *et al.* used a single molecule DED or 2,2-dithienylketone (DTK) additive with the intent to passivate bulk Pb^{2+} defects with the collaborative chelating effect of the carbonyl and thienyl groups.[93] Here, they found that the bifacial 'dione' structure of DED allowed for more efficient passivation of the perovskite bulk defects, where the optimized devices yielded a PCE of 21.15%. A notable aspect of additive engineering is that the additives more often than not fulfill multiple niches, as shown in the studies of Wang *et al.* using a 2,6-pyridinedicarboxamide (PC) additive.[94] The extra stability to the perovskite lattice offered by multiple balancing interactions between the amide groups or the *N*-pyridine group of the PC additive and the Pb^{2+} defects, otherwise noted as a "hinge modulation" by the authors, ensured that the perovskite film with PC can withstand longer annealing times in air, thus resulting in a more crystalline perovskite film as depicted in Fig. 16c. As a result, not only did the optimized device display a high V_{OC} of 1.342 V, but the resulting PCE is also among the recently highest reported for inorganic perovskite solar cells at 22.07%.

4.3.2 Inhibiting defect formation. While defect passivation has been a successful strategy to reduce recombination losses in inorganic perovskite solar cells to some extent, other strategies aim to tackle the root of the problem and rather inhibit defect formation by approaching the fundamental mechanism of defect formation. On one hand, the poor solubility of perovskite precursors may lead to uncontrolled rapid crystallization of solution processed all-inorganic perovskite films with detrimental defects such as pin-holes, grain boundaries or photo-inactive low-dimensional phases. On the other hand, the lattice mismatch between the inorganic perovskite layer and common metal oxide CTLs such as TiO_2 and SnO_2 would lead to lattice stress and the formation of related defects within the perovskite layer, which could lead to poor charge carrier dynamics and undesired performance drops.[87,96,122,130] The following section describes the recent progress in solving the above issues.

The formation process of solution processed perovskite films consists of nucleation and crystal growth, where it is generally accepted that fast homogeneous nucleation and slow crystal growth are beneficial for achieving high crystallinity.[178,179] As such, Zhang *et al.* used a sacrificial dye Rhodamine B isothiocyanate (RBITC) to facilitate nucleation while deterring crystallization in order to increase the crystallinity of the perovskite film.[95] The authors showed that photo-thermal decomposition of RBITC yields benzoic acid molecules that act as anti-solvent to promote initial nucleation, while the SCN^- anions interact with the Pb sites to deter crystal growth, eventually resulting in a highly crystalline inorganic perovskite solar cell with a high PCE of 20.95%. In another study by Zai *et al.*, DMAFa was added to the perovskite precursor, where the formate anion would interact with the exposed Pb^{2+} sites during the annealing process.[166] This interaction provided sufficient time for grain growth as the $HCOO^-$ is gradually replaced by I^-, and the final solar cell device with reduced defects exhibited increased V_{OC}, an increased FF and increased PCE at 20.40% compared to the pristine device with 18.87% PCE. Meanwhile, another risk of inorganic perovskites is the formation of undesired photo-inactive intermediate phases such as Cs_4PbI_6 that can degrade the overall photovoltaic performance, and thus it is crucial to regulate the crystallization process to prevent this. A common strategy is to incorporate the dimethylammonium (DMA^+) additive into the precursor solution, which has been reported to aid in the formation of a stable photo-active black phase of $CsPbX_3$, while inhibiting the formation of Cs_4PbX_6.[163,167] A study by Cui *et al.* well illustrates this strategy

where a dimethylamine acetate (DMAAc) molten salt additive supplies the precursor solution with extra Ac^- anions that can stabilize the $DMAPbI_3$ lattice structure, which reacts with the CsI precursors to produce a stable $CsPbI_3$ structure with volatile DMAI byproducts.[163] In particular, the authors emphasize the importance of the DMAAc additive that inhibits Cs_4PbI_6 formation, whereas without DMAAc, the reaction of $DMAPbI_3$ with CsI could produce Cs_4PbI_6. The optimized $CsPbI_3$ solar cell device shows a high PCE of 21.14%. Meanwhile, Sun *et al.* employed dimethylammonium iodide (DMAI) and lead acetate ($PbAc_2$) to substitute the original PbI_2 precursor.[167] The authors showed that the addition of DMAI increases the solubility of CsI within the precursor solution, after which the $PbAc_2$ introduces Ac^- ligands to the nuclei and slows down crystal growth as the anion is slowly exchanged with the iodide ion from DMAI. The formation of Cs_4PbI_6 is also shown to be inhibited in the optimized solar cell device, which showed a PCE of 20.17%.

Another inherent source of defects and trap-induced recombination loss in all-inorganic perovskite solar cells is the presence of lattice stress, which could potentially cause the formation of harmful defects within the perovskite layer. On one hand, the ion size mismatch of inorganic perovskites may lead to intrinsic tensile strain throughout the bulk perovskite film.[87,96,180] In 2024, Zhang *et al.* introduced graphdiyne (GDY), an sp-hybridized carbon framework, to be incorporated within the $CsPbI_3$ bulk film.[87] The authors found that GDY not only delays the crystal growth process for the formation of a highly crystalline perovskite film, but it also helps release lattice stress within the bulk film during the annealing process, as noted in depth-dependent crystallographic analysis. The optimized device showed impressive V_{OC} and FF values at 1.191 V and 83.96%, respectively, and a high PCE of 20.49%. Very recently, Sun *et al.* also noted the significance of releasing internal perovskite lattice stress and added a flexible molecule, 5-maleimidovaleric acid (5-MVA), as an additive within the inorganic perovskite precursor solution.[96] It was shown that, since both functional groups at either end of the 5-MVA molecule are effective electron donors, they could strongly interact with Pb^{2+} defect sites within the $CsPbI_{2.85}Br_{0.15}$ perovskite lattice and act as physical buffers to release tensile strain of the perovskite film, as seen in Fig. 16d. Its immediate effectiveness was shown by the depth-dependent analysis and the greatly improved photovoltaic characteristics resulting in a high PCE of 20.82%. On the other hand, the lattice mismatch and discrepancies in thermal expansion coefficients between the perovskite lattice and substrates such as metal oxides can cause greater lattice distortion at the substrate/perovskite interface, thus also harming the interfacial contact.[122,130] In the studies by Qiu *et al.*, a flexible SA molecule based on a propyl chain that was treated on the TiO_2 surface helped release the lattice stress at the TiO_2/$CsPbI_3$ interface.[122] The inverted p–i–n structured devices adopt a similar strategy through the widely accepted SAM treatment on the NiO_x substrate. Xu *et al.* realized that a poor SAM monolayer coverage on the NiO_x substrate could cause unnecessary lattice distortions at the perovskite buried interface and treated the SAM layer with niobium pentachloride (NCL) to prevent SAM agglomeration and improve its morphology.[130] As a result, the authors observed a decrease in interfacial lattice stress that also led to an increase in optimized solar cell PCE to 21.24%, which is among the highest PCEs reported to date for inverted inorganic perovskite solar cells.

4.3.3 Pb–Sn and Sn-based inorganic perovskite solar cells. When considering the partial or total substitution of Pb with Sn in inorganic perovskite solar cells, more tailored strategies are required. First of all, the precursors for Sn-based perovskite materials exhibit weaker solubility compared to their Pb-based counterparts, making it even more difficult to fabricate highly crystalline, defect-free perovskite thin films. Moreover, it is well-known that Sn-based perovskites experience a high tendency of the Sn^{2+} to be oxidized into its more stable oxidation state of Sn^{4+}, not only creating photo-inactive non-perovskite phases within the device, but also heavily doping the perovskite layer with detrimental p-type deep-level defects.

The problem of rapid crystallization could be resolved by adapting similar strategies to regulating crystallization kinetics of Pb-based inorganic perovskite thin films discussed in the previous section.[75,81,82,152,161,169,173] For example, Chen *et al.* first demonstrated the poor crystallinity of a pristine $CsPb_{0.55}Sn_{0.45}I_2Br$ perovskite film and then showcased a $CsPb_{0.55}Sn_{0.45}I_2Br$–CsCl perovskite film with much improved crystallinity and large, micro-sized grains.[173] It was shown that the CsCl additive provided small halogen ions that could simply infiltrate the bulk film at the grain boundaries during fabrication and strongly bond with the Sn^{2+}, effectively reconfiguring the grain boundaries and inhibiting the formation of halide vacancies. With the addition of a hydrophobic $PbSO_4$ passivation barrier at the perovskite surface, the optimized device displayed an impressive PCE of 10.39% with a highly improved V_{OC} and FF of 0.70 V and 71.82%, respectively. As such, due to the lower solubility and faster ion release of the Sn-based precursors compared to the Pb-based precursors, it is important to alleviate this discrepancy in order to form a homogeneously distributed perovskite film. Shang *et al.* did a good job in demonstrating this idea as they partially substituted PbI_2 with $PbAc_2$ in the perovskite precursor solution.[169] As shown in this work, the release rate of Sn^{2+} within the precursor solution is matched by the release of Pb^{2+} by $PbAc_2$, while an additional MAI additive supplies extra iodide anions for the fabrication of a homogeneous phase-pure Pb–Sn perovskite solar cell with a high PCE of 13.98%. Recently, Yu *et al.* fabricated $CsSnI_3$ perovskite solar cells with a CsFa additive in order to control the crystallization kinetics, yielding a high certified PCE of 13.68%, which is one of the highest reported efficiencies for $CsSnI_3$ devices to date.[161] Here, the authors proposed that the introduction of a pseudo-halide anion that could strongly bond with the Sn^{2+} cations could dramatically slow down crystallization by transforming the phase transition path as shown in Fig. 16e.

Meanwhile, the oxidation of Sn^{2+} to Sn^{4+} provided new challenges to the Sn-based inorganic perovskite solar cell community. To address this challenge, many studies have actively sought antioxidants or reducing agents in order to inhibit or reduce the Sn^{2+} oxidation.[81,92,99,100,102,156,173,174] For example, some cases report the effectiveness of Zn-based additives to prevent Sn^{2+} oxidation based on the more

suitable reduction potential of Zn^{2+} compared to Sn^{2+}.[173] For example, zinc oxalate additives within the $CsPb_{0.7}Sn_{0.3}PbIBr_2$ perovskite precursor solution would not only reduce any present Sn^{4+} to Sn^{2+}, but also the oxalate anions could strongly interact with the metal ions to regulate crystal growth. The resulting Pb–Sn-based solar cell device showed a champion PCE of 14.1%. However, such strategies would also have to consider the possible incorporation of Zn^{2+} within the inorganic perovskite lattice, which could alter the intrinsic properties of the perovskite thin film. A study by Wen *et al.* in 2023 used a dicyandiamide (DCD) additive to prevent oxidation of Sn^{2+}.[99] The authors noted that the presence of –C≡N and –C═NH functional groups would provide a strong interaction with the Sn^{2+} ions within the perovskite film, actively preventing oxidization and reducing deep level defects, for a high PCE of 14.17% in the optimized solar cell device as shown in Fig. 16f. Similarly, many researchers have incorporated antioxidative additives such as carbazide (CBZ),[81] dimethyl ketoxime (DMKO),[156] phthalimide (PTM),[100] 1-ethyl-3-methylimidazolium acetate (EMIMAc),[92] thiosemicarbazide (TSC),[174] and 1-(4-carboxyphenyl)-2-thiourea (CPT)[102] within $CsSnI_3$-based precursor solutions and have shown promising results.

4.4 Modifying interface charge carrier dynamics

As mentioned in the previous section, understanding the role of interfaces in inorganic perovskite solar cells is crucial to achieving high efficiency. Not only are the majority of defects found at interfaces, but poor interfacial contacts may also lead to poor charge carrier transfer efficiency, charge carrier accumulation, defect-induced degradation, lattice stress, ion migration and so on.[176] Therefore, proper strategic designs at perovskite/CTL interfaces such as modifying energy levels, inserting blocking layers, and inserting dipole-layers would be able to facilitate efficient charge carrier separation, reduce back recombination and prevent charge carrier accumulation.[114,138] Furthermore, another promising strategy involves the formation of heterojunctions that can effectively enhance charge carrier extraction.[136,181] This section will focus on interfacial strategies beyond the scope of, but not excluding, interfacial defect reduction (Table 7).

4.4.1 Surface/interface modification. Some of the most common studies of interface modification are motivated by the energy level mismatch between the inorganic perovskite layer and the adjacent CTLs, thus aiming to use passivating molecules that can also shift the energy level at the perovskite interface.[119,120,181–183] For example, Heo *et al.* demonstrated a p–i–n structured $CsPbI_3$ solar cell and treated the perovskite surface with a solution of OMXene.[120] OMXene treatment not only enabled a strong electric field at the perovskite/ETL interface, but also its n-type characteristics provided an extra energy level for better alignment at the interface, enabling efficient charge extraction and thus a high PCE of 19.69%. Wang *et al.* also noticed that the $CsPbI_3$/PCBM interface was not ideal for efficient electron transfer for an inverted device and thus applied propylamine hydrochloride (PACl) to modify the perovskite surface.[183] It was shown that PACl could effectively change the p-type nature of the inorganic perovskite surface to a slight n-type nature, which would prove beneficial for electron transfer to the subsequent PCBM ETL, yielding an optimized device PCE of 20.17% and an impressive V_{OC} and FF of 1.15 V and 84%, as depicted in Fig. 17a. Furthermore, Guo *et al.* also induced a p- to n-type transition at the $CsPbI_3$ surface by creating a $CsPbI_3$/PbS heterojunction through the reaction of perovskite with *N*,*N*′-diphenylthiourea (DPhTA).[181] The resulting device also exhibited superior charge extraction and thus a much improved PCE from 13.36% to 20.18%.

Other studies of interface modification have focused on treating the interface with molecules that exhibit strong dipoles such as when a dipole monolayer is formed, which could either facilitate charge extraction or hinder charge back-

Table 7 Efficiency enhancement *via* modifying interface charge carrier dynamics

No.	Strategy	Structure	Type	J_{SC} [mA cm^{-2}]	V_{OC} [V]	FF [%]	PCE [%]	Ref.
1	Energy level alignment	FTO/NiO_x/MeO-2PACz/$CsPbI_{3-x}Br_x$/MPTS/PCBM/BCP/Ag	PIN	20.4	1.22	84.2	21	119
2		FTO/TiO_2/$CsPbI_3$:MACl/PEACl/spiro-OMeTAD/Ag	NIP	20.7	1.2	83.1	20.6	182
3		ITO/PTAA/$CsPbI_3$/OMXene/CPTA/BCP/Ag	PIN	19.9	1.21	82	19.7	120
4		FTO/P3CT/$CsPbI_3$/PACl/PCBM/BCP/Ag	NIP	21.36	1.13	84	20.17	183
5		ITO/P3CT-N/$CsPbI_3$/DPhTA/PCBM/C_{60}/TPBi/Ag	PIN	20.84	1.18	81.9	20.18	181
6	Dipole interlayer	FTO/TiO_2/DCB/$CsPbI_3$/spiro-OMeTAD/Ag	NIP	20.7	1.26	83.8	21.9	122
7		FTO/TiO_2/$CsPbI_3$/F_3EAI/spiro-OMeTAD/Au	NIP	20.6	1.2	82.9	20.5	114
8		FTO/TiO_2/m-Al_2O_3/$CsPbI_3$/CF_3-PAI/carbon	NIP	20.5	1.14	78.2	18.3	136
9		FTO/c-TiO_2/$CsPbI_{2.75}Br_{0.25}$/NPA 2D-RP/P3HT/Ag	NIP	20.6	1.15	83.5	19.8	135
10		FTO/TiO_2/4A1N/$CsPbI_3$/spiro-OMeTAD/Ag	NIP	20.9	1.2	80	20	138
11		ITO/PEDOT:PSS/$CsPb_{0.5}Sn_{0.5}I_2Br$/F-TBA/PCBM/BCP/Ag	PIN	23.12	0.83	73	14.01	112
12	Heterojunctions	FTO/TiO_2/$CsPbI_3$/BDABr/spiro-OMeTAD/Au	NIP	20.8	1.18	83.6	20.6	142
13	(3D/low-D)	ITO/PTAA/$CsPbI_3$/Cs_4PbBr_6/CPTA/BCP/Ag	PIN	20.2	1.23	84.8	21	134
14	Heterojunctions	FTO/TiO_2/$CsPbI_2Br$/$CsPbI_{3-x}Br_x$/PTAA/Au	NIP	18.1	1.15	80.9	16.8	168
15	(compositional)	ITO/SnO_2/$CsPbI_{3-x}Br_x$/CsF/spiro-OMeTAD/Au	NIP	19.4	1.27	85.3	21	116
16	Heterojunctions	ITO/MeO-2PACz/β-$CsPbI_3$/γ-$CsPbI_3$/PCBM/BCP/Ag	PIN	20.6	1.16	84.2	20.2	154
17	(beta/gamma)	FTO/TiO_2/SnO_2/β-$CsPbI_3$:$Zn(C_6F_5)_2$/ γ-$CsPbI_3$:GAI/P3HT + SMeTAPyr/Au	NIP	21.7	1.22	81.5	21.6	159

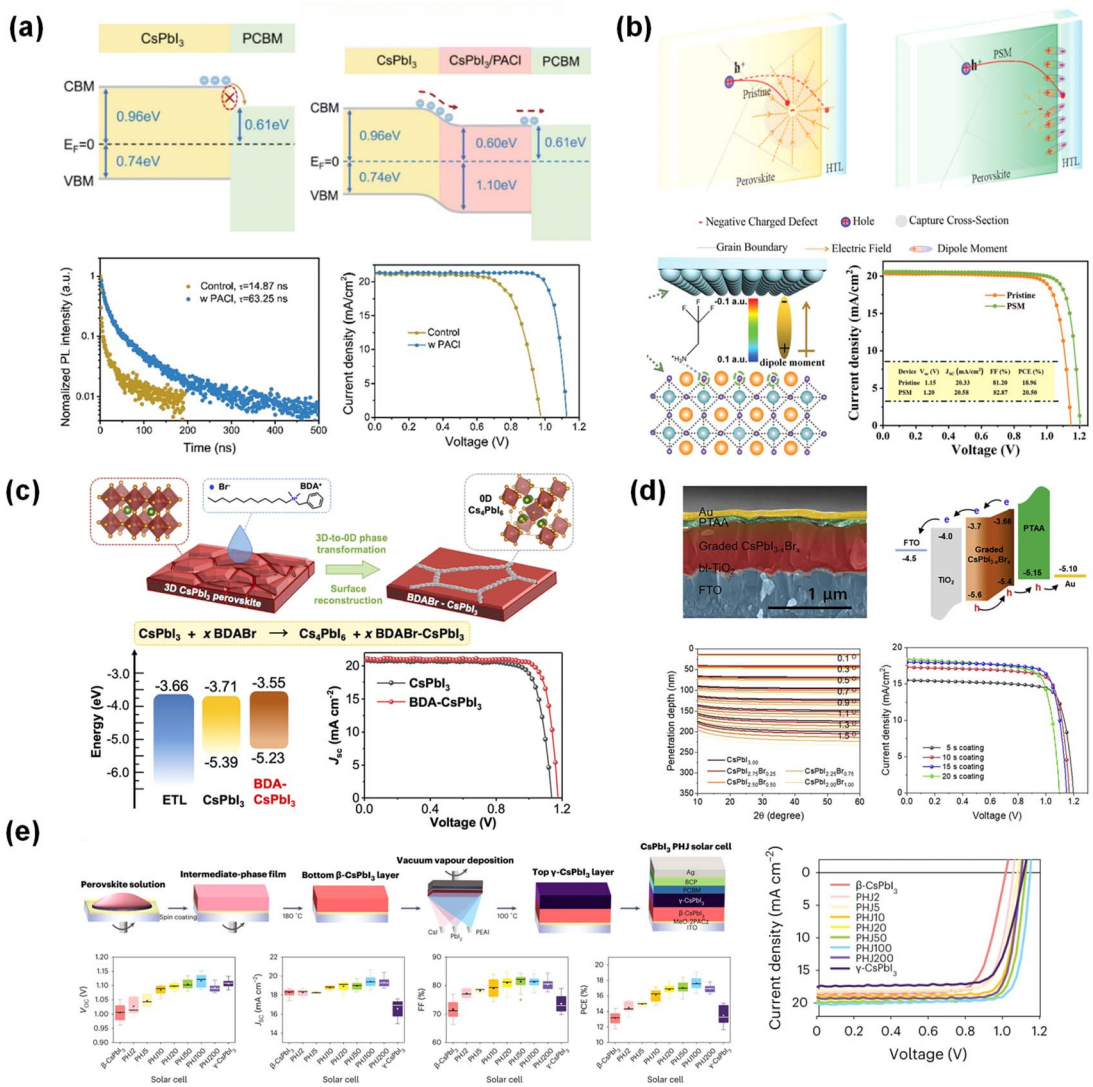

Fig. 17 The review of efficiency enhancement *via* modifying interface charge carrier dynamics. (a) Improving energy level alignment at the perovskite/ETL interface *via* a p- to n-type transition at the perovskite surface with propylamine hydrochloride (PACl) treatment (reproduced with permission from *Energy & Environmental Science*, 2023, **16**, 2572–2578. Copyright The Royal Society of Chemistry 2023).[183] (b) Improving hole transfer at the perovskite/HTL interface *via* introducing a dipole layer with highly polar 2,2,2-trifluoroethylammonium iodide (F_3EAI) treatment at the perovskite surface (reproduced with permission from *Advanced Materials*, 2022, **34**, 2202735. Copyright 2022 Wiley-VCH GmbH).[114] (c–e) Improved charge transfer induced by internal p–n heterojunctions at the inorganic perovskite layer. (c) 3D-$CsPbI_3$/0D-Cs_4PbI_6 heterojunctions *via* surface reconstruction with benzyldodecyl-dimethylammonium bromide (BDABr) treatment at the perovskite surface (reproduced with permission from *Science Bulletin*, 2023, **68**, 706–712. Copyright 2023 Science China Press).[142] (d) Composition graded $CsPbI_{3-x}Br_x$ heterojunction *via* spray deposition of $CsPbI_3$ on top of a $CsPbI_2Br$ layer (reproduced with permission from *Joule*, 2021, **5**, 481–494. Copyright 2020 Elsevier Inc.).[168] (e) Phase heterojunction formed by a two-step process of spin coating β-$CsPbI_3$ followed by vacuum evaporation of γ-$CsPbI_3$ (reproduced with permission from *Nature Energy*, 2022, **7**, 1170–1179. Copyright R. Ji, Y. Vaynzof *et al.* 2022).[184]

recombination.[112,114,122,135,136,138] Zhang *et al.* treated the $CsPbI_3$ perovskite surface with highly polar 2,2,2-trifluoroethylammonium iodide (F_3EAI) molecules, which they expected to provide a favorable path for hole extraction at the perovskite/HTL interface and yield a high PCE of 20.50%, as described in Fig. 17b.[114] It was shown that polar passivators would orient the positive dipole towards the perovskite surface, effectively attracting and passivating negatively charged defects that would otherwise trap holes and hinder extraction. Zhang *et al.* also treated the $CsPbI_3$/carbon–electrode interface with 4-trifluoromethyl-phenylammonium iodide (CF_3-PAI), which would align itself so that the positive dipole of the CF_3 group interacts with the perovskite surface.[136] Here, the authors showed that, while a direct contact between the perovskite and the carbon electrode layers would lead to back recombination since electrons could also cross the interface, the presence of the dipole layer would then deter electron transfer and ensure that only holes could selectively cross the interface. Meanwhile, some studies have demonstrated that dipole layer treatment at the buried interface could also be a viable strategy. In 2023,

Wang *et al.* used polar molecules of 4-amino-1-naphthalene sulfonate (4A1N) to functionalize the TiO_2 substrate and subsequently interact with the $CsPbI_3$ perovskite layer *via* the amino group.[138] The resulting ion–dipole interaction yielded a large shunt resistance across the interface, even under low light conditions, thus preventing back-recombination across the interface and enabling a high PCE of 20.03% and a high indoor photovoltaic PCE of 41.21% with an output power of 137.66 μW cm^{-2}.

4.4.2 Internal graded heterojunctions. One well-known advantage of organic–inorganic perovskites as photovoltaic materials is that the simple material tunability allows for flexibility in controlling the energy levels of the material. In addition to this, another advantage of all-inorganic perovskites is that their photovoltaic characteristics can also be tuned *via* controlling their many photo-active phases. These characteristics especially hold significance when they can be manipulated to offer many creative design choices for efficient inorganic perovskite solar cell structures, such as creating internal p–n heterojunctions for enhanced charge carrier separation.[116,134,142,159,168,184]

In 2023, Chen *et al.* treated a $CsPbI_3$ perovskite film with a benzyldodecyl-dimethylammonium bromide (BDABr) salt to demonstrate a surface reconstruction process where *in situ* 3-dimension-to-0-dimension phase transformation was observed.[142] While the 0D Cs_4PbI_6 phase is generally detrimental to the perovskite film due to its photo-inactivity, in this case, the 0D phase would actually accumulate on the grain boundaries to passivate pre-existing defects and also slightly shift the surface energy level such that the abundant 3D/0D heterojunctions at the surface instead aided in efficient hole transfer, as shown in Fig. 17c. Due to the reduced defects and increased charge transfer, the optimized device showed a high PCE of 20.63%. A similar concept was later demonstrated by Heo *et al.* where 0D Cs_4PbBr_6 perovskite NCs were synthesized and spray-deposited on the surface of $CsPbI_3$ films.[134] The authors showed that the 3D/0D heterojunctions could effectively reduce lattice strain, while also providing an electron-selective junction for efficient electron extraction, and the resulting p–i–n solar cell devices yielded a high PCE of 18.78%.

Besides dimension-engineered heterojunctions, the formation of heterojunctions *via* compositional control was also studied. Heo *et al.* suggested a creative approach towards creating composition-graded heterojunctions, where a thin film of $CsPbI_2Br$ was first spray-deposited on a TiO_2 substrate, followed by additional spray-deposition of $CsPbI_3$ in order to create a $CsPbI_{3-x}Br_x$ film with an internal graded heterojunction where the halide ratios (and the effective energy levels) changed with depth, as shown in Fig. 17d.[168] The fully spray-coated process not only provided an ideal band structure alignment for efficient charge extraction through an enlarged depletion region, where the unit cell device exhibited the best PCE of 16.81%, but also allowed for the realization of a stable process for efficient fully scalable inorganic perovskite

Table 8 Efficiency enhancement *via* multi-junction inorganic perovskite solar cells

No.	Strategy (narrow/wide)	Perovskite top cell	Type	Perovskite unit cell J_{SC} [mA cm^{-2}]	V_{OC} [V]	FF [%]	PCE [%]	Tandem cell PCE [%]	Ref.
1	Si/Perovskite tandem (2T)	ITO/NiO_x/$CsPbI_{2.85}Br_{0.15}$/ABA/PCBM/BCP/Ag	PIN	19.92	1.222	83.67	20.38	25.31	185
2		ITO/SnO_2/$CsPbI_{3-x}Br_x$/NiI_2/spiro-OMeTAD/Au	NIP	17.88	1.36	80.54	19.53	22.95	105
3		ITO/SnO_2/$CsPbI_{2.85}Br_{0.15}$:PC/ODADI/spiro-OMeTAD/Au	NIP	20.40	1.342	80.59	22.07	27.27	94
4		ITO/NiO_x/P3CT-N/$CsPbI_{2.85}Br_{0.15}$:ABF/PCBM/BCP/Ag	PIN	19.62	1.247	84.97	20.80	26.26	187
5	CIGS/Perovskite tandem (4T)	FTO/P3CT/$CsPbI_3$/PCBM/BCP/Ag	PIN	18.88	1.10	84.09	17.46	24.75	186
6	OPV/Perovskite tandem (2T)	ITO/NiO_x/CbzNaph/$CsPb(I_xBr_{(1-x)})_3$:(AQS:FPEA)/C_{60}/BCP/Ag	PIN	18.07	1.29	79.74	18.59	23.24	89

No.	Strategy (narrow/wide)	Top cell (wide E_g) / Bottom cell (narrow E_g)	Type	Top unit cell / Bottom unit cell (filtered by the top cell) / Bottom unit cell (unfiltered) J_{SC} [mA cm^{-2}]	V_{OC} [V]	FF [%]	PCE [%]	Tandem cell PCE [%]	Ref.
7	Perovskite/perovskite tandem (4T)	ITO/NiO_x/$CsPbI_2Br$/$Ti_{0.9}Sn_{0.1}O_2$/IZO/MgF_2	PIN	15.29	1.25	79.27	15.14	19.61	99
				7.43	0.85	70.74	4.47		
		ITO/NiO_x/$CsPb_{0.6}Sn_{0.4}I_2Br$:DCD/ZnO/PCBM/Ag		**22.67**	**0.87**	**71.73**	**14.17**		
8		ITO/SnO_2/$CsPbI_{1.5}Br_{1.5}$/spiro-OMeTAD/MoO_x/ITO	NIP	11.67	1.29	74.8	11.26	18.07	170
				11.61	0.85	72.5	7.15		
		ITO/PEDOT:PSS/$CsPb_{0.5}Sn_{0.5}I_{2.7}Br_{0.3}$/PCBM/BCP/Ag		**22.11**	**0.86**	**72.7**	**13.82**		

photovoltaic devices. In 2023, Chu *et al.* reported another method of achieving composition-graded heterojunctions for $CsPbI_xBr_{3-x}$ solar cells with a high PCE of 21.02% and high V_{OC} of 1.27 V.[116] Here, the authors showed that CsF salt treatment on $CsPbI_xBr_{3-x}$ films, followed by annealing, could trigger a solid-state reaction between the perovskite surface and CsF salt, proven by the wider bandgap measured at the surface. Through optimized parameters, the authors reported a high PCE of 21.02%.

A unique merit of $CsPbI_3$ inorganic perovskites is that the perovskite material can exhibit multiple photo-active "black" phases, which can be aligned with each other for efficient charge carrier extraction. In 2022, Ji *et al.* reported PHJ solar cells by creating a γ-$CsPbI_3$/β-$CsPbI_3$ PHJ.[184] The PHJ was fabricated through a two-step process, where the β-$CsPbI_3$ layer was first solution-processed through a spin deposition procedure with a DMAI additive and then the subsequent γ-$CsPbI_3$ layer was vacuum evaporated for deposition on the β-$CsPbI_3$ layer, as seen in Fig. 17e. Through careful optimization of the thickness of each perovskite layer, the authors achieved a high PCE of 19.1%. Mali *et al.* also demonstrated γ-$CsPbI_3$/β-$CsPbI_3$ PHJ solar cells in 2023 and increased the device PCE to an impressive 21.59%.[159] In order to further stabilize both layers and optimize energy level alignment, the authors incorporated a bis(pentafluorophenyl)zinc ($Zn(C_6F_5)_2$) p-type additive within the bottom β-$CsPbI_3$ layer, while also co-evaporating a small amount of guanidinium iodide (GAI) alongside the other precursors for the fabrication of a GAI-incorporated γ-$CsPbI_3$ layer.

4.5 Multi-junction inorganic perovskite solar cells

Despite the recent success in achieving high efficiency inorganic perovskite solar cells, the above studies mentioned so far are inevitably limited by the SQ-limit for single-junction photovoltaic devices. Thus, it is desirable to expand the focus towards multi-junction tandem cells that can surpass the efficiency limit of single junction cells. Perovskite solar cells have received peculiar interest in this field due to their simple bandgap tunability, through which they could form reliable tandem structures with silicon, CIGS, organic photovoltaic devices and other perovskite materials (Table 8).[89,94,99,105,170,185–187]

For example, Wang *et al.* demonstrated 2-terminal (2T) silicon/perovskite (Si/P) tandem cells, where they used a $CsPbI_{2.85}Br_{0.15}$ perovskite with a bandgap of 1.71 eV, which is considered ideal for the Si/P architecture, as shown in Fig. 18a.[185] Here, the wide-bandgap inorganic perovskite was processed as the top cell in conjunction with the narrow-bandgap silicon bottom cell, and the resulting tandem device exhibited a high PCE of 25.31%. The same group further

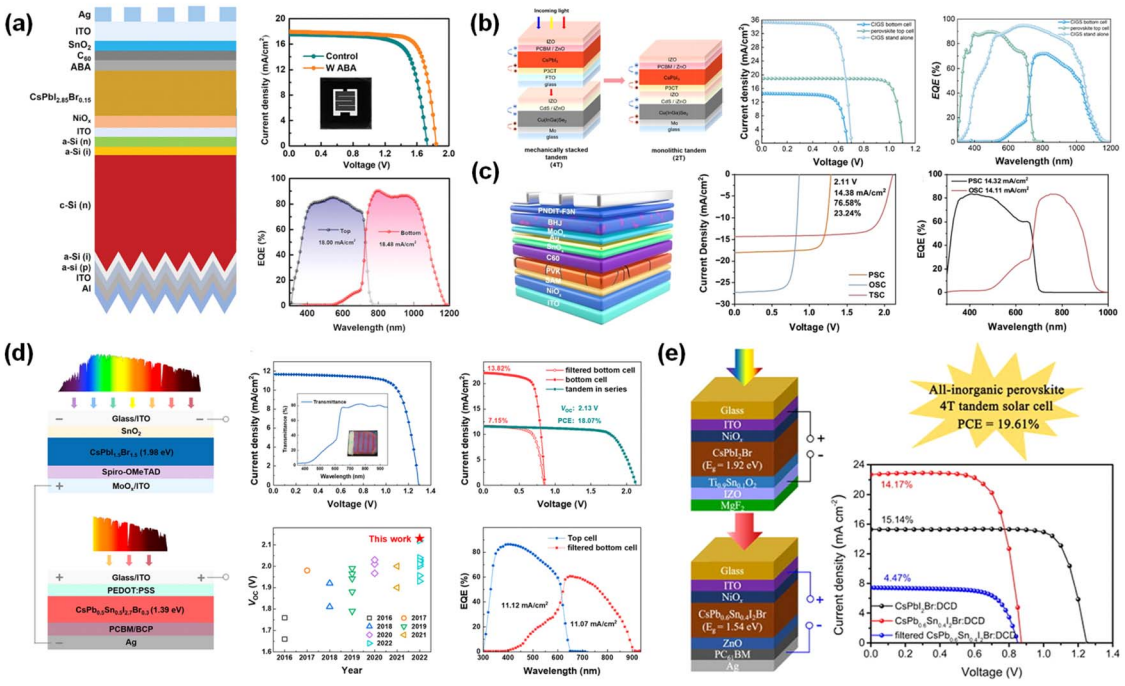

Fig. 18 The review of efficiency enhancement *via* multi-junction inorganic perovskite solar cells. (a) Silicon/$CsPbI_{2.85}Br_{0.15}$ 2T tandem solar cell and its performance (reproduced with permission from *Advanced Materials*, 2023, **35**, 2300581. Copyright 2023 Wiley-VCH GmbH).[185] (b) CIGS/$CsPbI_3$ 4T tandem solar cell and its performance (reproduced with permission from the *Journal of Energy Chemistry*, 2024, **97**, 622–629. Copyright 2024 Science Press and Dalian Institute of Chemical Physics, Chinese Academy of Sciences).[186] (c) Organic/$CsPbI_{1.8}Br_{1.2}$ 2T tandem solar cell and its performance (reproduced with permission from *Angewandte Chemie*, 2024, **63**, e202412515. Copyright 2024 Y. Li, J. Yin, S. Wu, A. K.-Y. Jen *et al.*).[89] (d) $CsPb_{0.5}Sn_{0.5}I_{2.7}Br_{0.3}$/$CsPbI_{1.5}Br_{1.5}$ 4T all-inorganic perovskite-only tandem solar cell and its performance (reproduced with permission from *ACS Energy Letters*, 2022, **7**, 4215–4223. Copyright 2022 American Chemical Society).[170] (e) $CsPb_{0.6}Sn_{0.4}I_2Br$/$CsPbI_2Br$ 4T all-inorganic perovskite-only tandem solar cell and its performance (reproduced with permission from the *Chemical Engineering Journal*, 2023, **452**, 139697. Copyright 2022 Elsevier B.V.).[99]

improved their design by etching away the defect-rich surface layer of the inorganic perovskite film by spin dripping with 3-amino-5-bromopyridine-2-formamide (ABF) in methanol solution, which, in tandem with the bottom silicon layer, now showed a higher PCE of 26.26%.[187] Soon afterwards, by regulating crystallization of the inorganic perovskite layer, the same group could suppress more defects within the perovskite film, which was again applied to a Si/P tandem device with a high PCE of 27.27% and an impressive V_{OC} of 2.024 V.[94] Recently, Zhang *et al.* used $CsPbI_3$ as the top cell and Cu(In,Ga)Se_2 (CIGS) as the bottom cell and reported fabricating 4-terminal (4T) CIGS/Perovskite (CIGS/P) tandem cells, which is shown in Fig. 18b.[186] This was the first report on 4T CIGS/P tandem cells, and the authors reported a total PCE of 24.75%. Meanwhile, Li *et al.* fabricated 2T Organic/Perovskite (O/P) tandem cells in 2024, where they used the $CsPbI_{1.8}Br_{1.2}$ inorganic perovskite with a bandgap of 1.78 eV.[89] The authors used a 9,10-anthraquinone-2-sulfonic acid (AQS) additive to suppress voltage loss within the perovskite cell by regulating the crystallization process with the sulfonic group and reported a PCE of 23.24% for the O/P tandem cell, as shown in Fig. 18c.

In 2022, Sun *et al.* demonstrated an all-perovskite 4T tandem structure (P/P) based only on inorganic Pb-based and Pb–Sn-based perovskites for the first time, where they used a wide-bandgap (1.98 eV) $CsPbI_{1.5}Br_{1.5}$ perovskite for the top cell and a narrow-bandgap (1.39 eV) $CsPb_{0.5}Sn_{0.5}I_{2.7}Br_{0.3}$ perovskite for the bottom cell.[170] As shown in Fig. 18d, the bottom Pb–Sn perovskite cell exhibited a PCE of 7.15% from the light filtered by the top cell, and the 4T P/P tandem structure yielded a total PCE of 18.07%. Soon after, in 2023, Wen *et al.* also reported a 4T P/P tandem structure using all-inorganic perovskites only.[99] Here, $CsPbI_2Br$ was chosen as the top wide-bandgap cell (1.92 eV), and by optimizing the Pb–Sn ratio, the authors found that $CsPb_{0.6}Sn_{0.4}I_2Br$ with a bandgap of 1.54 eV resulted in the highest performing bottom narrow-bandgap cell, as shown in Fig. 18e. The total PCE of the optimized 4T all-inorganic P/P tandem device was reported at 19.61%, where the PCE of the top cell was 15.14% and the PCE of the filtered bottom cell was 4.47%.

5. Conclusion & outlook

Inorganic halide perovskites, particularly those based on Pb, Sn, and Pb–Sn compositions, have gained considerable attention due to their outstanding thermal stability and suitable bandgap for single-junction and multi-junction tandem solar cells. Despite these advantages, several challenges remain to be addressed, notably phase instability, defect-induced non-radiative recombination, susceptibility to Sn^{2+} oxidation, and degraded long-term stability under operational conditions.

Recent research efforts have demonstrated progress in enhancing the stability and efficiency of inorganic perovskite solar cells through various strategies, including compositional engineering, additive incorporation, surface post-treatment, and interface optimization. Compositional engineering strategies effectively mitigate lattice strain and enhance thermodynamic stability by introducing foreign ions into perovskite structures. Additive engineering, employing multifunctional molecules, has proven successful in modulating crystallization kinetics, suppressing Sn^{2+} oxidation, and passivating defects. Surface post-treatment, achieved using multifunctional organic molecules and ionic salts, effectively suppresses surface defects and enhances perovskite lattice stability and energy-level alignment through surface reconstruction. Additionally, environmental protection layers formed through post-treatment prevent moisture ingress, thereby preserving perovskite phase stability under challenging environmental conditions. Interfacial optimization at the ETL and HTL interfaces and low-dimension heterostructure interfaces significantly reduce interfacial defects, alleviate lattice strain, improve energy-level alignment, enhance charge carrier dynamics, and suppress detrimental ion migration, thereby enhancing overall device stability and efficiency (Fig. 19a and b).

Furthermore, inorganic perovskites, owing to their suitable bandgap for tandem solar cells and thermal stability, have shown great promise as top and bottom cells in multi-junction tandem solar cells. Recent studies demonstrate their successful integration into 2T and 4T tandem configurations with silicon,

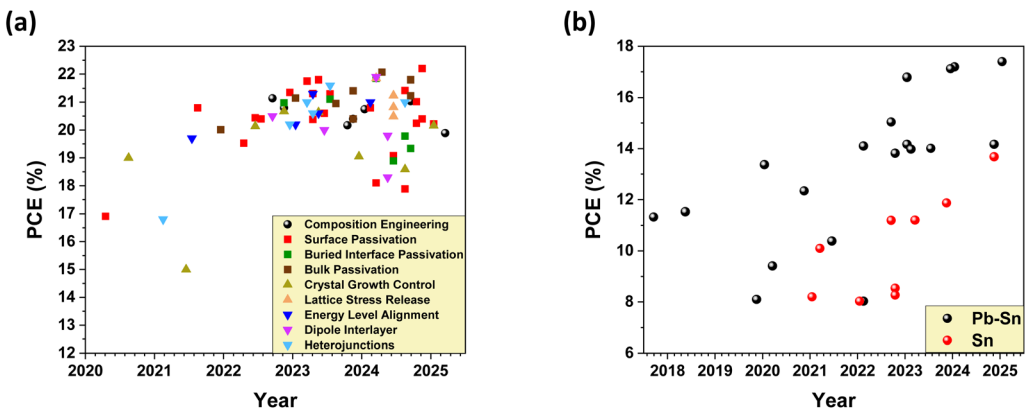

Fig. 19 Recent progress in PCE development for inorganic perovskite solar cells. (a) Pb-based inorganic perovskite solar cells with respect to development strategies (circle = composition engineering; square = defect passivation; upright triangle = inhibiting defect formation; upside-down triangle = interface modification). (b) Pb–Sn (black) and Sn-based (red) inorganic perovskite solar cells.

CIGS, organic photovoltaics, and even other inorganic perovskites.

Despite recent progress, inorganic perovskite solar cells still exhibit lower efficiencies than hybrid perovskite solar cells. Therefore, continued research is required to further improve the efficiency of inorganic perovskite solar cells, along with the development of tandem solar cells to overcome the theoretical efficiency limit of single-junction devices. In particular, research on Sn- and Sn–Pb-based inorganic perovskites, with their theoretically ideal bandgaps for single-junction operation and compatibility as bottom cells in tandem architectures, is regarded as essential to advancing the field.

To further advance the development of inorganic perovskite solar cells, it is essential to investigate detailed degradation mechanisms associated with phase instability, interfaces, and grain boundaries. Precise defect control using novel additives and multifunctional passivation agents is required, while strategies such as using internal graded heterojunctions, low-dimensional heterostructure integrations, and interface dipole modifications hold great promise for substantially improving both efficiency and stability.

For the commercialization of inorganic perovskite solar cells, further research is needed on using inorganic CTLs for the development of all-inorganic devices, since inorganic CTLs are mechanically and chemically more robust compared to organic CTLs and do not require the use of hygroscopic additives, as well as HTM-free carbon electrode architectures, which offer improved stability and reduced fabrication costs. In addition, the development of scalable strategies to maintain high efficiency and stability in large-area devices and modules and advanced encapsulation technologies to ensure robust operational stability under extreme environmental conditions is essential.

Finally, the extended application of inorganic perovskite solar cells can be envisioned in the field of indoor photovoltaics (IPVs), as they have similar device structures and operational principles. The relatively wide bandgaps and high open-circuit voltages of inorganic perovskites make them well suited for photoelectric conversion under low-intensity, narrow-spectrum indoor lighting, positioning them as strong candidates for indoor photovoltaic applications. However, achieving high IPV performance requires addressing unique challenges such as optimizing charge transport under low light, spectral matching to artificial light sources, minimizing non-radiative recombination losses, and developing lead-free devices by replacing toxic Pb-based compositions. The strategies discussed in this review—including compositional engineering, defect passivation, and interfacial engineering—can be effectively adapted to meet these demands, offering a valuable foundation for extending the application of inorganic perovskites to diverse photovoltaic environments, including indoor environments.

Data availability

No primary research results, software or code have been included and no new data were generated or analysed as part of this review.

Author contributions

Seok Yeong Hong: writing – original draft, investigation, David Sunghwan Lee: writing – original draft, investigation, Hyong Joon Lee: writing – original draft, investigation, Ki-Ha Hong: writing – original draft, investigation, and Sang Hyuk Im: writing – original draft, supervision.

Conflicts of interest

There are no conflicts of interest to declare.

Acknowledgements

This work was supported by the National Research Foundation of Korea (NRF) grant funded by the Korean government (MSIT) (No. 2024M3H4A1A03044871, RS-2025-12342968 and RS-2024-00458731).

References

1 A. Kojima, K. Teshima, Y. Shirai and T. Miyasaka, *J. Am. Chem. Soc.*, 2009, **131**, 6050–6051.
2 H.-S. Kim, C.-R. Lee, J.-H. Im, K.-B. Lee, T. Moehl, A. Marchioro, S.-J. Moon, R. Humphry-Baker, J.-H. Yum and J. E. Moser, *Sci. Rep.*, 2012, **2**, 591.
3 W. S. Yang, B.-W. Park, E. H. Jung, N. J. Jeon, Y. C. Kim, D. U. Lee, S. S. Shin, J. Seo, E. K. Kim and J. H. Noh, *Science*, 2017, **356**, 1376–1379.
4 S. Meloni, T. Moehl, W. Tress, M. Franckevičius, M. Saliba, Y. H. Lee, P. Gao, M. K. Nazeeruddin, S. M. Zakeeruddin and U. Rothlisberger, *Nat. Commun.*, 2016, **7**, 10334.
5 H. Cho, S.-H. Jeong, M.-H. Park, Y.-H. Kim, C. Wolf, C.-L. Lee, J. H. Heo, A. Sadhanala, N. Myoung and S. Yoo, *Science*, 2015, **350**, 1222–1225.
6 T. H. Chowdhury, Y. Reo, A. R. B. M. Yusoff and Y. Y. Noh, *Advanced Science*, 2022, **9**, 2203749.
7 H. M. Cho and H. W. Jang, *Electron. Mater. Lett.*, 2025, 1–20.
8 NREL Best Research-Cell Efficiency Chart, **https://www2.nrel.gov/pv/cell-efficiency**.
9 J. Hidalgo, W. Kaiser, Y. An, R. Li, Z. Oh, A.-F. Castro-Méndez, D. K. LaFollette, S. Kim, B. Lai and J. Breternitz, *J. Am. Chem. Soc.*, 2023, **145**, 24549–24557.
10 R. K. Misra, S. Aharon, B. Li, D. Mogilyansky, I. Visoly-Fisher, L. Etgar and E. A. Katz, *J. Phys. Chem. Lett.*, 2015, **6**, 326–330.
11 M. H. Miah, M. B. Rahman, M. Nur-E-Alam, M. A. Islam, M. Shahinuzzaman, M. R. Rahman, M. H. Ullah and M. U. Khandaker, *RSC Adv.*, 2025, **15**, 628–654.
12 S. Thampy, B. Zhang, K.-H. Hong, K. Cho and J. W. Hsu, *ACS Energy Lett.*, 2020, **5**, 1147–1152.
13 S. Thampy, B. Zhang, J.-G. Park, K.-H. Hong and J. W. Hsu, *Mater. Adv.*, 2020, **1**, 3349–3357.
14 S. Kim, T. Eom, Y.-S. Ha, K.-H. Hong and H. Kim, *Chem. Mater.*, 2020, **32**, 4265–4272.
15 B. W. Boote, H. P. Andaraarachchi, B. A. Rosales, R. Blome-Fernández, F. Zhu, M. D. Reichert, K. Santra, J. Li,

J. W. Petrich and J. Vela, *ChemPhysChem*, 2019, **20**, 2647–2656.
16 Z. Yao, W. Zhao and S. F. Liu, *J. Mater. Chem. A*, 2021, **9**, 11124–11144.
17 X. Tan, S. Wang, Q. Zhang, H. Liu, W. Li, L. Zhu and H. Chen, *Matter*, 2023, **6**, 691–727.
18 Y. Fu, M. T. Rea, J. Chen, D. J. Morrow, M. P. Hautzinger, Y. Zhao, D. Pan, L. H. Manger, J. C. Wright and R. H. Goldsmith, *Chem. Mater.*, 2017, **29**, 8385–8394.
19 T. Wu, X. Liu, X. Luo, X. Lin, D. Cui, Y. Wang, H. Segawa, Y. Zhang and L. Han, *Joule*, 2021, **5**, 863–886.
20 G. M. Dalpian, Q. Liu, C. C. Stoumpos, A. P. Douvalis, M. Balasubramanian, M. G. Kanatzidis and A. Zunger, *Phys. Rev. Mater.*, 2017, **1**, 025401.
21 S. A. U. Hasan, D. S. Lee, S. H. Im and K.-H. Hong, *Sol. RRL*, 2020, **4**, 1900310.
22 M. M. Byranvand, W. Zuo, R. Imani, M. Pazoki and M. Saliba, *Chem. Sci.*, 2022, **13**, 6766–6781.
23 A. Rajagopal, R. J. Stoddard, H. W. Hillhouse and A. K.-Y. Jen, *J. Mater. Chem. A*, 2019, **7**, 16285–16293.
24 T. Zhang, F. Wang, H. Chen, F. Qian, J. Li, H. Zheng, S. Yuan, X. Peng, Y. Wang and J. Huang, *Applied Physics Reviews*, 2023, **10**, 041417.
25 S. Lv, W. Gao, Y. Liu, H. Dong, N. Sun, T. Niu, Y. Xia, Z. Wu, L. Song and C. Ran, *J. Energy Chem.*, 2022, **65**, 371–404.
26 S. Hu, J. Thiesbrummel, J. Pascual, M. Stolterfoht, A. Wakamiya and H. J. Snaith, *Chem. Rev.*, 2024, **124**, 4079–4123.
27 J. A. Steele, H. Jin, I. Dovgaliuk, R. F. Berger, T. Braeckevelt, H. Yuan, C. Martin, E. Solano, K. Lejaeghere and S. M. Rogge, *Science*, 2019, **365**, 679–684.
28 F. Ke, C. Wang, C. Jia, N. R. Wolf, J. Yan, S. Niu, T. P. Devereaux, H. I. Karunadasa, W. L. Mao and Y. Lin, *Nat. Commun.*, 2021, **12**, 461.
29 G. E. Eperon, G. M. Paternò, R. J. Sutton, A. Zampetti, A. A. Haghighirad, F. Cacialli and H. J. Snaith, *J. Mater. Chem. A*, 2015, **3**, 19688–19695.
30 B. Wang, N. Novendra and A. Navrotsky, *J. Am. Chem. Soc.*, 2019, **141**, 14501–14504.
31 S. Hu, A. R. Tapa, X. Zhou, S. Pang, M. Lira-Cantu and H. Xie, *Cell Rep. Phys. Sci.*, 2024, **5**, 101825.
32 H. Jin, Y.-J. Zeng, J. A. Steele, M. B. Roeffaers, J. Hofkens and E. Debroye, *NPG Asia Mater.*, 2024, **16**, 24.
33 I. Deretzis, C. Bongiorno, G. Mannino, E. Smecca, S. Sanzaro, S. Valastro, G. Fisicaro, A. La Magna and A. Alberti, *Nanomaterials*, 2021, **11**, 1282.
34 I. Chung, J.-H. Song, J. Im, J. Androulakis, C. D. Malliakas, H. Li, A. J. Freeman, J. T. Kenney and M. G. Kanatzidis, *J. Am. Chem. Soc.*, 2012, **134**, 8579–8587.
35 W. Ning and F. Gao, *Adv. Mater.*, 2019, **31**, 1900326.
36 J. H. Heo, J. Kim, H. Kim, S. H. Moon, S. H. Im and K.-H. Hong, *J. Phys. Chem. Lett.*, 2018, **9**, 6024–6031.
37 S. W. Park, J. H. Heo, H. J. Lee, H. Kim, S. H. Im and K.-H. Hong, *ACS Energy Lett.*, 2023, **8**, 5061–5069.
38 J. Zhang, Z. Wang, A. Mishra, M. Yu, M. Shasti, W. Tress, D. J. Kubicki, C. E. Avalos, H. Lu and Y. Liu, *Joule*, 2020, **4**, 222–234.
39 A. Mishra, D. J. Kubicki, A. Boziki, R. D. Chavan, M. Dankl, M. Mladenovic, D. Prochowicz, C. P. Grey, U. Rothlisberger and L. Emsley, *ACS Energy Lett.*, 2022, **7**, 2745–2752.
40 J. H. Heo, J.-G. Park, S. H. Im and K.-H. Hong, *Sol. RRL*, 2020, **4**, 2000513.
41 G. Kieslich, S. Sun and A. K. Cheetham, *Chem. Sci.*, 2015, **6**, 3430–3433.
42 M. Becker, T. Klüner and M. Wark, *Dalton Trans.*, 2017, **46**, 3500–3509.
43 C. J. Bartel, C. Sutton, B. R. Goldsmith, R. Ouyang, C. B. Musgrave, L. M. Ghiringhelli and M. Scheffler, *Sci. Adv.*, 2019, **5**, eaav0693.
44 W. Travis, E. N. K. Glover, H. Bronstein, D. O. Scanlon and R. G. Palgrave, *Chem. Sci.*, 2016, **7**, 4548–4556.
45 A. Marronnier, G. Roma, S. Boyer-Richard, L. Pedesseau, J.-M. Jancu, Y. Bonnassieux, C. Katan, C. C. Stoumpos, M. G. Kanatzidis and J. Even, *ACS Nano*, 2018, **12**, 3477–3486.
46 T. Braeckevelt, R. Goeminne, S. Vandenhaute, S. Borgmans, T. Verstraelen, J. A. Steele, M. B. Roeffaers, J. Hofkens, S. M. Rogge and V. Van Speybroeck, *Chem. Mater.*, 2022, **34**, 8561–8576.
47 D. B. Straus, S. Guo, A. M. Abeykoon and R. J. Cava, *Adv. Mater.*, 2020, **32**, 2001069.
48 E. L. Da Silva, J. M. Skelton, S. C. Parker and A. Walsh, *Phys. Rev. B*, 2015, **91**, 144107.
49 Z.-G. Li, M. Zacharias, Y. Zhang, F. Wei, Y. Qin, Y.-Q. Yang, L.-C. An, F.-F. Gao, W. Li and J. Even, *ACS Energy Lett.*, 2023, **8**, 3016–3024.
50 H.-Y. Gu, W.-J. Yin and X.-G. Gong, *Appl. Phys. Lett.*, 2021, **119**, 191101.
51 T. Lanigan-Atkins, X. He, M. Krogstad, D. Pajerowski, D. Abernathy, G. N. Xu, Z. Xu, D.-Y. Chung, M. Kanatzidis and S. Rosenkranz, *Nat. Mater.*, 2021, **20**, 977–983.
52 Z. Guo, J. Fu, G. Chen, F. Liu, C. Yu, R. Lu and W. J. Yin, *Adv. Funct. Mater.*, 2024, **34**, 2308246.
53 Z. R. Wylie, M. Al Katrib, R. Campagna, J. E. Outen, S. Smith, P. Ruffolo, B. Bérenguier, M. Bouttemy, P. Schulz and J. A. Christians, *ACS Energy Lett.*, 2024, **9**, 4378–4385.
54 J.-P. Ma, J. Yin, Y.-M. Chen, Q. Zhao, Y. Zhou, H. Li, Y. Kuroiwa, C. Moriyoshi, Z.-Y. Li and O. M. Bakr, *ACS Mater. Lett.*, 2019, **1**, 185–191.
55 Y.-H. Kye, C.-J. Yu, U.-G. Jong, K.-C. Ri, J.-S. Kim, S.-H. Choe, S.-N. Hong, S. Li, J. N. Wilson and A. Walsh, *J. Phys. Chem. C*, 2019, **123**, 9735–9744.
56 S. Dastidar, C. J. Hawley, A. D. Dillon, A. D. Gutierrez-Perez, J. E. Spanier and A. T. Fafarman, *J. Phys. Chem. Lett.*, 2017, **8**, 1278–1282.
57 Y. Shen, T. Zhang, G. Xu, J. A. Steele, X. Chen, W. Chen, G. Zheng, J. Li, B. Guo and H. Yang, *Nature*, 2024, **635**, 882–889.
58 Z. Lin, Y. Zhang, M. Gao, J. A. Steele, S. Louisia, S. Yu, L. N. Quan, C.-K. Lin, D. T. Limmer and P. Yang, *Matter*, 2021, **4**, 2392–2402.

59 J. Lin, M. Lai, L. Dou, C. S. Kley, H. Chen, F. Peng, J. Sun, D. Lu, S. A. Hawks and C. Xie, *Nat. Mater.*, 2018, **17**, 261–267.
60 K. E. Kweon, J. Varley, T. Ogitsu, L. F. Wan, M. Shelby, Z. Song, R. J. Ellingson, Y. Yan and J. R. Lee, *Chem. Mater.*, 2023, **35**, 2321–2329.
61 W. Li, P. Liu, F. Wang, L. Pan, H. Guo, Y. Chen and S.-E. Yang, *Appl. Phys. Express*, 2020, **13**, 071003.
62 N. Aristidou, C. Eames, I. Sanchez-Molina, X. Bu, J. Kosco, M. S. Islam and S. A. Haque, *Nat. Commun.*, 2017, **8**, 15218.
63 M. Awais, R. L. Kirsch, V. Yeddu and M. I. Saidaminov, *ACS Mater. Lett.*, 2021, **3**, 299–307.
64 L. Lanzetta, T. Webb, N. Zibouche, X. Liang, D. Ding, G. Min, R. J. Westbrook, B. Gaggio, T. J. Macdonald and M. S. Islam, *Nat. Commun.*, 2021, **12**, 2853.
65 Y. Zhou and Y. Zhao, *Energy Environ. Sci.*, 2019, **12**, 1495–1511.
66 S. Tao, I. Schmidt, G. Brocks, J. Jiang, I. Tranca, K. Meerholz and S. Olthof, *Nat. Commun.*, 2019, **10**, 2560.
67 Z. Lin, M. C. Folgueras, H. K. Le, M. Gao and P. Yang, *Matter*, 2022, **5**, 1455–1465.
68 S. Peng, Y. Wang, M. Braun, Y. Yin, A. C. Meng, W. Tan, B. Saini, K. Severson, A. F. Marshall and K. Sytwu, *Matter*, 2023, **6**, 2052–2065.
69 X. Yin, Y. Guo, J. Liu, W. Que, F. Ma and K. Xu, *J. Phys. Chem. Lett.*, 2020, **11**, 7035–7041.
70 R. E. Beal, D. J. Slotcavage, T. Leijtens, A. R. Bowring, R. A. Belisle, W. H. Nguyen, G. F. Burkhard, E. T. Hoke and M. D. McGehee, *J. Phys. Chem. Lett.*, 2016, **7**, 746–751.
71 W. Wu, H. Xiong, J. Deng, M. Wang, H. Zheng, M. Wu, S. Yuan, Z. Ma, J. Fan and W. Li, *ACS Energy Lett.*, 2023, **8**, 2284–2291.
72 F. Meng, B. Yu, Q. Zhang, Y. Cui, S. Tan, J. Shi, L. Gu, D. Li, Q. Meng and C. Nan, *Adv. Energy Mater.*, 2022, **12**, 2103690.
73 M. Chen, M.-G. Ju, H. F. Garces, A. D. Carl, L. K. Ono, Z. Hawash, Y. Zhang, T. Shen, Y. Qi, R. L. Grimm, D. Pacifici, X. C. Zeng, Y. Zhou and N. P. Padture, *Nat. Commun.*, 2019, **10**, 16.
74 Z. Zhang, Q. Sun, T. Nakajima, H. Ban, Z. Liu, H. Yu, Y. Wang, Z. Xiao, Y. Shen and M. Wang, *J. Mater. Chem. A*, 2022, **10**, 23204–23211.
75 W. Zhang, H. Liu, X. Qi, Y. Yu, Y. Zhou, Y. Xia, J. Cui, Y. Shi, R. Chen and H.-L. Wang, *Advanced Science*, 2022, **9**, 2106054.
76 I. Jeong, J. Park, D. Shin, I. Hwang, N. Tsvetkov, D. Kim, J. Gwak, J. H. Park, S. I. Seok, K. Kim and H. Min, *Cell Rep. Phys. Sci.*, 2024, **5**, 101935.
77 Y. Yue, W. Zhang, R. Yang, C. Qu, Y. Wang, C. Li, H. Zhou and Y. Zhang, *Nano Energy*, 2024, **132**, 110396.
78 M. Hu, M. Chen, P. Guo, H. Zhou, J. Deng, Y. Yao, Y. Jiang, J. Gong, Z. Dai, Y. Zhou, F. Qian, X. Chong, J. Feng, R. D. Schaller, K. Zhu, N. P. Padture and Y. Zhou, *Nat. Commun.*, 2020, **11**, 151.
79 G. Chen, P. Li, T. Xue, M. Su, J. Ma, Y. Zhang, T. Wu, L. Han, M. Aldamasy, M. Li, Z. Li, J. Ma, S. Chen, Y. Zhao, F. Wang and Y. Song, *Small*, 2021, **17**, 2101380.
80 Y. Duan, J. Wang, D. Xu, P. Ji, H. Zhou, Y. Li, S. Yang, Z. Xie, X. Hai, X. Lei, R. Sun, Z. Fan, K. Zhang, S. Liu and Z. Liu, *Adv. Funct. Mater.*, 2024, **34**, 2312638.
81 C. Duan, F. Zou, Q. Wen, M. Qin, J. Li, C. Chen, X. Lu, L. Ding and K. Yan, *Adv. Mater.*, 2023, **35**, 2300503.
82 M. Hu, G. Wang, Q. Zhang, J. Gong, Z. Xing, J. Gao, J. Wang, P. Zeng, S. Zheng, M. Liu, Y. Zhou and S. Yang, *J. Energy Chem.*, 2022, **72**, 487–494.
83 Z. Wang, Q. Chen, H. Xie, X. Feng, Y. Du, T. Zhou, R. Li, J. Zhang, L. Zhang and Z. Xu, *Adv. Funct. Mater.*, 2025, **35**, 2416118.
84 K.-L. Huang, C.-F. Li, Y.-C. Chen, S.-W. Huang, Y.-C. Huang, W.-F. Su and F.-Y. Tsai, *J. Alloys Compd.*, 2024, **1004**, 175832.
85 T. Li, W. Li, K. Wang, Y. Tong, H. Wang, Y. Chen, H. Qi, Z. Kang and H. Wang, *Angew. Chem.*, 2024, **136**, e202407508.
86 C. Liu, X. Sun, Y. Yang, O. A. Syzgantseva, M. A. Syzgantseva, B. Ding, N. Shibayama, H. Kanda, F. Fadaei Tirani, R. Scopelliti, S. Zhang, K. G. Brooks, S. Dai, G. Cui, M. D. Irwin, Z. Shao, Y. Ding, Z. Fei, P. J. Dyson and M. K. Nazeeruddin, *Sci. Adv.*, 2023, **9**, eadg0087.
87 S. Zhang, C. Xu, W. Fan, H. Sun, F. Cheng, F. Dai, Z. Liang, Z. Kang and Y. Zhang, *Matter*, 2024, **7**, 3205–3220.
88 H. Lu, Q. Wen, R. Qin, Y. Han, J. Wang, W. Yang, L. Wu, L. Liu, B. Ma and K. Zhao, *Adv. Energy Mater.*, 2025, 2405072.
89 Y. Li, Y. Yan, Y. Fu, W. Jiang, M. Liu, M. Chen, X. Huang, G. Lu, X. Lu and J. Yin, *Angew. Chem., Int. Ed.*, 2024, **63**, e202412515.
90 T. Zhang, H. Ban, Q. Sun, H. Pan, H. Yu, Z. Zhang, X. Zhang, Y. Shen and M. Wang, *J. Energy Chem.*, 2022, **65**, 179–185.
91 T. Zhang, F. Qian, H. Chen, H. Zheng, L. Wang, S. Yuan, Y. Wu, Z. D. Chen and S. Li, *Chem. Eng. J.*, 2024, **479**, 147554.
92 H. Ban, Z. Zhang, L. Dai, Z. Liu, H. Yu, Y. Shen, X.-L. Zhang, J. Zhu and M. Wang, *Sol. RRL*, 2022, **6**, 2200827.
93 J. Wang, Y. Che, Y. Duan, Z. Liu, S. Yang, D. Xu, Z. Fang, X. Lei, Y. Li and S. Liu, *Adv. Mater.*, 2023, **35**, 2210223.
94 S. Wang, H. Sun, P. Wang, X. Ge, Y. Li, D. Li, Q. Huang, X. Du, Y. Zhao and X. Zhang, *Adv. Energy Mater.*, 2024, **14**, 2400151.
95 N. Zhang, J. Wang, Y. Duan, S. Yang, D. Xu, X. Lei, M. Wu, N. Yuan, J. Ding and J. Cui, *Adv. Funct. Mater.*, 2023, **33**, 2303873.
96 H. Sun, S. Wang, P. Wang, Y. Liu, S. Qi, B. Shi, Y. Zhao and X. Zhang, *J. Energy Chem.*, 2025, **100**, 87–93.
97 Y. Du, Q. Tian, X. Chang, J. Fang, X. Gu, X. He, X. Ren, K. Zhao and S. Liu, *Adv. Mater.*, 2022, **34**, 2106750.
98 X. Chang, J. Fang, Y. Fan, T. Luo, H. Su, Y. Zhang, J. Lu, L. Tsetseris, T. D. Anthopoulos and S. Liu, *Adv. Mater.*, 2020, **32**, 2001243.
99 Q. Wen, C. Duan, F. Zou, D. Luo, J. Li, Z. Liu, J. Wang and K. Yan, *Chem. Eng. J.*, 2023, **452**, 139697.
100 T. Ye, X. Wang, K. Wang, S. Ma, D. Yang, Y. Hou, J. Yoon, K. Wang and S. Priya, *ACS Energy Lett.*, 2021, **6**, 1480–1489.

101 T. Ye, K. Wang, Y. Hou, D. Yang, N. Smith, B. Magill, J. Yoon, R. R. Mudiyanselage, G. A. Khodaparast and K. Wang, *J. Am. Chem. Soc.*, 2021, **143**, 4319–4328.
102 H. Ban, T. Nakajima, Z. Liu, H. Yu, Q. Sun, L. Dai, Y. Shen, X.-L. Zhang, J. Zhu and P. Chen, *J. Mater. Chem. A*, 2022, **10**, 3642–3649.
103 S. Yang, M. Wu, X. Lei, J. Wang, Y. Han, X. He, S. Liu and Z. Liu, *ACS Energy Lett.*, 2024, **9**, 4817–4826.
104 Z. Wang, T. Xu, N. Li, Y. Liu, K. Li, Z. Fan, J. Tan, D. Chen, S. Liu and W. Xiang, *Energy Environ. Sci.*, 2024, **17**, 7271–7280.
105 S. Wang, P. Wang, B. Chen, R. Li, N. Ren, Y. Li, B. Shi, Q. Huang, Y. Zhao and M. Grätzel, *Escience*, 2022, **2**, 339–346.
106 Z. Wang, Q. Tian, H. Zhang, H. Xie, Y. Du, L. Liu, X. Feng, A. Najar, X. Ren and S. Liu, *Angew. Chem., Int. Ed.*, 2023, **62**, e202305815.
107 H. Zhang, Q. Tian, W. Xiang, Y. Du, Z. Wang, Y. Liu, L. Liu, T. Yang, H. Wu and T. Nie, *Adv. Mater.*, 2023, **35**, 2301140.
108 H. Zhang, W. Xiang, X. Zuo, X. Gu, S. Zhang, Y. Du, Z. Wang, Y. Liu, H. Wu and P. Wang, *Angew. Chem.*, 2023, **135**, e202216634.
109 Y. Liu, W. Xiang, T. Xu, H. Zhang, H. Xu, Y. Zhang, W. Qi, L. Liu, T. Yang and Z. Wang, *Small*, 2023, **19**, 2304190.
110 S. Wang, H. Jiang, Y. Gong, Y. Zhai, K. Chi and J. Qi, *ACS Sustain. Chem. Eng.*, 2024, **12**, 15562–15568.
111 S. Qi, P. Wang, H. Sun, Y. Liu, J. Chang, J. Li, Y. Zhao and X. Zhang, *Sol. RRL*, 2025, **9**, 2400819.
112 Z. Zhang, L. Dai, M. Zhang, H. Ban, Z. Liu, H. Yu, A. Gu, X.-L. Zhang, S. Chen and Y. Wang, *ACS Appl. Mater. Interfaces*, 2023, **15**, 36594–36601.
113 T. Xu, W. Xiang, J. Yang, D. J. Kubicki, W. Tress, T. Chen, Z. Fang, Y. Liu and S. Liu, *Adv. Mater.*, 2023, **35**, 2303346.
114 J. Zhang, B. Che, W. Zhao, Y. Fang, R. Han, Y. Yang, J. Liu, T. Yang, T. Chen and N. Yuan, *Adv. Mater.*, 2022, **34**, 2202735.
115 S. M. Yoon, H. Min, J. B. Kim, G. Kim, K. S. Lee and S. I. Seok, *Joule*, 2021, **5**, 183–196.
116 X. Chu, Q. Ye, Z. Wang, C. Zhang, F. Ma, Z. Qu, Y. Zhao, Z. Yin, H.-X. Deng and X. Zhang, *Nat. Energy*, 2023, **8**, 372–380.
117 S. Tan, C. Tan, Y. Cui, B. Yu, Y. Li, H. Wu, J. Shi, Y. Luo, D. Li and Q. Meng, *Adv. Mater.*, 2023, **35**, 2301879.
118 W. Dai, Y. Gou, H. Wei, C. Chen, Z. Pan, L. Lin, M. Shang, X. Wang, Q. Tai and J. Li, *Chem. Eng. J.*, 2024, **497**, 154706.
119 T. Xu, W. Xiang, X. Ru, Z. Wang, Y. Liu, N. Li, H. Xu and S. Liu, *Adv. Mater.*, 2024, **36**, 2312237.
120 J. H. Heo, F. Zhang, J. K. Park, H. J. Lee, D. S. Lee, S. J. Heo, J. M. Luther, J. J. Berry, K. Zhu and S. H. Im, *Joule*, 2022, **6**, 1672–1688.
121 D. Xu, T. Li, Y. Han, X. He, S. Yang, Y. Che, J. Xu, H. Zou, X. Guo and J. Wang, *Adv. Funct. Mater.*, 2022, **32**, 2203704.
122 J. Qiu, X. Mei, M. Zhang, G. Wang, S. Zou, L. Wen, J. Huang, Y. Hua and X. Zhang, *Angew. Chem., Int. Ed.*, 2024, **63**, e202401751.
123 D. Xu, J. Wang, Y. Duan, S. Yang, H. Zou, L. Yang, N. Zhang, H. Zhou, X. Lei and M. Wu, *Adv. Funct. Mater.*, 2023, **33**, 2304237.
124 H. Zou, Y. Duan, S. Yang, D. Xu, L. Yang, J. Cui, H. Zhou, M. Wu, J. Wang and X. Lei, *Small*, 2023, **19**, 2206205.
125 C. Tan, Y. Cui, R. Zhang, Y. Li, H. Wu, J. Shi, Y. Luo, D. Li and Q. Meng, *ACS Energy Lett.*, 2025, **10**, 703–712.
126 C. Xu, S. Zhang, W. Fan, F. Cheng, H. Sun, Z. Kang and Y. Zhang, *Adv. Mater.*, 2023, **35**, 2207172.
127 M. Hu, Y. Zhang, J. Gong, H. Zhou, X. Huang, M. Liu, Y. Zhou and S. Yang, *ACS Energy Lett.*, 2023, **8**, 1035–1041.
128 Z. Xu, J. Wang, Z. Liu, C. Xiao, J. Wang, N. Liu, J. Zhang, L. Huang, Z. Hu and Y. Zhu, *ACS Appl. Mater. Interfaces*, 2024, **16**, 53811–53821.
129 D. Xu, H. Cao, Z. Fan, B. Wang, Y. Li, R. Sun, Y. Li, J. Tan, H. Lei, Y. Duan, H. Bian and Z. Liu, *Angew. Chem.*, 2025, e202502221.
130 D. Xu, M. Wu, Y. Bai, B. Wang, H. Zhou, Z. Fan, N. Zhang, J. Tan, H. Li and H. Bian, *Adv. Funct. Mater.*, 2025, **35**, 2412946.
131 Y. Liu, T. Xu, Z. Xu, H. Zhang, T. Yang, Z. Wang, W. Xiang and S. Liu, *Adv. Mater.*, 2024, **36**, 2306982.
132 Z. Fan, Y. Duan, M. Wu, H. Zou, Y. Yao, Y. Li, D. Xu, J. Tan, Y. Li and H. Wang, *Adv. Energy Mater.*, 2024, 2405360.
133 X. Zhao, T. Liu, Q. C. Burlingame, T. Liu, R. Holley, G. Cheng, N. Yao, F. Gao and Y.-L. Loo, *Science*, 2022, **377**, 307–310.
134 J. H. Heo, J. K. Park, H. J. Lee, E. H. Shin, S. Y. Hong, K. H. Hong, F. Zhang and S. H. Im, *Adv. Mater.*, 2024, **36**, 2408387.
135 M. Zhan, S. Yuan, W. Wu, M. Wang, W. Yang, H. Xiong, Z. Tan, W. Li and J. Fan, *Small*, 2024, **20**, 2402997.
136 Q. Zhang, H. Liu, X. Wei, Y. Song, C. Lv, W. Li, L. Zhu, Y. Lan, Y. Du and K. Wang, *Small*, 2024, **20**, 2402061.
137 J. Lin, R. Huang, X. Peng, J. Zhang, G. Zhang, W. Wang, Z. Pan, H. Rao and X. Zhong, *Adv. Mater.*, 2024, **36**, 2404561.
138 K. L. Wang, H. Lu, M. Li, C. H. Chen, D. Bo Zhang, J. Chen, J. J. Wu, Y. H. Zhou, X. Q. Wang and Z. H. Su, *Adv. Mater.*, 2023, **35**, 2210106.
139 D. Li, X. Li, K. Wang, S. Ma, X. Shao, T. Yang, Y. Han, Z. Zhang, S. Liu and S. Guo, *Chem. Eng. J.*, 2024, **497**, 154845.
140 J. Wang, N. Liu, Z. Liu, J. Liu, C. Zhou, J. Zhang, L. Huang, Z. Hu, Y. Zhu and X. Liu, *ACS Appl. Nano Mater.*, 2024, **7**, 15267–15276.
141 R. Jiang, Z. Ren, T. Huang, Q. Xu, Y. Qiu, H. Cao and S. Yin, *Mater. Sci. Semicond. Process.*, 2024, **176**, 108309.
142 Y. Chen, X. Wang, Y. Wang, X. Liu, Y. Miao and Y. Zhao, *Sci. Bull.*, 2023, **68**, 706–712.
143 X. Huo, J. Lv, K. Wang, W. Sun, W. Liu, R. Yin, Y. Sun, Y. Gao, T. You and P. Yin, *Carbon Energy*, 2024, **6**, e586.
144 J. Zhang, X. Peng, H. Wu, G. Zhang, Y. Chen, W. Cai, Z. Pan, H. Rao and X. Zhong, *Angew. Chem.*, 2025, e202423655.
145 N. A. N. Ouedraogo, Y. Chen, Y. Y. Xiao, Q. Meng, C. B. Han, H. Yan and Y. Zhang, *Nano energy*, 2020, **67**, 104249.

146 Y. Yang, M. T. Hoang, D. Yao, N. D. Pham, V. T. Tiong, X. Wang and H. Wang, *J. Mater. Chem. A*, 2020, **8**, 12723–12734.
147 M. Kim and J. Kim, *Renewable Sustainable Energy Rev.*, 2025, **219**, 115835.
148 S. Rühle, *Sol. Energy*, 2016, **130**, 139–147.
149 W. Zhang, H. Liu, Y. Qu, J. Cui, W. Zhang, T. Shi and H. L. Wang, *Adv. Mater.*, 2024, **36**, 2309193.
150 T. Xu, W. Xiang, D. J. Kubicki, Y. Liu, W. Tress and S. Liu, *Advanced Science*, 2022, **9**, 2204486.
151 J. Liang, P. Zhao, C. Wang, Y. Wang, Y. Hu, G. Zhu, L. Ma, J. Liu and Z. Jin, *J. Am. Chem. Soc.*, 2017, **139**, 14009–14012.
152 N. Li, Z. Zhu, J. Li, A. K. Y. Jen and L. Wang, *Adv. Energy Mater.*, 2018, **8**, 1800525.
153 H. Ban, Q. Sun, T. Zhang, H. Li, Y. Shen and M. Wang, *Sol. RRL*, 2020, **4**, 1900457.
154 Z. Yang, X. Zhang, W. Yang, G. E. Eperon and D. S. Ginger, *Chem. Mater.*, 2020, **32**, 2782–2794.
155 S. Lee, J. Moon, J. Ryu, B. Parida, S. Yoon, D.-G. Lee, J. S. Cho, S. Hayase and D.-W. Kang, *Nano Energy*, 2020, **77**, 105309.
156 W. Zhang, Y. Cai, H. Liu, Y. Xia, J. Cui, Y. Shi, R. Chen, T. Shi and H. L. Wang, *Adv. Energy Mater.*, 2022, **12**, 2202491.
157 H. Jung, Z. Liu, M. Sotome, K. Nonomura, H. Segawa, G. Kapil, S. Hayase and T. Kondo, *ACS Appl. Mater. Interfaces*, 2025, **17**, 15613–15620.
158 C.-H. Kuan, H.-H. Shen and C.-F. Lin, *RSC Adv.*, 2021, **11**, 3264–3271.
159 S. S. Mali, J. V. Patil, J.-Y. Shao, Y.-W. Zhong, S. R. Rondiya, N. Y. Dzade and C. K. Hong, *Nat. Energy*, 2023, **8**, 989–1001.
160 X. Chen, H. Peng, X. Sun, L. Yan, X. Feng, S. Fan, R. Jia, S. Dai, X. Li, X. Zhang, X. Li and M. Cai, *Small*, 2025, **20**, 2500710.
161 H. Yu, Z. Zhang, H. Dong, X. Li, Z. Liu, J. Huang, Y. Fu, Y. Shen and M. Wang, *ACS Energy Lett.*, 2024, **9**, 5870–5878.
162 S. Li, S. Zai, X. Wei, F. Yang, W. Huang, N. Yuan, J. Ding, K. Zhao, S. Liu and W. Zhao, *Small*, 2024, **20**, 2406960.
163 Y. Cui, J. Shi, F. Meng, B. Yu, S. Tan, S. He, C. Tan, Y. Li, H. Wu and Y. Luo, *Adv. Mater.*, 2022, **34**, 2205028.
164 Y. Cui, C. Tan, R. Zhang, S. Tan, Y. Li, H. Wu, J. Shi, Y. Luo, D. Li and Q. Meng, *Sci. China Mater.*, 2024, 1–8.
165 S. Wang, H. Sun, P. Wang, S. Qi, B. Shi, Y. Zhao and X. Zhang, *Sol. RRL*, 2024, **8**, 2300739.
166 S. Zai, R. Han, W. Zhao, C. Ma, W. Huang and S. Liu, *Adv. Energy Mater.*, 2024, **14**, 2303264.
167 N. Sun, S. Fu, Y. Li, L. Chen, J. Chung, M. M. Saeed, K. Dolia, A. Rahimi, C. Li and Z. Song, *Adv. Funct. Mater.*, 2024, **34**, 2309894.
168 J. H. Heo, F. Zhang, C. Xiao, S. J. Heo, J. K. Park, J. J. Berry, K. Zhu and S. H. Im, *Joule*, 2021, **5**, 481–494.
169 Y. Shang, X. Li, W. Lian, X. Jiang, X. Wang, T. Chen, Z. Xiao, M. Wang, Y. Lu and S. Yang, *Chem. Eng. J.*, 2023, **457**, 141246.
170 Q. Sun, Z. Zhang, T. Zhang, Y. Feng, A. Gu, H. Yu, M. Zhang, X. L. Zhang, J. Zhu and Y. Shen, *ACS Energy Lett.*, 2022, **7**, 4215–4223.
171 X. Gu, W. Xiang, Q. Tian and S. Liu, *Angew. Chem., Int. Ed.*, 2021, **60**, 23164–23170.
172 W. Zhang, H. Liu, T. Huang, L. Kang, J. Ge, H. Li, X. Zhou, W. Zhang, T. Shi and H.-L. Wang, *Adv. Mater.*, 2025, **37**, 2414125.
173 G. Chen, P. Li, T. Xue, M. Su, J. Ma, Y. Zhang, T. Wu, L. Han, M. Aldamasy and M. Li, *Small*, 2021, **17**, 2101380.
174 B. Li, H. Di, B. Chang, R. Yin, L. Fu, Y. N. Zhang and L. Yin, *Adv. Funct. Mater.*, 2021, **31**, 2007447.
175 F. Gao, Y. Zhao, X. Zhang and J. You, *Adv. Energy Mater.*, 2020, **10**, 1902650.
176 H. J. Lee, J. H. Heo and S. H. Im, *Applied Physics Reviews*, 2024, **11**, 031301.
177 Y. Duan, J. Wang, D. Xu, P. Ji, H. Zhou, Y. Li, S. Yang, Z. Xie, X. Hai and X. Lei, *Adv. Funct. Mater.*, 2024, **34**, 2312638.
178 C. Liu, Y.-B. Cheng and Z. Ge, *Chem. Soc. Rev.*, 2020, **49**, 1653–1687.
179 K. L. Wang, Z. H. Su, Y. H. Lou, Q. Lv, J. Chen, Y. R. Shi, C. H. Chen, Y. H. Zhou, X. Y. Gao and Z. K. Wang, *Adv. Energy Mater.*, 2022, **12**, 2201274.
180 W. Hui, Y. Xu, F. Xia, H. Lu, B. Li, L. Chao, T. Niu, B. Du, H. Du and X. Ran, *Nano Energy*, 2020, **73**, 104803.
181 X. Guo, C. Lu, W. Zhang, H. Yuan, H. Yang, A. Liu, Z. Cui, W. Li, Y. Hu and X. Li, *ACS Energy Lett.*, 2024, **9**, 329–335.
182 W. Chai, W. Zhu, Z. Zhang, H. Xi, D. Chen, J. Zhu, J. Zhang, C. Zhang and Y. Hao, *Mater. Today Phys.*, 2023, **34**, 101088.
183 S. Wang, M.-H. Li, Y. Zhang, Y. Jiang, L. Xu, F. Wang and J.-S. Hu, *Energy Environ. Sci.*, 2023, **16**, 2572–2578.
184 R. Ji, Z. Zhang, Y. J. Hofstetter, R. Buschbeck, C. Hänisch, F. Paulus and Y. Vaynzof, *Nat. Energy*, 2022, **7**, 1170–1179.
185 S. Wang, P. Wang, B. Shi, C. Sun, H. Sun, S. Qi, Q. Huang, S. Xu, Y. Zhao and X. Zhang, *Adv. Mater.*, 2023, **35**, 2300581.
186 Y. Zhang, Z. Tang, Z. Zhang, J. Tang, M. Li, S. Zhu, W. Tan, X. Jin, T. Chen and J. Hu, *J. Energy Chem.*, 2024, **97**, 622–629.
187 S. Wang, S. Qi, H. Sun, P. Wang, Y. Zhao and X. Zhang, *Angew. Chem.*, 2024, **136**, e202400018.